A MEASUREMENT OF THE PARITY-CONSERVING, TIME-REVERSAL VIOLATING CROSS SECTION OF POLARIZED NEUTRONS ON ALIGNED HOLMIUM

by

Paul Reece Huffman

Department of Physics
Duke University

Date: _____
Approved:

_____
N. Russell Roberson, Supervisor

_____
Christopher R. Gould

_____
Berndt Müller

_____
John E. Thomas

_____
Werner Tornow

Dissertation submitted in partial fulfillment of
the requirements for the degree of
Doctor of Philosophy in the Department of Physics
in the Graduate School of Duke University

1995

ABSTRACT

(Physics – Nuclear)

A MEASUREMENT OF THE PARITY-CONSERVING, TIME-REVERSAL VIOLATING CROSS SECTION OF POLARIZED NEUTRONS ON ALIGNED HOLMIUM

by

Paul Reece Huffman

Department of Physics
Duke University

Date: _____
Approved:

_____
N. Russell Roberson, Supervisor

_____
Christopher R. Gould

_____
Berndt Müller

_____
John E. Thomas

_____
Werner Tornow

An abstract submitted in partial fulfillment of
the requirements for the degree of
Doctor of Philosophy in the Department of Physics
in the Graduate School of Duke University

1995

A MEASUREMENT OF THE PARITY-CONSERVING, TIME-REVERSAL VIOLATING CROSS SECTION OF POLARIZED NEUTRONS ON ALIGNED HOLMIUM

by

Paul Reece Huffman

A test of parity-conserving, time-reversal (T) invariance in polarized neutron transmission through an aligned holmium target has been performed at the Triangle Universities Nuclear Laboratory. The measurement searches for the T-violating five-fold correlation (FC) term $\boldsymbol{s}\cdot(\boldsymbol{I}\times\boldsymbol{k})(\boldsymbol{I}\cdot\boldsymbol{k})$ in the neutron-nucleus forward scattering amplitude, where $\boldsymbol{s}$ is the spin of the neutron, $\boldsymbol{k}$ is the momentum of the neutron, and $\boldsymbol{I}$ is the spin of the target.

A 6 MeV polarized neutron beam is produced in the $^2\mathrm{H}(\vec{\mathrm{d}},\vec{\mathrm{n}})^3\mathrm{He}$ reaction, and is transmitted through a rotating, cryogenically aligned, single crystal of ^{165}Ho. The holmium target is in the shape of a cylinder mounted vertically with its alignment axis pointing radially out. The holmium is cooled to ~ 150 mK with a $^3\mathrm{He}-{}^4\mathrm{He}$ dilution refrigerator and undergoes spontaneous nuclear alignment due to the hyperfine interaction. The transmitted neutron flux is detected using a four-detector array of plastic scintillator detectors. A second scintillator array is located between the neutron production target and the holmium sample for flux normalization. A double modulation technique — flipping the neutron spin while simultaneously rotating the alignment axis of the holmium target — is used to isolate the FC term. The neutron spin is directed vertically along $(\boldsymbol{I}\times\boldsymbol{k})$, and is flipped every 100 ms in the eight-step sequence $+--+-++-$. The target alignment axis is rotated 22.5° every four minutes in the sequence $-180^\circ \rightarrow +180^\circ \rightarrow -180^\circ$. The alignment of the target is measured using thermometry, and is verified with measurements of the deformation effect cross section at 9.4 MeV. The polarization of the neutron beam is obtained from measurements of the left-right asymmetry of the $^2\mathrm{H}(\vec{\mathrm{d}},\vec{\mathrm{n}})^3\mathrm{He}$ source reaction.

An asymmetry is formed from the transmission yields for the two neutron spin-states and is fit to the form $a_0 + a_2 \sin 2\theta$ where θ is the angle between the alignment

axis and $\boldsymbol{k}$. The FC term a_2, is identified by its $\sin 2\theta$ angular signature. A value of $a_2 = (1.1 \pm 1.0) \times 10^{-6}$ is extracted, which corresponds to a bound on the T-violating spin-correlation coefficient A_5 of $(8.6 \pm 7.7) \times 10^{-6}$, consistent with time-reversal invariance. The measurement represents an improvement of a factor of four over previous detailed balance studies of time-reversal invariance in nuclear reactions, and now represents the most precise direct test of time-reversal invariance in nuclear physics.

Acknowledgements

A thesis provides the unique opportunity to thank the many individuals involved in all aspects of this experiment. I begin by thanking four individuals who have contributed to both this experiment and to my physics education in general. My advisor Dr. Russell Roberson has provided me with the opportunity to carry out this project and has been a mentor throughout my education at Duke. Dr. Chris Gould has spent many hours working with me on the details of this measurement and the subtle aspects that arose in the analysis of the data. Dr. David Haase has taught me the art of cryogenics and the finer aspects of bass fishing. Finally, Dr. Scott Wilburn has provided valuable assistance in the design and construction of the data acquisition electronics and in the analysis of the data.

Numerous students were involved throughout this project and without their contributions, this experiment would not have been possible. I first thank Dr. Chris Keith, who while pursuing his own thesis project, provided me with assistance throughout this experiment. Tim Murphy, Brian Raichle, Joe Walston, Bret Crawford, and David Junkin deserve thanks for the many midnight shifts performed during collection of the data and Joe deserves further thanks for his help with the Monte-Carlo calculations performed in the early stages of this project.

Other individuals who have contributed to the project include Dr. Mike Seely; although he joined our group in the mid stages of this project, he provided valuable advice and assistance on both the target design and measurement procedures. I thank Dr. Werner Tornow for providing advice and support in the development of the neutron production target and the neutron detectors. Finally, Dr. Jim Koster deserves thanks for performing

the first measurement of this type.

The support staff at TUNL have contributed in numerous ways to this experiment. I thank Sidney Edwards for help in the design and repair of many electronic modules and Patrick Mulkey for his excellent work in the assembly of the phototube bases and the countless number of BNC cables. I thank John Dunham for the maintenance and operation of the polarized ion source and Dr. Tom Clegg for his continued support in improving the source. Lastly, I thank Paul Carter and Richard O'Quinn for maintaining the accelerator and their advice and assistance in the preparation of my beam line.

Many pieces of equipment designed for this experiment were machined by the instrument makers at the Duke instrument shop. Bob Hogan and Robert Timberlake deserve recognition for their advice and excellent work in the construction of the mounting apparatus of the holmium target and construction of the liquid nitrogen cooled deuterium gas cell.

I thank my parents for making my education possible and thank my mother, my sister Merisue, and Warren and Joyce Gurganus for their support throught my graduate education. Lastly, I thank my wife Roxanne for her love and support, without which none of this would have been possible.

Paul Reece Huffman

Duke University

October 1995

To My Father

Paul Franklin Huffman, Jr.

1938 – 1988

Contents

List of Figures

List of Tables

Chapter 1

Introduction

Symmetry concepts have played an important role in understanding basic physics. The discrete symmetry operators are parity (P), charge conjugation (C), and time reversal (T). While each may separately be violated, the combination of the symmetries via the CPT theorem [Lüd57] is believed always to be conserved. Parity and charge conjugation violations were the first to be observed in weak interactions. For many years, the combination of CP however was believed to be conserved, as was T on its own. But, in 1964, the CP-violating decay of the neutral kaon system was observed [Chr64], and the combination of CP-violation and the CPT theorem implied that time-reversal invariance was violated. To this date however, no experiments have directly observed time-reversal violation in any system.

The discovery of CP-violation prompted numerous searches for time-reversal violating interactions. The experiments are generally classified into two categories: those which conserve parity and those which do not. The most precise parity non-conserving, time-reversal violating experiments include measurements of the electric dipole moments (edm) of the neutron [Smi90, Alt92], of atomic ^{199}Hg [Jac93], and of molecules [Cho89]. Using the bounds set by these measurements, P-odd T-violating interactions are known to be $\lesssim 10^{-11}$ times smaller than the strong interaction [Hen89, Her92], approaching limits which are the predictions set by the standard model at the $\sim 10^{-16}$ level [Hen89].

Time-reversal violating interactions which are parity conserving are much less constrained. Previous detailed balance tests ($^{27}\mathrm{Al} + \mathrm{p} \rightleftarrows {}^{24}\mathrm{Mg} + \alpha$) constrain the strength of this interaction to only $\lesssim 10^{-3}$ times the strength of the strong interaction [Bla83]. These interactions can only arise within the standard model through second order weak interactions or can arise in first order in exotic models [Eng95]. Studies of P-conserving, T-violating interactions are therefore searches for physics beyond the standard model.

Since the discovery of compound nuclear resonance enhancements in parity violation [Alf83], low energy neutron physics has quickly emerged as a sensitive way of testing fundamental symmetry violations. On-resonance enhancements of $\sim 10^5 - 10^6$ have been observed in parity-violating transmission asymmetries using epithermal neutrons. These enhancements have lead to a systematic study of the parity-violating interaction through measurements in many nuclei [Bow93]. This work has laid the foundation for similar studies of T-violating interactions using both resonance enhancements (as in the parity violating measurements) [Huf95] and MeV neutron transmission [Kos91].

Searches for T-violating interactions using neutron transmission study P-non-conserving, T-violation through the three-fold correlation term, and study P-conserving, T-violation through the five-fold correlation term. The three-fold correlation refers to an $\boldsymbol{s} \cdot (\boldsymbol{I} \times \boldsymbol{k})$ vector dependence in the total cross section. Here $\boldsymbol{s}$ is the spin of the incident neutron, $\boldsymbol{I}$ is the spin of the target nucleus, and $\boldsymbol{k}$ is the momentum of the neutron beam. Development of a ^{139}La target is underway at Kyoto University (^{139}La shows a 10% parity violation at 0.73 eV) [Shi93], but experiments to measure this three-fold correlation term remain in the development stages [Mas93].

The five-fold correlation (FC) term in the neutron total cross has a $\boldsymbol{s} \cdot (\boldsymbol{I} \times \boldsymbol{k})(\boldsymbol{I} \cdot \boldsymbol{k})$ vector dependence. It is studied via polarized neutron transmission through an aligned target. The angular dependence of the FC term varies as $\sin 2\theta$ when $\boldsymbol{s}$ is perpendicular to $(\boldsymbol{I} \times \boldsymbol{k})$ with θ defined as the angle between $\boldsymbol{I}$ and $\boldsymbol{k}$. A double modulation procedure — flipping the neutron spin while simultaneously rotating the holmium alignment axis — is used to extract the T-violating FC term. Measurements of this term using polarized neu-

tron transmission through a rotating aligned ^{165}Ho target have previously been performed, setting bounds of $\sim 10^{-2}$ on α_T (the ratio of the T-violating to T-conserving nuclear matrix elements) [Kos90, Kos91]. This measurement laid the foundation for the work discussed in this thesis, where the upper bound on the P-conserving, T-violating interaction is improved by a factor of fifty. The large improvement results from a higher neutron polarization, a higher target alignment, and a larger neutron flux.

Neutrons are produced in the $^2\mathrm{H}(\vec{\mathrm{d}},\vec{\mathrm{n}})^3\mathrm{He}$ polarization transfer reaction and are transmitted through a rotating, cryogenically aligned, single crystal of ^{165}Ho. The holmium target is in the shape of a cylinder mounted vertically with its c-axis pointing radially out. The holmium is cooled with a dilution refrigerator to $\sim$ 150 mK, and undergoes spontaneous nuclear alignment due to the hyperfine interaction. Polarized neutrons are transmitted through the holmium target and detected at 0° using a four-detector array of plastic scintillator detectors. A second scintillator array is located between the neutron production target and the holmium sample for flux normalization purposes. The spin of the neutron beam is directed along $(\boldsymbol{I} \times \boldsymbol{k})$ and is flipped every 100 ms in the eight-step sequence $+\ -\ -\ +\ -\ +\ +\ -$. The target is rotated 22.5° every four minutes in the sequence $-180°, \ldots, -22.5°, 0°, 22.5°, \ldots, +180°, \ldots, -180°$. An asymmetry is formed from the transmission yields for the two neutron spin-states and is fit to the form $a_0 + a_2 \sin 2\theta$ to extract a bound on the FC term a_2. This bound is directly compared to measurements in other systems using the theoretical analysis of Engel *et al.* [Eng95].

This thesis presents measurements of the five-fold correlation term at 5.9 MeV. The theoretical framework for this measurement is presented in Chapter 2. The experimental apparatus and procedures are discussed in Chapter 3. Chapter 4 presents the systematic effects that can arise and measurements of various quantities needed in the analysis of the time-reversal data. Chapter 5 presents the analysis of the data and Chapter 6 concludes this thesis with a presentation of the results of this measurement, including comparisons with measurements in other systems. The present measurement is now the most precise direct test of parity-conserving, time-reversal invariance in nuclear physics.

Chapter 2

Theoretical Background

The theoretical framework of this experiment is presented beginning with a brief description of polarization phenomena. This formalism is then used to discuss the spin-dependence in the total cross section, including the parity-conserving, time-reversal violating term of interest. The final section presents the theoretical analysis needed to compare the results of this experiment with other time-reversal measurements.

2.1 Polarization Formalism

The analysis of the data from experiments involving polarized beams and/or targets is facilitated if the proper formalism is used to describe the polarization states. Over the years, numerous conventions have arisen to describe polarization states and polarization observables, but the most useful is based on the Madison convention [Sat71], and uses the spherical tensor notation to label the polarizations. This section discusses these tensors. A general discussion of polarization formalism and observables is given by Simonius [Sim74].

For an ensemble of particles with nuclear spin s, the probability of a particle being in a given magnetic substate m is given by the density matrix $\rho_{mm'}$. Since the density matrix is not the most convenient form to represent polarization phenomena, $\rho_{mm'}$ is expressed in

terms of irreducible spherical tensors

$$t_{kq}(s) = \hat{s} \sum_{m} (-1)^{s-m} \langle ssm' - m | kq \rangle \rho_{mm'}, \tag{2.1}$$

where k denotes the rank of the tensor ($0 \leq k \leq 2s$) with components q ($-k \leq q \leq k$) [Sim74], $\langle ab\alpha\beta|c\gamma\rangle$ denotes a Clebsch-Gordan coefficient [Bri71], and $\hat{s} = \sqrt{2s+1}$. Spherical tensors are chosen because they have simple rotational properties compared to the density matrices.

For beams produced in a polarized ion source, the geometry of the magnetic fields in the ionizer creates a symmetry axis for the polarization. Similarly, cryogenically aligned targets will have a symmetry axis defined by the crystal structure. These systems are axially symmetric and the statistical tensors $\tilde{t}_{kq}(s)$ describing the polarization states are diagonal ($\tilde{t}_{kq}(s) = 0$ for $q \neq 0$). The statistical tensor in an arbitrary direction $\hat{\boldsymbol{s}}$ given an initially axially symmetric tensor $\tilde{t}_{k0}(s)$ is

$$t_{kq}(s) = \sqrt{\frac{4\pi}{2k+1}}\, Y_k^q(\hat{\boldsymbol{s}})\, \tilde{t}_{k0}(s), \tag{2.2}$$

where $Y_k^q(\hat{\boldsymbol{s}})$ is a spherical harmonic. The direction of the unit vector $\hat{\boldsymbol{s}}$ is given by the polar angles (θ, ϕ) defined in Figure 2.1 in accordance with the Madison convention [Sat71].

The neutron beam is produced via the $^2\mathrm{H}(\vec{\mathrm{d}}, \vec{\mathrm{n}})^3\mathrm{He}$ reaction and thus the polarization of both the deuteron beam and the neutron beam must be considered. The deuteron has a spin of $s = 1$ and, since it is created with a polarized ion source, two tensors are sufficient to completely describe its polarization state: $\tilde{t}_{10}(1)$ and $\tilde{t}_{20}(1)$. These are related to the vector and tensor polarizations P_z and P_{zz} via $P_z = \sqrt{\frac{2}{3}}\, \tilde{t}_{10}(1)$ and $P_{zz} = \sqrt{2}\, \tilde{t}_{20}(1)$. The deuteron beam emerges from the polarized ion source with its polarization along the z-axis. A Wien filter rotates the polarization symmetry axis along the vertical y-axis (in order to produce vertically polarized neutrons) and the deuteron beam is then accelerated and strikes a deuterium gas cell to produce a polarized neutron beam.

The neutron polarization P_n at 0° can be expressed in terms of the vector and tensor

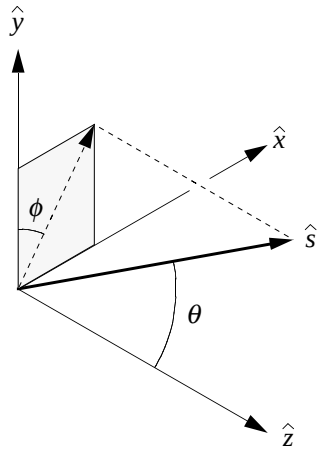

Figure 2.1: The coordinate system for scattering experiments adopted by the Madison convention [Sat71]. The beam is directed along the z-axis with the y-axis defined by the scattering plane.

polarizations of the deuteron beam [Ohl72]:

$$P_n = \frac{\frac{3}{2} K_y^{y'}(0^\circ)\, P_z}{1 - \frac{1}{4} A_{zz}(0^\circ)\, P_{zz}} \tag{2.3}$$

where $K_y^{y'}(0^\circ)$ is the polarization transfer coefficient and $A_{zz}(0^\circ)$ is the tensor analyzing power. The polarization of the neutron beam is along the same direction as the polarization of the deuteron beam. To measure this polarization, a pair of detectors is placed symmetrically about the z-axis at angles $\pm\theta$. The left-right asymmetry for the detector pair is [Ohl72]

$$\mathcal{E}_{LR} = \frac{N_L - N_R}{N_L + N_R} = \frac{\frac{3}{2} A_y(\theta)\, P_z}{1 + \frac{1}{2} A_{yy}(\theta)\, P_{zz}}, \tag{2.4}$$

where N_L and N_R denote the number of neutrons scattered into the left and right detectors, and $A_y(\theta)$ and $A_{yy}(\theta)$ are the (known) vector and tensor analyzing powers for the $^2\mathrm{H}(\vec{\mathrm{d}}, \vec{\mathrm{n}})^3\mathrm{He}$ reaction.

The polarized ion source is configured to produce a beam with vector polarization either parallel (+) or antiparallel (−) to the positive y-axis, which leaves four unknown polarization states with maximum values of $P_z^{\pm} = \pm 1$ and $P_{zz}^{\pm} = 1$. Substituting Equation 2.4

into Equation 2.3, and taking $P_{zz}^{\pm} = |P_z^{\pm}|$ [Kei94], gives the neutron polarization in terms of the left-right polarization asymmetry $\mathcal{E}_{LR}^{\pm}$:

$$P_n^{\pm} = \frac{K_y^{y'}\,\mathcal{E}_{LR}^{\pm}}{\left(A_y(\theta) \mp \frac{1}{3}\,A_{yy}(\theta)\,\mathcal{E}_{LR}^{\pm} \mp \frac{1}{6}\,A_{zz}(0^\circ)\,\mathcal{E}_{LR}^{\pm}\right)}. \tag{2.5}$$

A general discussion of polarization transfer reactions can be found in [Ohl72].

The spin of the holmium nucleus is 7/2 and a complete description of its polarization requires spherical tensors up to rank 7 ($0 \leq k \leq 7$). Even-rank tensors correspond to *alignment*, whereas the odd-rank tensors correspond to *polarization*. A discussion of the alignment of the holmium requires an understanding of its crystal structure and is deferred to Section 3.4.1. Due to the crystal structure and method of alignment, the holmium sample has zero net polarization ($\tilde{t}_{k0} = 0$ if k is odd). This property is used later to isolate the five-fold term in the total cross section.

2.2 Spin-Dependent Total Cross Section

The spin-dependent total cross section for neutron scattering has been discussed in detail by numerous authors ([Alf73, Bar87, Gou90, Hni87, Hni94a, Hni94b]). It is derived from the optical theorem and forward scattering amplitude in Appendix A. Following the notation introduced there, the neutron total cross section, σ_T, is separated into a sum of partial cross sections, σ_{kK}, that depend on the rank of the statistical tensors describing the polarization states of the beam (k) and target (K). The total cross section is given by

$$\sigma_T = \sum_{kK} \tilde{t}_{k0}(s)\,\tilde{t}_{K0}(I)\,\sigma_{kK}, \tag{2.6}$$

where the beam direction ($\hat{\boldsymbol{k}}$) is taken along the z-axis, s denotes the spin of the incident neutron beam, I denotes the spin of the target, and $\boldsymbol{\ell}$ is the angular momentum of the neutron. The spin-orbit angular momentum coupling scheme ($\boldsymbol{\ell} + \boldsymbol{s} = \boldsymbol{j}$, $\boldsymbol{j} + \boldsymbol{I} = \boldsymbol{J}$) is used and the quantities $\tilde{t}_{k0}(s)$ and $\tilde{t}_{K0}(I)$ denote the polarization states of the beam and target

in their axially-symmetric frames. The partial cross sections, σ_{kK}, are [Hni94b]

$$\begin{aligned}\sigma_{kK} &= 4\pi\lambda\!\!\!^{-2}\frac{\hat{k}\hat{K}}{\hat{s}\hat{I}}\mathrm{Im}\sum_{\Lambda}\hat{\Lambda}\,C_{kK\Lambda}(\hat{\boldsymbol{s}}\hat{\boldsymbol{I}}\hat{\boldsymbol{k}})\sum_{J\ell j\ell' j'}(2J+1)\,\hat{\ell}\hat{j}\hat{j}' \\ &\times\left\langle \ell\Lambda 00|\ell' 0\right\rangle W\left(JjIK;Ij'\right)\left\{\begin{array}{ccc}\ell & s & j\\ \Lambda & k & K\\ \ell' & s & j'\end{array}\right\}T^{J}_{\ell' j'\ell j},\end{aligned} \tag{2.7}$$

where $W(abcd;ef)$ is a Racah coefficient [Bri71], $\left\{\begin{array}{ccc}a & b & c\\ d & e & f\\ g & h & i\end{array}\right\}$ is a *9-j* coefficient [Bri71], and $\lambda\!\!\!^{-}$ is the reduced wavelength. The T-matrix elements, $T^{J}_{\ell' j'\ell j} = (1/2i)(S^{J}_{\ell' j'\ell j} - \delta_{\ell\ell'}\delta_{jj'})$, contain the elements of the elastic-scattering S-matrix for the reaction (Section 2.2.2). The spin-correlation coefficients, $C_{kK\Lambda}(\hat{\boldsymbol{s}}\hat{\boldsymbol{I}}\hat{\boldsymbol{k}})$, are defined by

$$C_{kK\Lambda}(\hat{\boldsymbol{s}}\hat{\boldsymbol{I}}\hat{\boldsymbol{k}}) = \frac{(4\pi)^{3/2}}{\hat{k}\hat{K}}\left[\left[Y^{q}_{k}(\hat{\boldsymbol{s}})\otimes Y^{-q}_{K}(\hat{\boldsymbol{I}})\right]_{\Lambda 0}\otimes Y^{0}_{\Lambda}(\hat{\boldsymbol{k}})\right]_{00}, \tag{2.8}$$

where the product of two spherical tensors $Y^{q}_{k}(\hat{\boldsymbol{s}})$ and $Y^{-q}_{K}(\hat{\boldsymbol{I}})$ coupled to rank Λ and projection 0 is given by

$$\left[Y^{q}_{k}(\hat{\boldsymbol{s}})\otimes Y^{-q}_{K}(\hat{\boldsymbol{I}})\right]_{\Lambda 0} = \sum_{q} Y^{q}_{k}(\hat{\boldsymbol{s}})Y^{-q}_{K}(\hat{\boldsymbol{I}})\left\langle kKq\,-q|\Lambda 0\right\rangle. \tag{2.9}$$

These tensor products can be rewritten as vector products of the spin and momentum unit vectors ($\hat{\boldsymbol{s}}$, $\hat{\boldsymbol{I}}$, and $\hat{\boldsymbol{k}}$) to more readily illuminate the angular dependences in the total cross section. This is examined in the next section.

2.2.1 Angular Dependence of the Total Cross Section

The spin-correlation factors $C_{kK\Lambda}(\hat{\boldsymbol{s}}\hat{\boldsymbol{I}}\hat{\boldsymbol{k}})$ contain all of the geometric features of the partial cross sections. For a given $(kK\Lambda)$, the tensor product in Equation 2.8 can be rewritten using Equation 2.9, to explicitly show the angular dependences as vector products of the spin and momentum unit vectors. A summary of these relations for all possible ranks of neutron polarization ($k = 0, 1$) and ranks of target polarization/alignment to $K = 2$ is given in Table 2.1.

$(kK\Lambda)$	$C_{kK\Lambda}(\hat{\boldsymbol{s}}\hat{\boldsymbol{I}}\hat{\boldsymbol{k}})$	P	T
(000)	1	$+$	$+$
(011)	$-\sqrt{\frac{1}{3}}\,\hat{\boldsymbol{I}}\cdot\hat{\boldsymbol{k}}$	$-$	$+$
(022)	$\frac{3}{2}[(\hat{\boldsymbol{I}}\cdot\hat{\boldsymbol{k}})^2-\frac{1}{3}]$	$+$	$+$
(101)	$-\sqrt{\frac{1}{3}}\,\hat{\boldsymbol{s}}\cdot\hat{\boldsymbol{k}}$	$-$	$+$
(110)	$-\sqrt{\frac{1}{3}}\,\hat{\boldsymbol{s}}\cdot\hat{\boldsymbol{I}}$	$+$	$+$
(111)	$-\frac{i}{\sqrt{2}}\,\hat{\boldsymbol{s}}\cdot(\hat{\boldsymbol{I}}\times\hat{\boldsymbol{k}})$	$-$	$-$
(112)	$\sqrt{\frac{3}{2}}\,[(\hat{\boldsymbol{s}}\cdot\hat{\boldsymbol{k}})(\hat{\boldsymbol{I}}\cdot\hat{\boldsymbol{k}})-\frac{1}{3}(\hat{\boldsymbol{s}}\cdot\hat{\boldsymbol{I}})]$	$+$	$+$
(121)	$-\sqrt{\frac{3}{10}}\,[(\hat{\boldsymbol{s}}\cdot\hat{\boldsymbol{I}})(\hat{\boldsymbol{I}}\cdot\hat{\boldsymbol{k}})-\frac{1}{3}(\hat{\boldsymbol{s}}\cdot\hat{\boldsymbol{k}})]$	$-$	$+$
(122)	$i\sqrt{\frac{3}{2}}\,[\hat{\boldsymbol{s}}\cdot(\hat{\boldsymbol{I}}\times\hat{\boldsymbol{k}})(\hat{\boldsymbol{I}}\cdot\hat{\boldsymbol{k}})]$	$+$	$-$
(123)	$-\frac{\sqrt{15}}{2}\,[(\hat{\boldsymbol{s}}\cdot\hat{\boldsymbol{k}})(\hat{\boldsymbol{I}}\cdot\hat{\boldsymbol{k}})^2-\frac{2}{5}(\hat{\boldsymbol{s}}\cdot\hat{\boldsymbol{I}})(\hat{\boldsymbol{I}}\cdot\hat{\boldsymbol{k}})-\frac{1}{5}(\hat{\boldsymbol{s}}\cdot\hat{\boldsymbol{k}})]$	$-$	$+$

Table 2.1: The vector dependence of the spin-correlation coefficients and their transformations under the parity (P) and time-reversal (T) operators. The symbol + ($-$) denotes an even (odd) transformation.

The present experiment measures the partial cross section $\sigma_{12}(\Lambda=2)\equiv\sigma_{FC}$. A geometry is chosen where the neutron spin direction ($\hat{\boldsymbol{s}}$) is along the y-axis, its momentum ($\hat{\boldsymbol{k}}$) along the z-axis, and the target spin ($\hat{\boldsymbol{I}}$) in the x-z plane. In this situation, only three partial cross sections are important: the unpolarized cross section (σ_{00}), the deformation effect cross section (σ_{02}), and the five-fold correlation cross section (σ_{FC}). The total cross section to order $K=2$ is thus

$$\sigma_T=\sigma_{00}+\tilde{t}_{20}(I)\,\sigma_{02}+\tilde{t}_{10}(s)\,\tilde{t}_{20}(I)\,\sigma_{FC}. \tag{2.10}$$

The deformation effect cross section is a measure of how nonspherical the nuclear mass distribution is. It is independent of the neutron polarization, depending only on the alignment of the target. Using Equations 2.7 – 2.9, the deformation effect term in the cross section is

$$\begin{aligned}\sigma_{02} &= 4\pi\lambda\!\!\!^{-2}\,\frac{\sqrt{5}}{\hat{s}^2\hat{I}}\,\mathrm{P}_2(\cos\theta)\sum_{J\ell j\ell' j'}(-1)^{s-\ell-j'}\,(2J+1)\,\hat{\ell}\hat{j}\hat{j}' \\ &\quad\times\left\langle\ell 200|\ell' 0\right\rangle W\left(JjI2;Ij'\right)W\left(\ell j\ell' j';s2\right)\mathrm{Im}\left\{T^J_{\ell' j'\ell j}\right\},\end{aligned} \tag{2.11}$$

where θ is defined as the angle between the directions of the diagonal tensors describing the target alignment and the beam direction (ie. $\hat{\boldsymbol{I}} \cdot \hat{\boldsymbol{k}} = \cos\theta$) and $\mathrm{P}_2(\cos\theta)$ is a Legendre polynomial. In this form, the $\mathrm{P}_2(\cos\theta)$ angular dependence is evident. For targets with $I \geq 2$, partial cross sections with higher order alignments can also exist and these have been discussed in detail by Koster [Kos90]. Holmium is spin $I = \frac{7}{2}$ and the higher order terms (σ_{0K} for $K = 4, 6$) are negligible in this experiment due to the small $\tilde{t}_{40}(I)$ and $\tilde{t}_{60}(I)$ alignment. Measurements of the deformation effect cross section are presented in Chapter 4.

The five-fold correlation (FC) term in the cross section depends on both the beam polarization and target alignment. As shown in the next section, this term is zero only if time-reversal is a good symmetry. Using Equation 2.7, σ_{FC} is given by

$$\begin{aligned}\sigma_{FC} &= \pi\lambda\!\!\!^{-2}\frac{\sqrt{15}}{2\hat{s}^2\hat{I}}\sin 2\theta \sum_{J\ell j\ell' j'} (-1)^{s-\ell-j'}\,(2J+1)\,\hat{\ell}\hat{j}\hat{j}' \\ &\quad\times\frac{\ell(\ell+1)-\ell'(\ell'+1)-j(j+1)+j'(j'+1)}{\sqrt{s(s+1)}} \\ &\quad\times\left\langle \ell 200|\ell' 0\right\rangle W\left(JjI2;Ij'\right) W\left(\ell j\ell' j';s2\right) \mathrm{Im}\left\{iT^J_{\ell' j'\ell j}\right\}. \end{aligned} \tag{2.12}$$

Note that the five-fold correlation term requires both a polarized beam and an aligned target. A transfer of two units of angular momentum is required ($\boldsymbol{\ell} + \mathbf{2} = \boldsymbol{\ell}'$) and the term exhibits a $\sin 2\theta$ angular dependence. This $\sin 2\theta$ angular dependence and the neutron polarization dependence are used to isolate this term.

2.2.2 Parity and Time-Reversal Operations on σ_T

The five-fold correlation term is non-zero only if time-reversal invariance is violated. This section introduces the parity (P) and time-reversal (T) operators and the behavior of the partial cross sections under these operations. We conclude by looking explicitly at the FC term in the cross section.

The parity operator is a reflection in space ($\boldsymbol{r} \rightarrow -\boldsymbol{r}$) [Sac87] and operates on a wave function ψ as

$$P\,\psi(\boldsymbol{r},t) = \psi(-\boldsymbol{r},t). \tag{2.13}$$

The time-reversal operator, on the other hand, is a reflection in time ($t \rightarrow -t$) [Sac87] and operates on a wave function ψ as

$$T\,\psi(\boldsymbol{r},t) = \psi^*(\boldsymbol{r},-t). \tag{2.14}$$

These relations, when applied to angular momentum eigenstates with spin I, intrinsic parity π_I, and momentum $\hat{\boldsymbol{k}}$, give

$$P\,|\hat{\boldsymbol{k}}, Im_I\rangle = \pi_I|-\hat{\boldsymbol{k}}, Im_I\rangle \tag{2.15}$$

and

$$T\,|\hat{\boldsymbol{k}}, Im_I\rangle = (-1)^{I-m_I}|-\hat{\boldsymbol{k}}, I-m_I\rangle. \tag{2.16}$$

The behavior of the neutron partial cross sections under the P and T operations are contained in the spin-correlation coefficients $C_{kK\Lambda}(\hat{\boldsymbol{s}}\hat{\boldsymbol{I}}\hat{\boldsymbol{k}})$ and the elastic-scattering S-matrix. Application of Equations 2.15 and 2.16 to $C_{kK\Lambda}(\hat{\boldsymbol{s}}\hat{\boldsymbol{I}}\hat{\boldsymbol{k}})$ and $S^J_{\ell' j' \ell j}$ will thus determine the transformations of the partial cross sections under P and T.

The spin-correlation coefficients have simple transformations under the P and T operations. Beginning with the parity operator, the directions of the spins of both the beam and target do not reverse sign, whereas the direction of linear momentum does ($\hat{\boldsymbol{s}}, \hat{\boldsymbol{I}}, \hat{\boldsymbol{k}} \rightarrow \hat{\boldsymbol{s}}, \hat{\boldsymbol{I}}, -\hat{\boldsymbol{k}}$). Using the property of the spherical harmonics, $Y^m_\ell(-\hat{\boldsymbol{r}}) = (-1)^\ell\, Y^m_\ell(\hat{\boldsymbol{r}})$, the $C_{kK\Lambda}(\hat{\boldsymbol{s}}\hat{\boldsymbol{I}}\hat{\boldsymbol{k}})$'s transform under the parity operation as

$$P\,C_{kK\Lambda}(\hat{\boldsymbol{s}}\hat{\boldsymbol{I}}\hat{\boldsymbol{k}}) = (-1)^\Lambda\, C_{kK\Lambda}(\hat{\boldsymbol{s}}\hat{\boldsymbol{I}}\hat{\boldsymbol{k}}). \tag{2.17}$$

Clearly, Λ defines whether the spin-correlation coefficients are even (Λ is even) or odd (Λ is odd) under the parity operation.

The time-reversal operation, on the other hand, reverses the directions of both the spins and momenta ($\hat{\boldsymbol{s}}, \hat{\boldsymbol{I}}, \hat{\boldsymbol{k}} \rightarrow -\hat{\boldsymbol{s}}, -\hat{\boldsymbol{I}}, -\hat{\boldsymbol{k}}$). Application of the T operator to the spherical harmonics gives $T\,Y^m_\ell = (-1)^{\ell+m}\,Y^{-m}_\ell$, which implies that the spin-correlation coefficients transform as

$$T\,C_{kK\Lambda}(\hat{\boldsymbol{s}}\hat{\boldsymbol{I}}\hat{\boldsymbol{k}}) = (-1)^{k+K+\Lambda} C_{kK\Lambda}(\hat{\boldsymbol{s}}\hat{\boldsymbol{I}}\hat{\boldsymbol{k}}). \tag{2.18}$$

If $k + K + \Lambda$ is even (odd), $C_{kK\Lambda}(\hat{\boldsymbol{s}}\hat{\boldsymbol{I}}\hat{\boldsymbol{k}})$ is therefore even (odd) under the time-reversal operation. The behaviors of the spin-correlation factors under P and T (to order $K = 2$) are summarized in Table 2.1.

The elastic scattering matrix $S^J_{\ell' j' \ell j}$ — commonly referred to as the S-matrix — contains the dynamics of the nuclear reaction. The S-matrix is defined (for total angular momentum J) as the probability that a beam in the angular momentum state ℓj, exits in the state $\ell' j'$ [Bla79]. The S-matrix conserves flux,

$$\sum_{\ell' j'} \left| S^J_{\ell' j' \ell j} \right|^2 = 1, \tag{2.19}$$

and requiring orthogonality between angular momentum entrance states makes the S-matrix unitary. By definition, if a system is time-reversal invariant, both the time-reversed wave function, $T\,\psi(t)$, and the wave function, $\psi(t)$, must be eigenstates of the Hamiltonian of the system. Combining time-reversal invariance with the unitary property leads to the *reciprocity theorem* [Bla79]:

$$S^J_{\ell' j' \ell j} = S^J_{\ell j \ell' j'}. \tag{2.20}$$

Explicitly stated, the S-matrix is symmetric and unaffected by the reversal of initial and final states, provided that nuclear reactions are time-reversal invariant.

The two terms in the FC partial cross section that are affected by the time-reversal operation are the spin-correlation coefficient (which reverses sign – Table 2.1), and the elastic-scattering S-matrix (which remains unchanged – Equation 2.20). Under the T operation, this partial cross section transforms as

$$T\,\sigma_{FC} = -\sigma_{FC}. \tag{2.21}$$

Since the partial cross section changes sign upon application of the T operator, the five-fold partial cross section σ_{FC} must be identically zero for a system that is time-reversal invariant. A non-zero value of σ_{FC} would therefore directly indicate a violation of the time-reversal symmetry.

2.2.3 Isolating the Five-Fold Correlation Term

For a neutron transmission experiment, the five-fold correlation partial cross section can be isolated by forming an asymmetry between the number of neutrons transmitted with "spin-up" (+) and those with "spin-down" (−). The neutron transmission yield $N^{\pm}$ is a function of the incident flux $N_0^{\pm}$, the target thickness n, and the total cross section $\sigma_T^{\pm}$ [Kra88],

$$N^{\pm}(0^{\circ}) = N_0^{\pm}(0^{\circ})e^{-n\sigma_T^{\pm}}. \tag{2.22}$$

By forming an asymmetry between the normalized neutron transmission yields,

$$\mathcal{E} = \frac{N^{+}(0^{\circ})/N_0^{+}(0^{\circ}) - N^{-}(0^{\circ})/N_0^{-}(0^{\circ})}{N^{+}(0^{\circ})/N_0^{+}(0^{\circ}) + N^{-}(0^{\circ})/N_0^{-}(0^{\circ})}, \tag{2.23}$$

the five-fold partial cross section can be isolated. Reversing the direction of the neutron spin ($\hat{\boldsymbol{s}} \rightarrow -\hat{\boldsymbol{s}}$) leaves the unpolarized and deformation effect partial cross sections unchanged ($\sigma_{00} \rightarrow \sigma_{00}$ and $\sigma_{02} \rightarrow \sigma_{02}$), whereas the five-fold correlation partial cross section reverses sign ($\sigma_{FC} \rightarrow -\sigma_{FC}$). Thus, the unpolarized and deformation effect terms in the cross section are removed by forming this asymmetry and the five-fold correlation term is isolated. The asymmetry is

$$\begin{aligned} \mathcal{E} &= \tanh(n\,\tilde{t}_{10}(s)\,\tilde{t}_{20}(I)\,\sigma_{FC}) \\ &\cong n\,\tilde{t}_{10}(s)\,\tilde{t}_{20}(I)\,\sigma_{FC} \end{aligned} \tag{2.24}$$

if σ_{FC} is very small. In reducing Equation 2.23, the reciprocity of the S-matrix ($S^J_{\ell' j' \ell j} = S^J_{\ell j \ell' j'}$) was used to combine σ_{FC} with its time reversed state. A measurement of $\mathcal{E}$ is therefore a direct measure of asymmetric terms in the S-matrix. This means that a non-zero value of $\mathcal{E}$ would violate the reciprocity theorem, and therefore time-reversal invariance.

It is customary to remove the angular dependence in σ_{FC} and quote a bound on a new spin-correlation coefficient A_5 defined by

$$A_5 = \frac{1}{\sin 2\theta}\frac{\sigma_{FC}}{\sigma_{00}}. \tag{2.25}$$

A_5 is related to the normalized asymmetry $\mathcal{E}$ via

$$A_5 = \frac{a_2}{\tilde{t}_{10}(s)\,\tilde{t}_{20}(I)\,n\,\sigma_{00}}, \tag{2.26}$$

where a_2 is the magnitude of the $\sin 2\theta$ component in $\mathcal{E}$.

2.2.4 Contributions from False Asymmetries

Although Section 2.2.3 implies that the five-fold correlation term can be uniquely isolated, T-conserving terms that can mimic a $\sin 2\theta$ angular dependence in the normalized asymmetry must be considered. These terms can exist, either from systematic effects or sequential interactions. A detailed discussion of systematic effects and the steps taken to remove them is presented in Chapter 4. This section discusses the problem that, regardless of systematic effects, sequential T-conserving interactions can produce a $\sin 2\theta$ component in the normalized asymmetry.

The sequential interaction terms in the asymmetry are present independent of any systematic considerations. These interactions require a neutron to be scattered through one interaction channel and then rescattered through another channel with the two reactions combining to give an angular signature in the asymmetry. Bowman *et al.* [Bow89] has shown that only one such combination of interactions exist that can generate a $\sin 2\theta$ dependence, namely the $(\hat{\boldsymbol{s}} \cdot \hat{\boldsymbol{k}})$ interaction combined with the $(\hat{\boldsymbol{s}} \cdot \hat{\boldsymbol{I}})(\hat{\boldsymbol{I}} \cdot \hat{\boldsymbol{k}})$ interaction. The real part of one of these interactions will precess $\hat{\boldsymbol{s}}$ about either $\hat{\boldsymbol{k}}$ or $\hat{\boldsymbol{I}}$ — depending on the interaction — resulting in a horizontal component of $\hat{\boldsymbol{s}}$ in the x-z plane. The imaginary part of the other amplitude would produce an absorption of the neutron beam that is preferential of the neutron spin. Both interactions are parity-violating and are known to be small.

Stodolsky [Sto86] was the first to identify these terms, and to show how they can be removed by analyzing the spin of the neutron beam after it passes through the target. Kabir [Kab88] expanded this discussion to include all possible combinations of reactions that can mimic a T-violating signal and how such an analyzer removes these effects. This procedure, although unambiguous in determining the T-violating asymmetry, requires an-

alyzing the neutron polarization after the neutrons exit the target. This is a very inefficient procedure because it requires a second scattering process, effectively reducing the number of neutrons detected by $\sim 10^4$. Measuring an asymmetry at the 10^{-6} level is therefore completely impractical because it would require fluxes of neutrons of order $\sim 10^{10}$. For FC measurements however, it turns out that the T-conserving terms that can generate the FC angular signature are smaller than the limits of the present measurement and a neutron spin-analyzer is not required.

The sequential interaction terms that can generate the $\sin 2\theta$ angular signature have been independently measured. The $(\hat{\boldsymbol{s}} \cdot \hat{\boldsymbol{k}})$ term was measured by Soderstrum *et al.* [Sod88] to be $(-2.4 \pm 2.6) \times 10^{-4}$. The $(\hat{\boldsymbol{s}} \cdot \hat{\boldsymbol{I}})(\hat{\boldsymbol{I}} \cdot \hat{\boldsymbol{k}})$ term is measured in the present experiment (presented in Chapter 4) to be $(-1.0 \pm 1.2) \times 10^{-5}$. When combined, effects from the sequential interaction of these terms must be $\lesssim 10^{-9}$, well below the limits of the present measurements.

2.3 Microscopic T-Violating Optical Potential

In this section we discuss a framework in which this measurement can be compared at a fundamental level to measurements in other systems. Parity-conserving, time-reversal violating interactions do not arise in the minimal standard model [Hax94]. Such interactions can only be generated through weak corrections to P-, T-violating interactions and are expected to be extremely small [Her92]. P-conserving, time-reversal violation can, however, be modeled in terms of a meson exchange model [Sim75]. Meson exchange models treat the nucleons as fundamental particles which interact through the exchange of mesons. These models have produced a satisfactory description of the nuclear force and are widely used in describing nucleon-nucleon (NN) interactions at low energies (< 300 MeV). This description also gives a model in which to compare measurements in different systems to fundamental quantities.

Simonius [Sim75] has shown that P-conserving, T-violation can arise only through

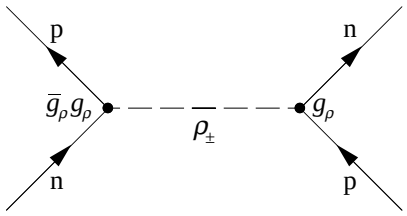

Figure 2.2: The Feynman diagram representing T-violating ρ-exchange given by Simonius [Sim75]. $\bar{g}_\rho$ is the ratio of T-violating to T-conserving coupling constants and g_ρ is the standard T-conserving coupling constant.

charged vector meson exchanges. Identical particle interactions — neutron-neutron or proton-proton — are strongly suppressed by the Pauli exclusion principle and the dominant process is neutron-proton interactions. Pseudoscalar meson exchanges (for example the π) and uncharged vector mesons (for example the ω) can not contribute, leading to charged ρ-exchange as the lowest order meson contributing to P-conserving, T-violating interactions. Processes involving heavier mesons (such as the A_1) are suppressed by short-range nucleon-nucleon repulsion, leaving charged ρ-exchange as the dominant P-conserving T-violating process.

The charged ρ-exchange interaction is parameterized by $\bar{g}_\rho$, the ratio of T-violating to T-conserving coupling constants. A Feynman diagram depicting this exchange is shown in Figure 2.2. The ρ-exchange interaction potential is given by Engel *et al.* [Eng94]:

$$V^\rho_{1,2} = \mathcal{V}^\rho_{1,2}\ [\boldsymbol{\tau_1} \times \boldsymbol{\tau_2}]_3 \tag{2.27}$$

with

$$\mathcal{V}^\rho_{1,2} = \frac{m_\rho^3 g_\rho^2 \bar{g}_\rho \mu_\nu}{4\pi M^2} \frac{e^{-m_\rho r_{12}}}{m_\rho^3 r_{12}^3}(1 + m_\rho r_{12})(\boldsymbol{\sigma}_1 - \boldsymbol{\sigma}_2) \cdot \boldsymbol{\ell}, \tag{2.28}$$

where $\boldsymbol{r_{12}} = \boldsymbol{r_1} - \boldsymbol{r_2}$, $\boldsymbol{\ell} = \boldsymbol{r_{12}} \times \frac{1}{2}(\boldsymbol{p_1} - \boldsymbol{p_2})$, $\mu_\nu = 3.70\ \mu_N$ is the isovector nucleon magnetic moment (μ_N is the nuclear magneton), M is the nucleon mass, and $g_\rho = 2.79$ is the normal strong ρNN coupling constant. The T-violation occurs in the isospin product $[\boldsymbol{\tau_1} \times \boldsymbol{\tau_2}]_3$, where $\boldsymbol{\tau_1}$ and $\boldsymbol{\tau_2}$ denotes the isospin operators of the two nucleons in the NN system.

The ρ-exchange interaction potential given in Equation 2.27 can be used to construct

an optical potential $\bar{U}(\boldsymbol{r})$ through a microscopic folding model calculation. Such a procedure has been performed for ^{165}Ho by Engel *et al.* [Eng94]. A zero-range approximation ($m_\rho \to \infty$) is used to calculate the expectation value of the ground state interaction. Terms linear in the target spin I are removed and the resulting expression is used to generate an optical potential $\bar{U}(\boldsymbol{r})$. The complete expression for this potential is given by Engel *et al.* [Eng94].

Two unique features of the potential are worth mentioning. The potential contains a factor T_5,

$$\begin{aligned} T_5 &= \frac{1}{2} r^{-2} \{ \boldsymbol{s} \cdot (\boldsymbol{I} \times \boldsymbol{r})(\boldsymbol{I} \cdot \boldsymbol{r}) + (\boldsymbol{I} \cdot \boldsymbol{r})(\boldsymbol{I} \times \boldsymbol{r}) \cdot \boldsymbol{s} \} \\ &= -2i\sqrt{\pi} \left[[\boldsymbol{I} \otimes \boldsymbol{I}]_{20} \otimes [Y_2(\hat{\boldsymbol{r}}) \otimes \boldsymbol{s}]_{20} \right]_{00} , \end{aligned} \tag{2.29}$$

which is a symmetrized form of the five-fold operator $C_{122}(\hat{\boldsymbol{s}}\hat{\boldsymbol{I}}\hat{\boldsymbol{k}})$ with $\boldsymbol{r}$ denoting the neutron position. Secondly, the radial form of the potential is unique in form and is shown in Figure 2.3.

The strength of the potential is comparable to the interaction between the incident neutron and a single valence proton in the outer shell of the nucleus. The effect is therefore suppressed by a factor of $1/A$ compared to typical one-body potentials. Koster *et al.* estimated the T-violating nuclear matrix elements by taking the ratio of inelastic to elastic cross sections for scattering into the first $7/2^-$ excited state of holmium [Kos92a]. This method assumes the potential is dependent upon the nuclear density, which does not contain this $1/A$ suppression.

The P-conserving, T-violating potential $\bar{U}(\boldsymbol{r})$ is used in a coupled-channels optical model code to calculate the observable A_5 given by Equation 2.26, thus relating $\bar{g}_\rho$ to a measurable quantity. The coupled-channels code CHUCK [Kun80] was used to perform these calculations, using Young's parameterization of the strong interaction alongside $\bar{U}(\boldsymbol{r})$ [You83]. The deformed shape of the holmium nucleus ($\beta = 0.3$) was also taken into account. A_5 as a function of energy is given in Figure 2.4 for $\bar{g}_\rho = 1$. Note the spin-correlation coefficient A_5 is maximized around $E_n = 6$ MeV.

Upon measuring A_5, a limit on the T-violating ρ-exchange coupling constant $\bar{g}_\rho$ can

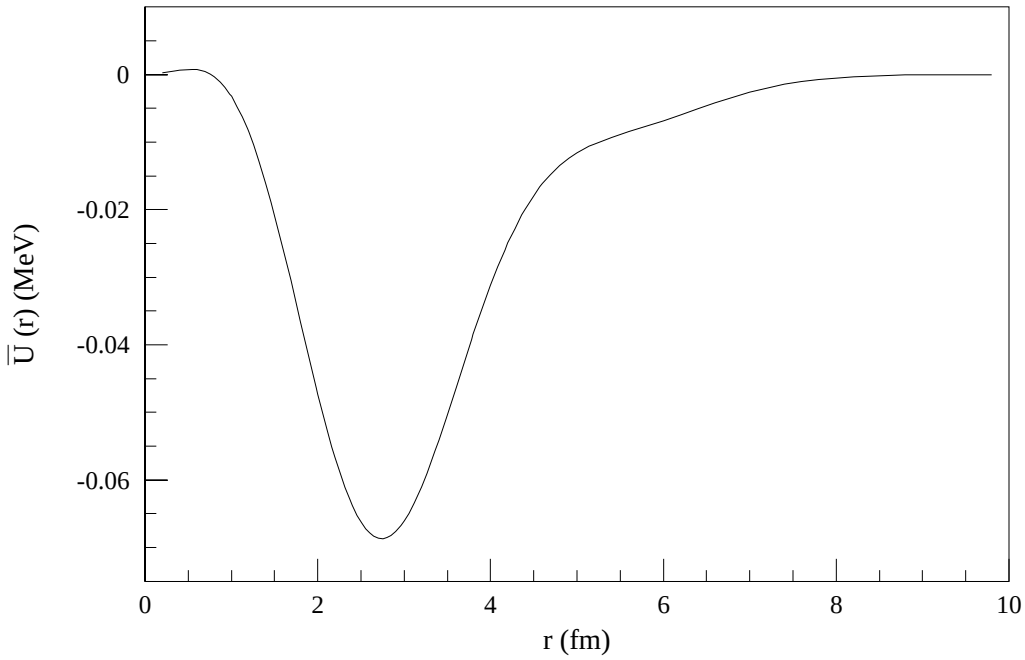

Figure 2.3: The radial dependence of the P-conserving, T-violating optical potential multiplying T_5 ($\bar{g}_\rho = 1$) [Eng94].

be set using the calculations of Engel *et al.* [Eng94]. The spin-correlation coefficient A_5 scales linearly with $\bar{g}_\rho$ and a bound can be extracted directly. Short range repulsions were ignored in the folding-model calculations above, so the bound on $\bar{g}_\rho$ must be increased by an additional factor of 2.9 not included in Figure 2.4 [Hax94].

Traditionally, limits on time-reversal violation are given in terms of α_T, the ratio of T-violating to T-conserving nuclear matrix elements. The connection between α_T and $\bar{g}_\rho$ has been established by Haxton *et al.* [Hax94] and given by

$$\alpha_T = \frac{3.6}{300}\,\bar{g}_\rho. \tag{2.30}$$

The scaling factor comes from taking the ratio of the T-violating nuclear matrix element to that of the strong interaction. Taking $\bar{g}_\rho = 1$, an average nuclear matrix element of 3.6 keV was calculated using the Simonius ρ-exchange potential [Sim75]. This matrix element is then divided by the average matrix elements of the strong interaction, of order ~ 300 keV.

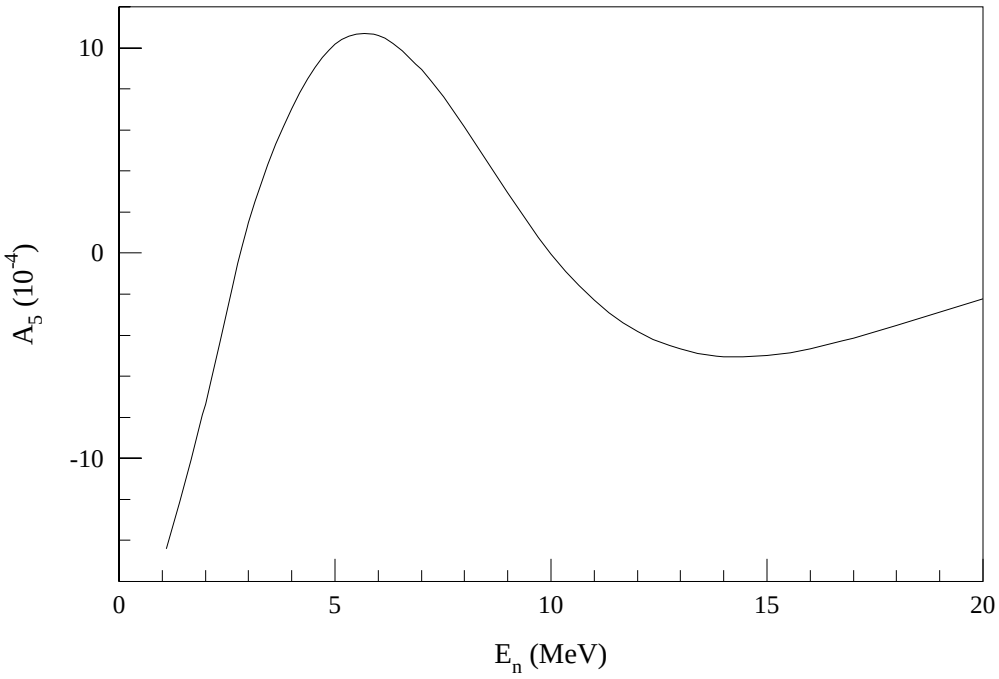

Figure 2.4: The spin-correlation coefficient A_5 for $\bar{g}_\rho = 1$ [Eng94].

With this formalism in hand, present experimental bounds can now be compared with both electric dipole moment and detailed balance experiments. A comparison is presented in Chapter 6.

Chapter 3

Experimental Apparatus and Procedure

3.1 Overview

The five-fold correlation time-reversal measurement involves transmitting polarized neutrons through an aligned holmium target. In this chapter, we discuss the production of the neutron beam, the cryogenically aligned holmium target, and the electronics and data acquisition. Neutron beams are created through secondary reactions and the most efficient reaction available for producing a 6 MeV polarized beam is $^2\mathrm{H}(\vec{\mathrm{d}},\vec{\mathrm{n}})^3\mathrm{He}$. The polarized deuteron beam is created using the TUNL Atomic Beam Polarized Ion Source (ABPIS) and accelerated through a FN Tandem Van de Graaff. Neutrons are produced when the polarized deuteron beam strikes a deuterium gas cell. The neutron flux is transmitted through a holmium target which consists of a holmium single crystal cooled to ~ 150 mK by a dilution refrigerator with a rotating central shaft. The transmitted neutrons are detected with a four-detector array of plastic scintillator detectors and a similar four-detector array is positioned between the gas cell and the target to monitor the neutron flux. The beam polarization is monitored by two liquid scintillation detectors placed at $\pm 36^\circ$ with respect to the beam direction. Counts from these ten detectors are collected using standard NIM

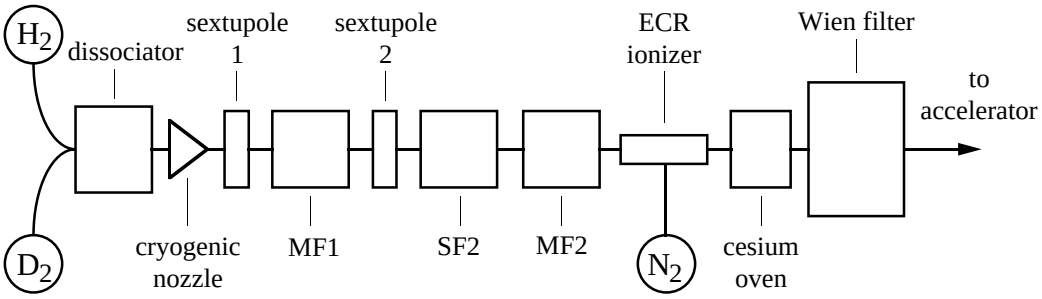

Figure 3.1: Block diagram of the TUNL Atomic Beam Polarized Ion Source. The symbols are defined in the text.

and CAMAC electronics, and stored using the XSYS data acquisition system.

3.2 Charged-Particle Beam

3.2.1 Polarized Ion Source

Polarized beams at TUNL are created using a high intensity Atomic Beam Polarized Ion Source (ABPIS). This source is capable of producing both polarized hydrogen and deuterium beams, and is utilized in the majority of experiments at TUNL. Positive beam currents of up to a hundred microamperes are available for low energy (< 80 keV) experiments, and negative beam currents of five to seven microamperes are available for injection into the accelerator. Since the design and construction of the ABPIS is well documented [Cle95a, Cle95b, Din95], only a brief overview will be given.

A block diagram of the ABPIS depicting the major components of the source and their relative locations is given in Figure 3.1. Deuterium gas enters the dissociator and flows through a glass tube surrounded by radio-frequency (RF) coils operating at 13 MHz. This cavity creates a discharge in the gas which dissociates the deuterium molecules into atoms. The atoms exit the dissociator through a cryogenic copper nozzle, forming a beam. The nozzle is cooled to 30 K to reduce the energy spread of the beam and the surfaces of the

nozzle are coated with nitrogen gas to minimize the recombination of atoms into molecules.

The atomic beam enters the sextupole magnets which focuses atomic substates with spin projections of $m_J = +1/2$ and de-focuses substates with $m_J = -1/2$. The emerging "atomic-polarized" beam then passes through an RF transition unit and into a second sextupole.

Nuclear polarization is created in the RF transition units by tuning the RF oscillators to frequencies that correspond to the energy difference between hyperfine states. Two types of transition units are used in the ABPIS: strong field (SF) and medium field (MF) units. The designs of the two units differ in the strength of the magnetic field and operational frequency. The SF unit operates between 75–155 G and 330–1485 MHz. This cavity can be tuned to a given field and frequency to allow transitions between two nuclear polarization states. In this experiment, SF2 was operated at 80 G and 460 MHz. The MF unit operates at a lower magnetic field and frequency, 8–40 G and 7.5–28 MHz. These cavities can be tuned to allow multiple transitions between nuclear polarization states to occur. Both MF units were used to create the polarized deuteron beam. MF1 was operated at 25 G and 28 MHz and MF2 was operated in the "weak-field" mode at 8 G and 8 MHz.

In practice, the power to the RF transition units can be rapidly toggled between two separate units to reverse the direction of the spin of the beam. For the two polarization states used in this experiment, MF1 was continuously on, while SF2 and MF2 were toggled to produce "spin-up" and "spin-down" beams respectively. The transition schemes used to produce the two spin-states can be expressed in a series of deuterium level diagrams. These diagrams depict the hyperfine splitting of the atomic and nuclear substates as a function of magnetic field. The stronger the magnetic field, the larger the energy separation between states. The SF transitions occur at large magnetic fields where the energy separation is large, and the MF transitions occur at low magnetic fields where the separation is small. Figures 3.2 and 3.3 give the energy level diagrams and the transition schemes. The six levels are numbered according to the substate, where the left set of arrows corresponds to the atomic polarization substate and the right set corresponds to the nuclear polarization

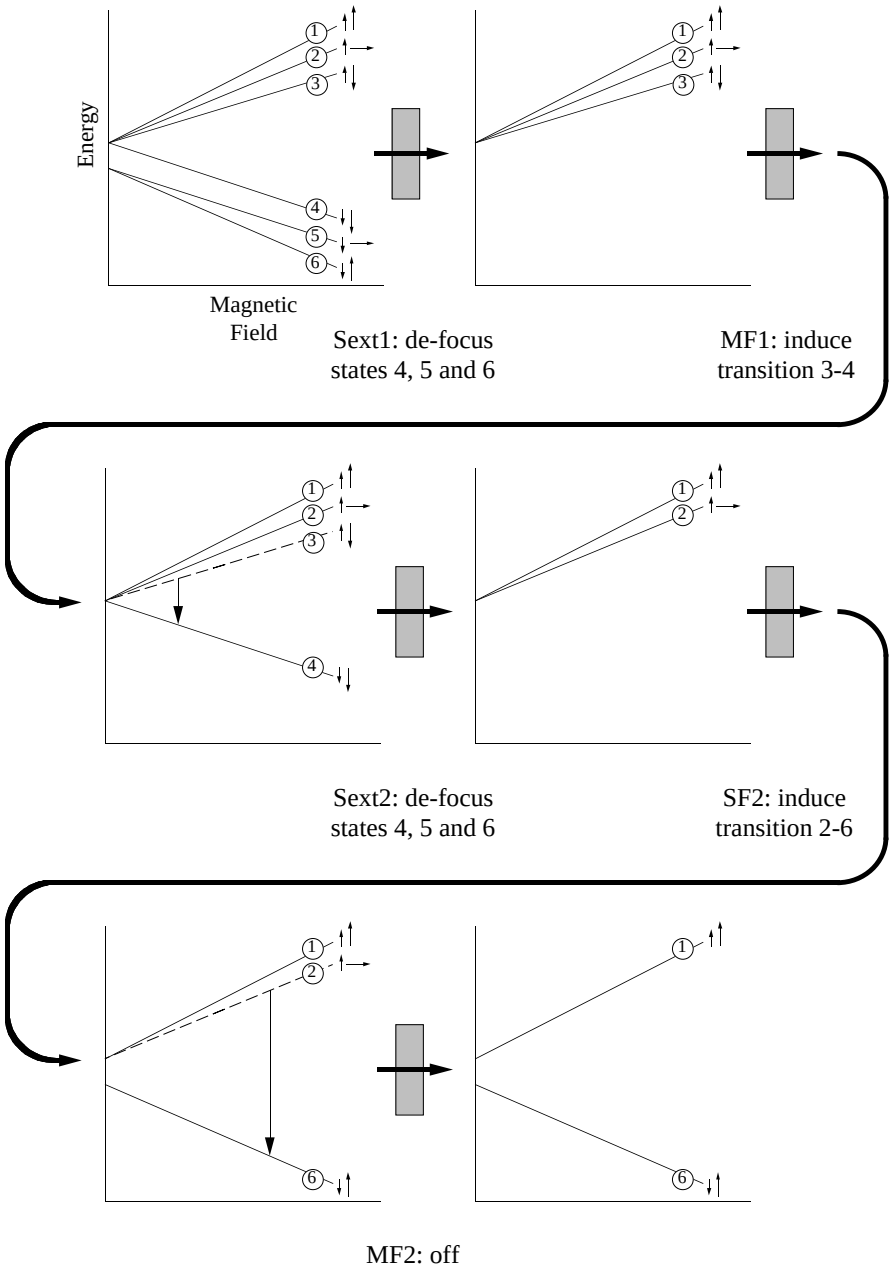

Figure 3.2: The ABPIS transition scheme for "spin-up" deuterons expressed in terms of energy level diagrams. The six levels are numbered according to the substate, where the left set of arrows denotes the atomic polarization and the right set denotes the nuclear polarization.

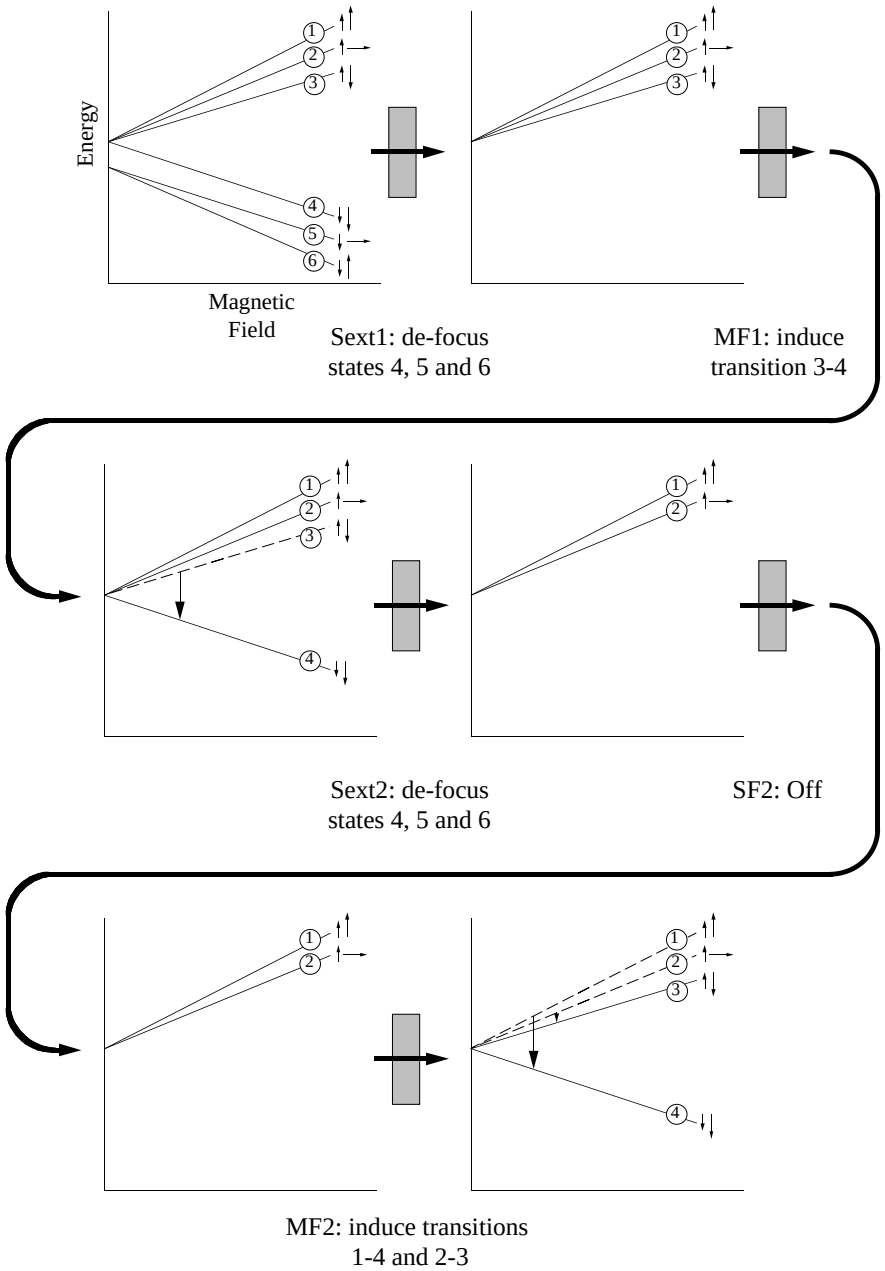

Figure 3.3: The ABPIS transition scheme for "spin-down" deuterons expressed in terms of energy level diagrams. The six levels are numbered according to the substate, where the left set of arrows denotes the atomic polarization and the right set denotes the nuclear polarization.

substate.

In each of the two spin-states, the first sextupole de-focuses states 4, 5, and 6. MF1 then induces a transition between states 3 and 4. The second sextupole de-focuses state 4, leaving states 1 and 2 remaining. For the "spin-up" transition, SF2 induces a transition between states 2 and 6, leaving the beam in a state with maximum polarization $P_z^+ = 1$ and $P_{zz}^+ = 1$. The "spin-down" transition utilizes MF2 in the "weak-field" mode to induce transitions between states 1 and 4 and states 2 and 3 to produce a beam with maximum polarization $P_z^- = -1$ and $P_{zz}^- = 1$. The actual polarizations are approximately 80% of the maximum.

The polarized beam emerges from the transition units and enters the electron cyclotron resonance (ECR) ionizer. The ECR ionizer produces high energy electrons in a plasma created with N_2 buffer gas. Electrons are confined within the plasma both axially and radially with magnetic fields and are excited by microwave power. Ionization of the polarized beam occurs as the atoms collide with the electrons, leaving a positive ion beam. These ions are accelerated to 1500 V and pass through the cesium oven. The cesium charge-exchange reaction is utilized to add two electrons to the deuterium ions. Efficiencies of about 10% for conversion from positive to negative beam are observed. The resulting negative beam is then ejected into the accelerator.

Due to the geometry of the sextupole magnetic fields, the beam emerges with the symmetry axis of its polarization along the axis of the source. Since experiments can require an arbitrary direction of the symmetry axis, a Wien filter is utilized to orient the spin direction. A magnetic field is used to rotate the spin direction and a perpendicular electric field used to prevent deflection of the beam. In this experiment, the polarization symmetry axis was rotated perpendicular to the beam axis and oriented along the vertical y-axis. This required a magnetic field of 1953 G. The polarized deuteron beam then exits the ABPIS and enters the TUNL low energy beam transport facility. The beam has an energy of 80 keV, corresponding to the frame voltage of the source.

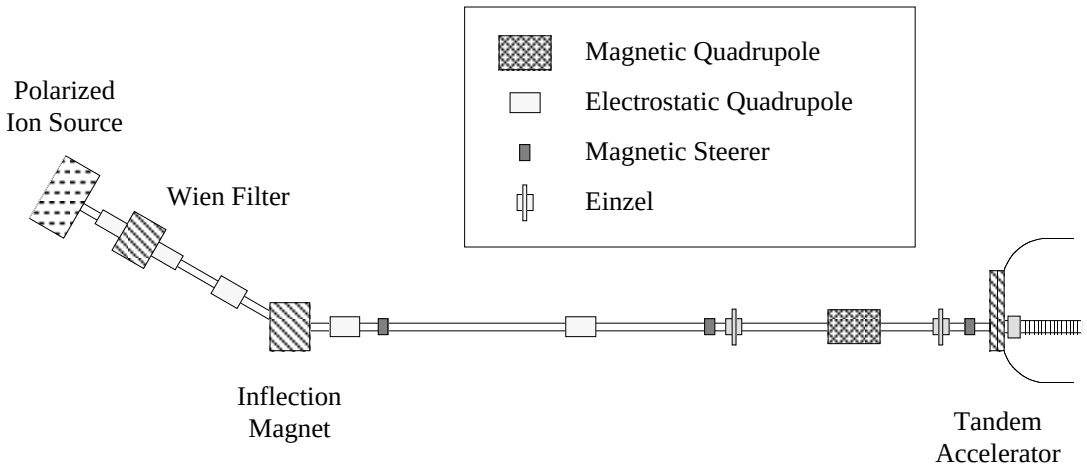

Figure 3.4: The TUNL low energy beam transport facility.

3.2.2 Beam Transport

The charged particle beam is transported from the ABPIS, through the accelerator, and into the experimental area. The low energy beam transport facility is shown in Figure 3.4. Upon exiting the Wien filter, the beam passes through a 30° analyzing magnet and is focused through a series of electrostatic quadrupoles, magnetic quadrupoles, and Einzel lenses before injected into the accelerator. Typical currents of 5–7 μA of polarized beam were observed on the low energy Faraday cup.

The accelerator is a High Voltage, Inc. Tandem Van de Graaff model FN. It accepts negative beam and accelerates it towards the positive potential at the terminal. The beam passes through a carbon foil removing both electrons, and is then accelerated away from the positive terminal [VdG60]. The energy of the beam is therefore $2eV_{Terminal}$. The terminal is encased in a tank containing a mixture of nitrogen, carbon dioxide, and sulfur hexafluoride. Two tubes consisting of alternating glass and stainless steel plates connect the terminal to each end of the tank and serve both as a beam pipe and voltage divider circuit. The terminal is biased by two pelletron charging systems and controlled through a corona feedback system. A beam transmission efficiency of about 70% was observed through the

accelerator for energies used in this experiment.

The positive beam emerges from the accelerator and is transported to the experimental area through the high energy beam transport facility shown in Figure 3.5. The beam is analyzed and deflected 59° towards the polarized target facility. The magnetic field of the analyzing magnet fixes the energy of the beam. The magnetic field is regulated with feedback from a nuclear magnetic resonance probe. A pair of tantalum slits are located at the exit of the analyzing magnet for energy control of the beam through the corona feedback circuit. The beam is then transported directly to the neutron production target using magnetic steerers and magnetic quadrupoles to steer and focus the beam. Three sets of tantalum slits are connected through feedback circuits to magnetic steerers to control the position of the beam. A NEC beam profile monitor allows monitoring of the shape of the beam. The third set of feedback slits are located directly in front of the neutron production target and fixes the position of the beam on the target. Typical beam currents on target were 0.5–2.0 μA.

3.2.3 Spin Transport

The spin of the deuteron beam is rotated by magnetic fields due to the interaction of the field with the deuteron's magnetic moment. Therefore, the spin rotation due to the analyzing magnets must be considered. For the time-reversal measurement, the spin is chosen to be along the vertical y-axis, the same direction as the magnetic fields in the bending magnets. Since the spin will precess about the direction of the magnetic field, the direction of the polarization symmetry axis is unchanged when the beam reaches the target. However, measurements of false T-violating effects (Section 4.4) require placing the spin of the deuteron beam in the x-z plane, which will undergo precession.

If a beam with non-zero spin I, charge q, mass m, and magnetic moment μ is deflected through a bending magnet of angle θ, spin components perpendicular to the magnetic field will precess through an angle

$$\alpha = \frac{\mu m}{I\hbar q}\theta = g\theta. \tag{3.1}$$

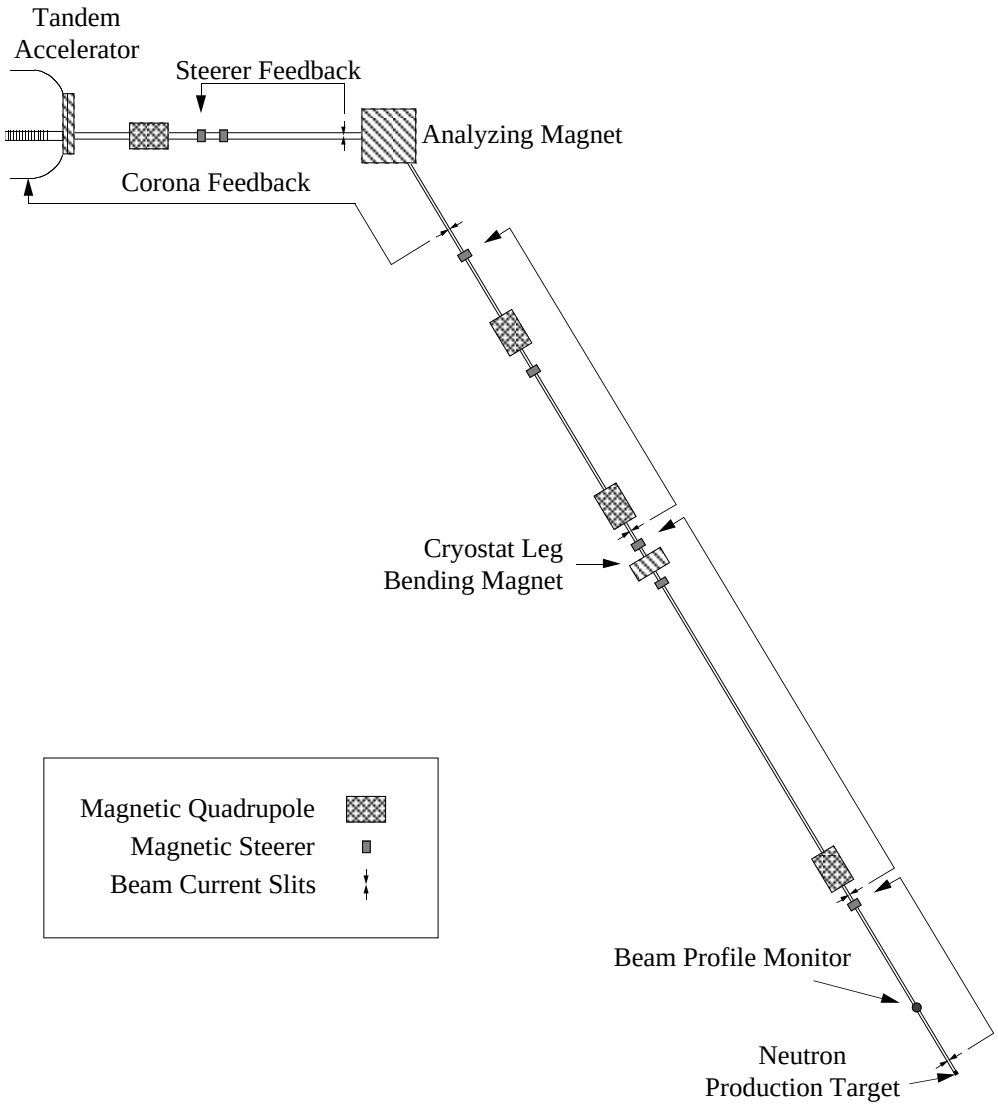

Figure 3.5: The TUNL high energy beam transport facility.

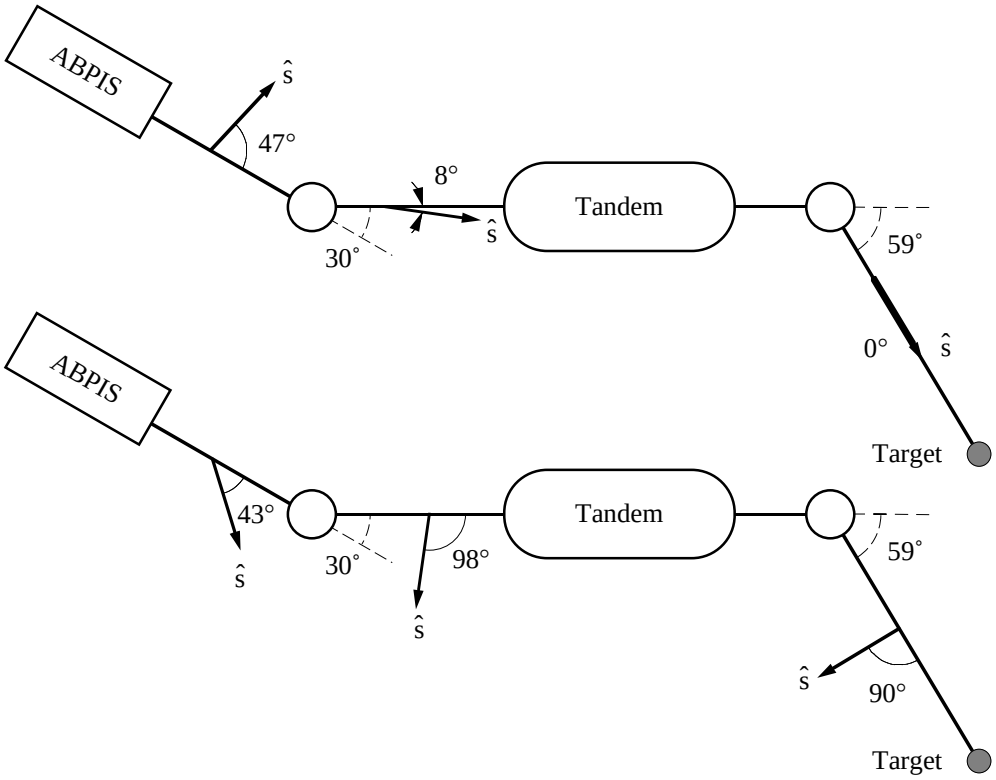

Figure 3.6: Spin precession of the deuteron beam during transport.

For deuterons, $|g| = 0.857$, and the direction of the precession is given by the sign of the charge of the beam. For example, if a negative beam enters a bending magnet at an angle ϕ, it will emerge at an angle ϕ' where

$$\phi' = \phi + \theta(1 - g). \tag{3.2}$$

A pictorial representation of the orientation of the polarization symmetry axis (spin-axis) required to obtain the spin-axis along the x-axis or z-axis at the target is shown in Figure 3.6. A Wien filter magnetic field of -850 G was used for the x-axis orientation and 1166 G for the z-axis orientation. The direction of the Wien filter was rotated 90° with respect to the direction used in producing vertically polarized deuterons.

3.3 Neutron Production and Detection

3.3.1 Neutron Production

When a polarized deuteron beam strikes a deuterium gas target, a polarized neutron beam is produced. The outgoing neutron flux is proportional to the incident deuteron flux and the density and thickness of the production target. The time-reversal measurement requires the highest possible neutron fluxes. To achieve this, the neutron production target was designed for high density and thickness. The ^{2}H(d, n)^{3}He reaction has $Q = 3.269$ MeV.

Three factors determined design of the most efficient gas cell: density and thickness of the gas, energy spread of the beam, and solid angle considerations. Standard deuterium gas cells at TUNL operate with a maximum of 8 atm (1.3 mg/cm^3) of deuterium gas at room temperature. Typical lengths are, at most, 6 cm giving the product $\rho t = 7.9$ mg/cm^2. For this experiment, the density of the gas is increased by cooling the cell with liquid nitrogen while maintaining 8 atm of pressure. The fixed size of the holmium target and the entrance window of the gas cell determines the solid angle (Section 3.3.2). A shorter cell allows a larger solid angle and is therefore preferred. The length of the cell combined with the density of the gas also determines the energy spread of the neutron beam. The length is chosen to correspond to a 2.5 MeV energy spread in the beam with 8 atm of gas. A longer room temperature gas cell could have been designed to give the same product of ρt, but the effective solid angle would have been greatly reduced.

The final design is 3.81 cm long and 0.851 cm diameter. The beam enters the cell through a 15.2 μm Havar foil and the deuteron beam is stopped by a 0.51 mm gold cylindrical tube surrounding the gas and a 0.51 mm foil on one end. The incoming beam is collimated by four tantalum slits forming a 0.625 cm diameter beam 5.91 cm in front of the Havar foil. These slits are connected to feedback steerers to center the beam on the Havar foil and prevent deuterons from hitting the copper surrounding the gas cell. Figure 3.7 depicts a cross sectional view of the gas cell and beam collimation.

The cell is cooled to liquid nitrogen temperatures by a coldfinger connecting the

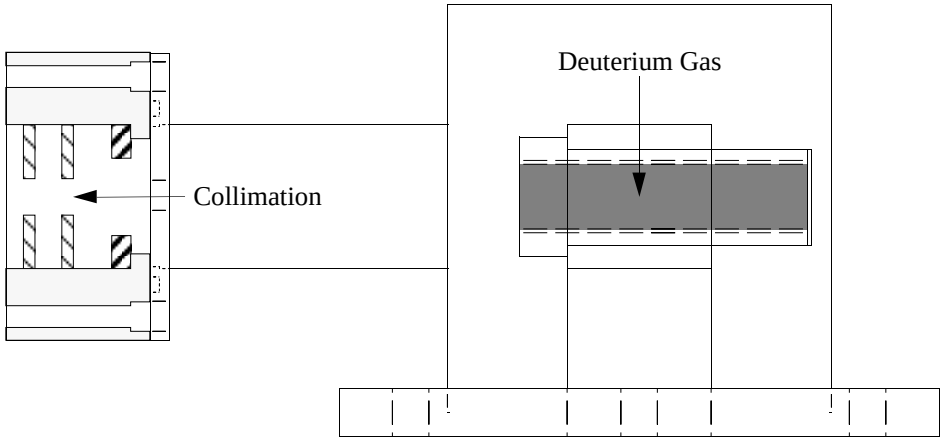

Figure 3.7: Cross sectional view of the deuterium gas cell and collimation (actual size).

cell to a 25 l liquid nitrogen bath. The cooling system of the cell is shown in Figure 3.8. The copper coldfinger is mechanically clamped to the gas cell and extends 71 cm to the liquid nitrogen. A base temperature of 86 K is obtained with 8 atm gas and no beam. The temperature of the gas cell is monitored with a calibrated 1000 Ω (at 0 °C) platinum thermometer attached to the gas cell and regulated using a 5.0 Ω heater thermally anchored to the cell. The heater is powered by a locally designed temperature controller similar to a Linear Research LR-130. Beam currents of up to 2.0 μA are observed at 3 MeV, adding up to 6 W of heat to the cell. To minimize systematic effects in the normalized detector asymmetry due to beam heating effects (discussed in Appendix D), the temperature of the gas cell is stabilized at 168 K. Variations in temperature are observed to be less than 0.5 K with beam on the cell.

The cell is housed in a thin-walled stainless steel vacuum can that connects to the vacuum of the beam line. The cell is pumped by both the beam line vacuum pumps and by activated charcoal surrounding the coldfinger.

The cell was filled using the system shown in Figure 3.9. Deuterium gas of 99.9% purity is filtered through a liquid nitrogen cooled cold trap containing activated charcoal. The cell is filled to 5 atm of gas at room temperature, cooled to 168 K, and then pressurized

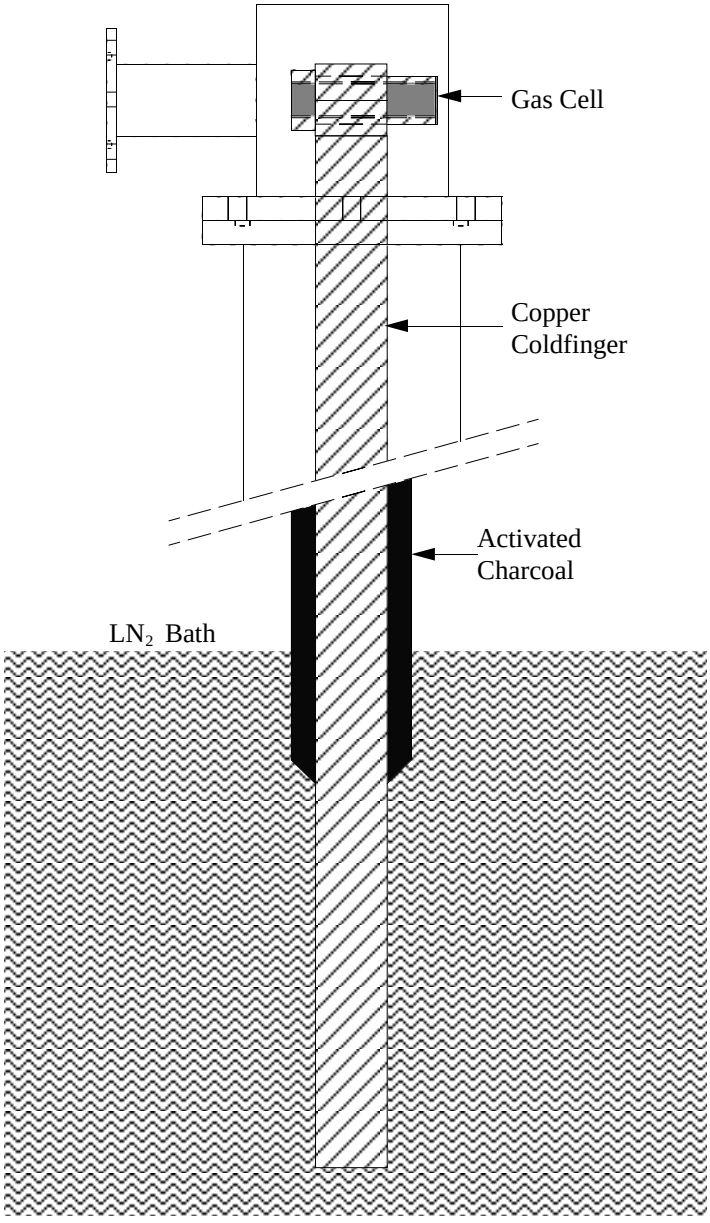

Figure 3.8: Cooling system for the deuterium gas cell.

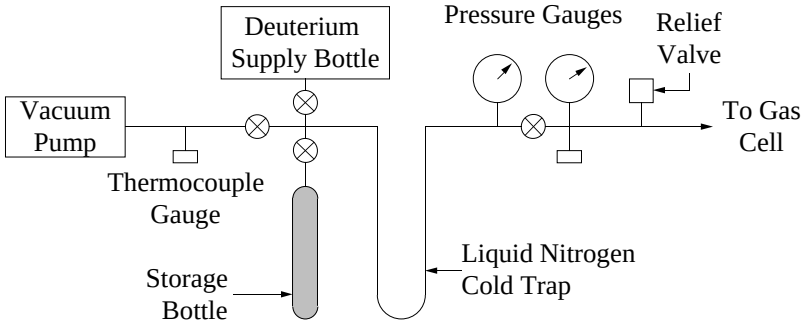

Figure 3.9: Gas handling system for the deuterium gas cell.

to 8 atm. The gas enters the cell through a 1/8" OD stainless steel tube thermally anchored to the coldfinger. Once filled, the cell is isolated from the filling system, fixing the volume of the gas. The pressure is monitored and a relief valve is present to protect the Havar foil separating the gas from the beam line vacuum. The relief value was set to open at 8.5 atm.

With a gas thickness of $\rho t = 8.84$ mg/cm^2, a 4.86 MeV deuteron beam is required to produce a neutron beam with an average energy of 5.9 MeV. The 59° analyzing magnet was set to a field of 0.736400 T, requiring a terminal voltage of $V_{Terminal} = 2.39$ MV. The energy losses of the deuteron beam in the gas cell produce an energy spread in the neutron beam. This spread is calculated using the computer code BABEL [Bow82]. For an incident deuteron beam with energy 4.9 MeV, the energy spread of the neutron beam was calculated to be ± 1.3 MeV with an average energy of 5.9 MeV. Energy losses from the Havar foil and deuterium gas are summarized in Table 3.1. The neutron beam energy was verified by locating resonances in oxygen near 6 MeV using the procedures described by Wilburn [Wil93]. The calculations from BABEL agree with the measured energy values to within 100 keV.

3.3.2 Neutron Collimation

An open geometry is used in this experiment with the detectors located such that neutrons are not detected unless they pass through the holmium target. The solid angle

Location	E_d	E_n
Havar Entrance	4.86	
^{2}H Entrance	3.83	7.10
^{2}H Center	2.60	5.86
^{2}H Exit	1.36	4.55
$\bar{E}_n$(spread)	5.86 (2.55)	

Table 3.1: Deuteron and neutron energies in the deuterium gas cell. Energies are given in MeV.

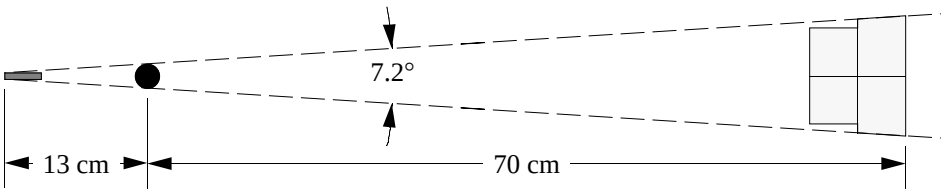

Figure 3.10: The neutron solid angle subtended by the 0° detectors.

is fixed by the entrance window of the deuterium gas cell and the holmium target. The locations of the gas cell, target, and 0° detectors are shown in Figure 3.10, with the dashed lines depicting the acceptance angle. The detectors are placed 70 cm directly behind the target and subtend a solid angle of 15.8 msr.

Monte-Carlo calculations of the inscattering from surrounding material and the small angle scattering within the holmium target were performed using the program MCNP [JFB93]. These calculations are presented in Appendix B. They indicate that less than 1% of the counts arise from small angle scattering from the holmium target and less than 1% of the counts arise from scattering from surrounding material. These MCNP calculations were important in confirming estimates of the neutron fluxes and in estimating cross-talk between adjacent neutron detectors.

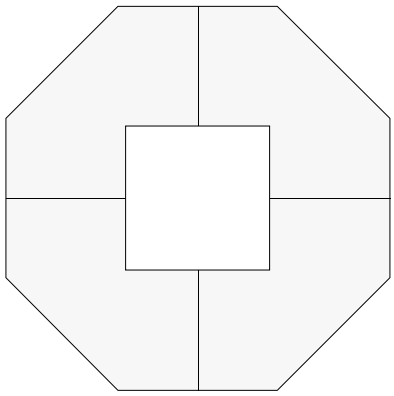

Figure 3.11: Cross-sectional view of the monitor scintillator array (actual size).

3.3.3 Neutron Detection

A four-detector array of neutron detectors monitors the neutron flux emerging from the gas cell. The scintillation material is machined into four segments forming a square opening around the solid angle of the beam. The detectors thus monitor a "halo" of the beam surrounding the solid angle. Pilot-U scintillation material [NET] is used to obtain short scintillation pulses. Pilot-U has a 1.36 ns decay constant, a density of 1.032 g/cm^3, and ratio of H:C atoms of 1:1.1. A cross-sectional view of the scintillator array is shown in Figure 3.11. The opening forms a square 1.9 cm on edge and the scintillators are 1.27 cm thick.

The scintillators are connected to the photomultiplier tubes through highly polished lucite light guides. The guides are 2.54 cm long, 2.86 cm diameter on one end, and 1.27 $\times$ 2.10 cm on the other end. The connections between the photomultiplier tubes, light guides, and scintillators are made with Bicron BC-630 optical grease [Bic] and mechanically pressed together. The outer surfaces of the light guides and scintillators are covered with aluminum foil for light reflection and wrapped with electrical tape to seal out external light.

The four phototubes extend from the light guides perpendicular to each other at a 45° angle with respect to the vertical axis. Positioning the phototubes along the vertical

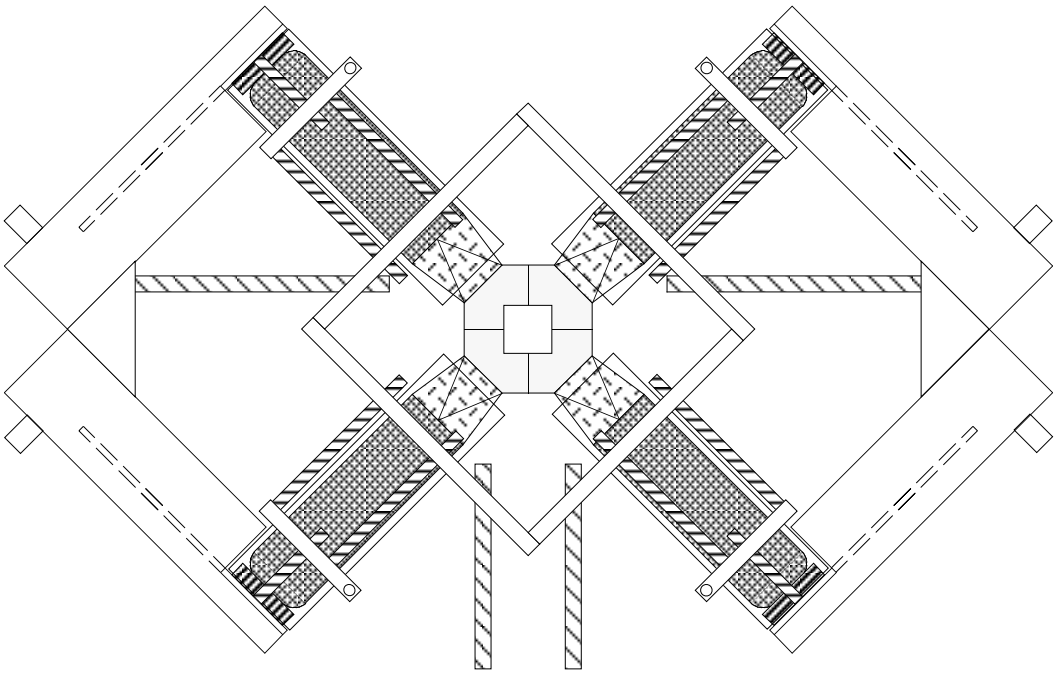

Figure 3.12: Monitor detector assembly

and horizontal directions is not possible due to the location of the dilution refrigerator. The phototubes are Hamamatsu R-1398 [Ham94], 1-1/8" head-on type photomultiplier tubes, which have a 10-stage current amplification, a maximum anode to cathode voltage of -1900 V, and a rise time of 2.0 ns. The maximum anode to cathode current is 0.2 mA, which ultimately determines the maximum counting rates. The tubes are biased between -1000 V and -1100 V using a LeCroy HV4032A power supply, and connected to a transistorized voltage divider base. A Mumetal shield surrounds each base to minimize magnetic fields. The four detectors are assembled in the configuration shown in Figure 3.12. This assembly operates reliably at count rates up to 15 MHz.

A similar four-detector array was constructed for the 0° transmission detector. The scintillation material is Pilot-U and a polished lucite light guide provides the transition from the $6.35 \times 6.35 \times 10.2$ cm thick scintillator to the 2" diameter photomultiplier tube. The tubes are Hamamatsu 1828-01 [Ham94], 12-stage tubes with typical rise times of 1.3 ns.

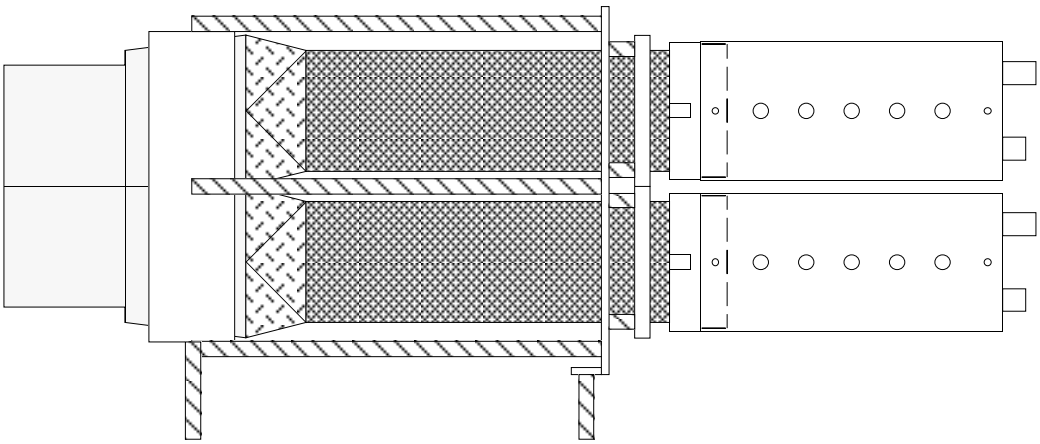

Figure 3.13: 0° detector assembly

The tubes have a maximum anode current rating of 0.2 mA and maximum voltage rating of −3000 V. They are surrounded with magnetic shielding and typically biased between −1600 V and −1700 V with a LeCroy HV4032A power supply. A side view of the 0° detector array is shown in Figure 3.13. This array operated reliably at count rates up to 10 MHz.

Due to the high counting rates in the monitor and 0° detector arrays, a standard voltage divider circuit can not supply enough current to maintain linearity in the high gain stages of the photomultiplier tubes. A transistorized base is used to minimize voltage deviations and thus gain nonlinearities. The transistors are chosen to have a high forward current ratio ($\beta = 65$) while withstanding high voltage biases. The resistor values are selected to obtain the standard voltage division recommended by Hamamatsu [Ham94] and capacitors added to provide ample charge for pulse operation. A schematic of the transistorized voltage divider circuit for both sets of detectors is provided in Appendix C (Figures C.1 and C.2).

The voltage divider circuits are assembled on a printed circuit board. The components are matched to assure consistency and attached directly to the photomultiplier tube bases. The monitor circuit is mounted inside a chamber machined to both house the circuit board and serve as part of the detector mounting hardware. The voltage distribution for

a fixed input voltage applied to the individual circuits are given in Tables C.1 and C.2 of Appendix C. The detectors are electrically isolated to maintain a single ground connection for the electronics.

3.3.4 Neutron Polarimeter

The neutron polarization is monitored using the left-right asymmetry from the $^2\mathrm{H}(\vec{\mathrm{d}},\vec{\mathrm{n}})^3\mathrm{He}$ reaction. The polarimeter consists of two liquid scintillator detectors (NE-213) placed at $\pm 36^\circ$ with respect to the beam direction 66 cm from the cell. The detectors are mounted in the horizontal (x-z) plane and face the center of the deuterium gas cell. The scintillators are $4.5 \times 15.8 \times 7.6$ cm thick and are painted with reflective paint. Each scintillator is connected to a Hamamatsu type H1161 phototube [Ham94] through a polished lucite light guide. The phototube base uses a standard voltage divider circuit, and are biased to -1650 V using a Fluke 415 high voltage supply.

3.4 Target

3.4.1 Holmium

Holmium is chosen as the target nucleus because it is monoisotopic (^{165}Ho) and single crystals have a large internal hyperfine field. The large hyperfine field allows cryogenic alignment of the nuclei in the absence of an external magnetic field. In addition, large metallic single crystal samples are commercially available, making holmium an ideal nucleus for the five-fold correlation time-reversal measurement.

The ^{165}Ho nucleus has spin and parity $I^\pi = \frac{7}{2}^-$. Holmium is a rare earth element which exhibits unique magnetic properties. The crystal structure of metallic holmium is hexagonal close-packed. Below 131 K, holmium undergoes a magnetic-ordering transition to an antiferromagnetic state. A second transition occurs to a ferromagnetic state below 20 K [Koe66]. In the ferromagnetic state, the magnetic moments are directed 10° out of the a-b basal plane and are parallel within a given plane. In successive planes, the moments

are rotated 30° about the c-axis, forming a cylindrically symmetric spiral structure about the c-axis.

Holmium has two unpaired $4f$ electrons, which generate a large internal hyperfine field. Holmium has both a magnetic dipole and electric quadrupole moment, both of which interact with the field, to create a hyperfine energy splitting between nuclear levels. The internal field orients the nuclei if the thermal energy is comparable to or less than the energy splitting. In the absence of an external magnetic field, nuclear alignment with respect to the c-axis occurs when the sample is cooled below 1 K.

The interaction of the nuclear magnetic dipole moment with the effective hyperfine field can be modelled by the Hamiltonian $\mathcal{H} = \frac{\mu B}{I} I_z$, with energy eigenvalues $E_m = A\, m$. The electric quadrupole interaction is modelled by the Hamiltonian $\mathcal{H} = P[I_z^2 - \frac{1}{3}\boldsymbol{I}^2]$ and has energy eigenvalues $E_m = P[m^2 - \frac{1}{3}I(I+1)]$. The coefficients A and P in

$$E_m = Am + P[m^2 - \tfrac{1}{3}I(I+1)] \tag{3.3}$$

have been determined empirically by Krusius *et al.* [Kru69]. They found $A = 0.319 \pm 0.003$ k (eV) and $P = 0.004 \pm 0.001$ k (eV).

The probability that a given nucleus is in substate m is given by the Boltzmann distribution function

$$a_m = \frac{\exp(-E_m/kT)}{\sum_m \exp(-E_m/kT)}. \tag{3.4}$$

The tensor $\tilde{t}_{K0}^{planar}$ describing the alignment of the nucleus along the axis of its magnetic moment is given by [Kra86]

$$\tilde{t}_{20}^{planar} = 6\sqrt{5}\hat{I}\sqrt{\frac{(2I-2)!}{(2I+3)!}}\left[\sum_m m^2\, a_m - \frac{1}{3}(I+1)\right]. \tag{3.5}$$

Combining Equations 3.3, 3.4, and 3.5 gives the tensor alignment as a function of temperature and is shown in Figure 3.14. The tensor alignment $\tilde{t}_{20}^{planar}$ reaches a maximum value of $\sqrt{\frac{7}{3}}$ at $T = 0$ K and 96% of the maximum at 100 mK.

The symmetry axis of the alignment is directed along the c-axis of the crystal and only the c-axis components of the magnetic moments contribute to this alignment. The

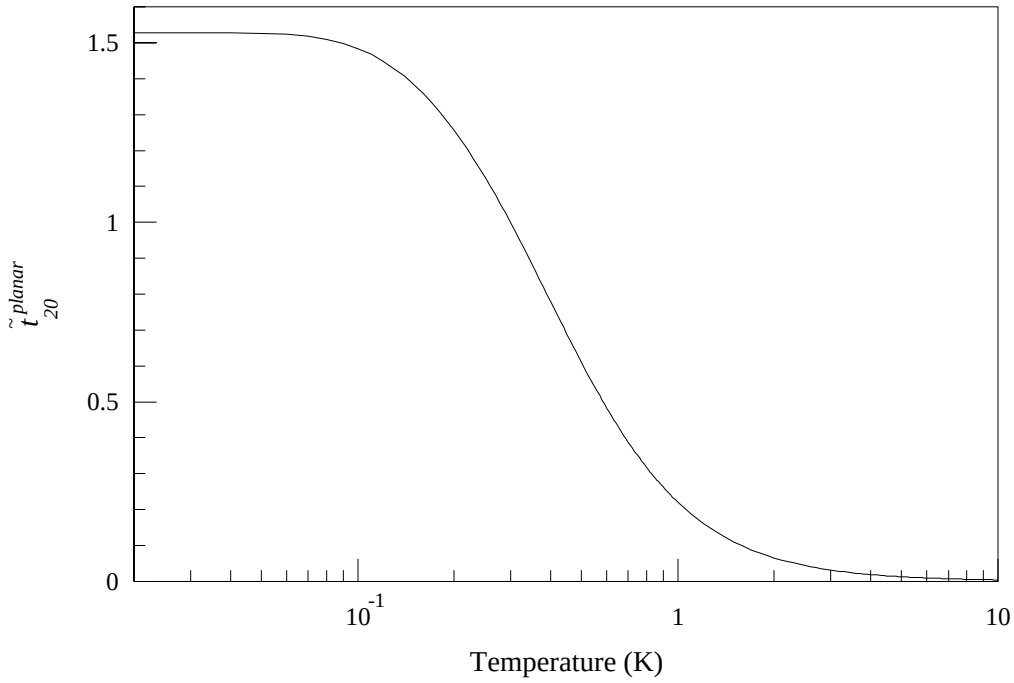

Figure 3.14: $\tilde{t}_{20}^{planar}$ as a function of temperature.

polarization tensor along the symmetry axis is related to the planar alignment tensor using Equation 2.2

$$\tilde{t}_{20} = \mathrm{P}_2(\cos 80^\circ)\, \tilde{t}_{20}^{planar}, \tag{3.6}$$

where 80° corresponds to the angle between the magnetic moments and the c-axis of the crystal. The maximum value of $\tilde{t}_{20}$ for holmium is therefore

$$\tilde{t}_{20} = \sqrt{\frac{7}{3}}\, \mathrm{P}_2(\cos 80^\circ) = -0.695. \tag{3.7}$$

The single crystal sample used for this experiment was grown by Ames Laboratory [Ame] and machined in a cylindrical shape with the c-axis perpendicular to the cylinder axis. The 101.6 g sample is 99.8% holmium. The cylinder is 2.29 cm diameter and 2.8 cm in height.

The crystal is cleaned using an electropolishing technique. First, the oxide surface layer of the crystal is removed with fine sandpaper and an acid solution. The solution

consists of a mixture of 20 ml lactic acid, 5 ml phosphoric acid, 10 ml acetic acid, 15 ml nitric acid, and 1 ml sulfuric acid. The acid solution is applied with a cotton swab and rinsed with ethanol following the techniques given by Roman [Rom65]. The electropolishing apparatus consists of a stainless steel beaker (used as the cathode) holding a solution of 1–2% perchloric acid in methanol. The beaker is suspended in a dry-ice/acetone bath. The holmium is suspended in the perchloric acid solution and a 0.5 A current applied between the holmium sample and the beaker. The electropolishing takes approximately five minutes. The sample is removed from the bath, rinsed first in the dry-ice/acetone bath and then with methanol. The electropolishing technique is described by Beaudry *et al.* [Bea78]. In order to assure good thermal contact between the holmium and the copper mounting holder, a layer of gold is evaporated onto the surface of the holmium.

3.4.2 Dilution Refrigerator

The holmium sample is cooled with the aid of a ^{3}He – ^{4}He dilution refrigerator. The refrigerator is a homebuilt model, similar in design to a SHE model DRI-420 commercial refrigerator. It has a cooling power of 85 μW at 110 mK with a base temperature of 42 mK. A central shaft extends from room temperature to the sample holder to allow the target to be rotated. The design and construction of the refrigerator is discussed by Koster [Kos90] and this section serves only to overview the dilution refrigerator in general.

In order to understand the basic principles behind the operation of a dilution refrigerator, we must first look at the properties of a ^{3}He – ^{4}He mixture. Depending on the relative concentrations of ^{3}He and ^{4}He, the mixture can exist either as a normal fluid or superfluid. As the temperature of the mixture is lowered, a phase separation occurs which separates the mixture into two components: a ^{3}He-rich solution which "floats" on top of a heavier ^{4}He-rich solution. In the operating regime of a dilution refrigerator (below 500 mK), the ^{3}He-rich layer is essentially pure ^{3}He, while the ^{4}He-rich layer is a mixture of approximately 94% ^{4}He and 6% ^{3}He. Since below 500 mK, superfluid ^{4}He is essentially in its quantum mechanical ground state, the ^{4}He-rich phase can be thought of as a ^{3}He gas in

an inert ^{4}He background. The dilution refrigerator (DR) utilizes the latent heat involved in this phase separation to cool samples to temperatures as low as 5-10 mK.

The refrigerator consists of four main components: the coldplate, still, heat exchangers, and mixing chamber. A block diagram showing the principal parts of a DR is shown in Figure 3.15. The phase separation occurs in the mixing chamber and continuous cooling is possible through recirculation of ^{3}He.

The still contains the ^{4}He-rich solution, and when pumped on, ^{3}He is preferentially removed due to the lower vapor pressure of the ^{3}He. In order to maintain equilibrium, ^{3}He will continuously diffuse across the phase boundary in the mixing chamber into the ^{4}He-rich phase. By connecting a sample to the mixing chamber, the latent heat required for the ^{3}He to cross the phase boundary can be removed from the sample, allowing the sample to reach milli-Kelvin temperatures. Heat exchangers are required to minimize the heat load from the incoming ^{3}He and the coldplate precools the incoming ^{3}He to 1.2 K before it enters the heat exchangers. Quality heat exchangers are essential in achieving low temperatures.

The DR is housed inside of a liquid helium cryostat. The cryostat consists of a liquid nitrogen shield surrounding a liquid helium bath. A vacuum jacket surrounds the liquid nitrogen bath, the liquid helium bath, and the dilution refrigerator.

3.4.3 Rotation Apparatus

A shaft extending from the top of the cryostat to the sample allows for rotation of the holmium sample while cold [Kos92b]. The hardware for the rotation apparatus consists of a stepping motor, a 25:1 gearbox, a shaft encoder, and a computer controller. The stepping motor is connected to the central shaft through an anti-backlash 25:1 gearbox. The shaft enters the vacuum can through a rotating fluid seal and extends roughly 200 cm to the target. The shaft consists mainly of 3/16" OD thin-walled stainless steel tubing, separated by solid copper couplers to minimize the thermal radiation from room temperature entering through the shaft. The shaft extends to directly above the target, connecting to the sample holder.

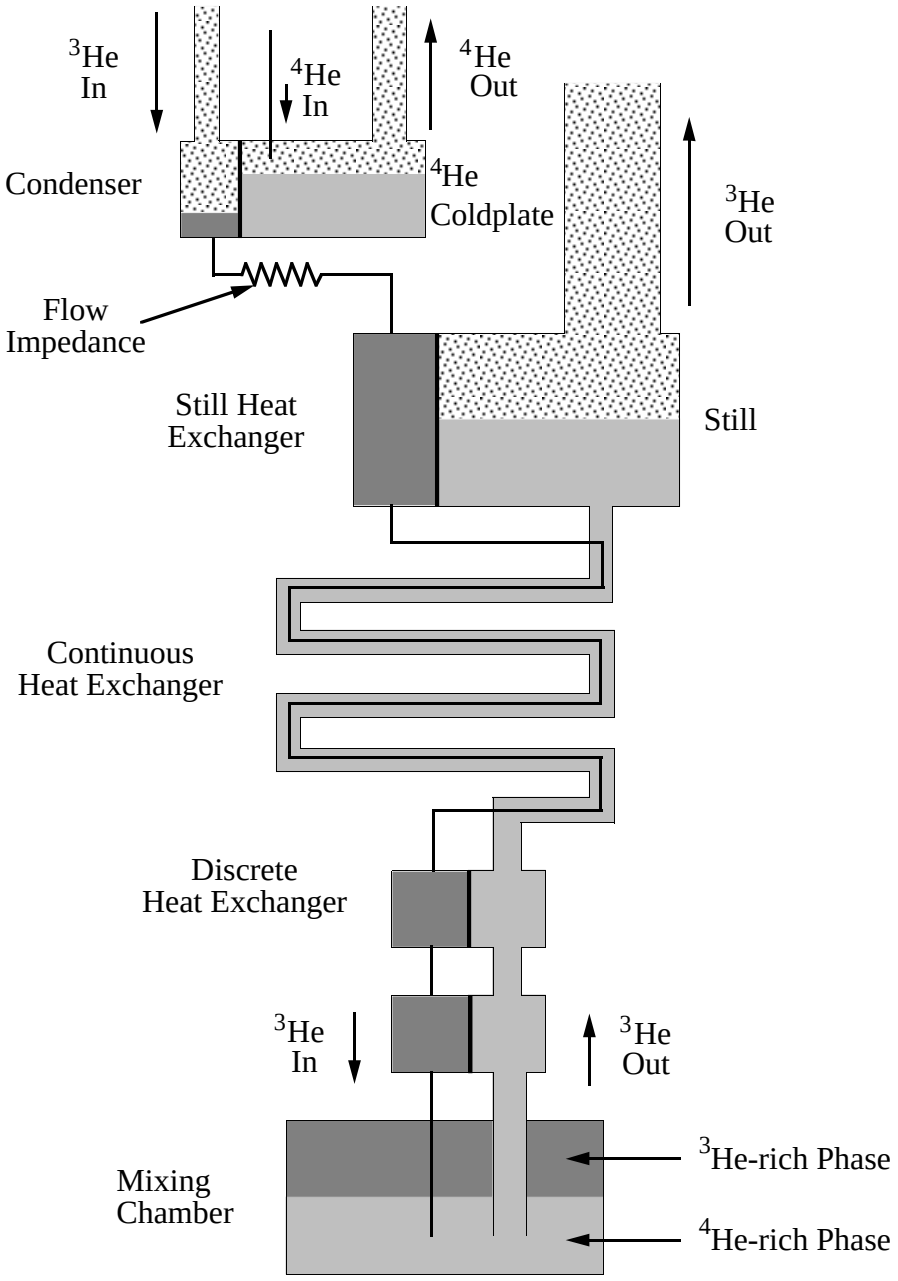

Figure 3.15: Schematic of a dilution refrigerator.

The sample holder is shown in Figure 3.16. The central shaft extending from the top of the refrigerator connects to a precision ground 0.5000" stainless steel bearing shaft (Berg S8-70 [Ber]). The shaft passes through two greaseless, high-precision, stainless steel bearings (Berg B2-11-U [Ber]) mounted directly above the sample to insure the stability of the target during rotation. The deviations of the sample during rotation were less than .005 cm side-to-side movement and .007 cm vertical displacement. The angular position is reproducible to within 0.16°.

The holmium sample is mounted into a copper holder machined .003 cm smaller than the sample. The sample is mounted using a press-fit connection into the cylindrical holder. The holmium is cooled in liquid nitrogen and then placed into the heated copper holder. When thermal equilibrium is reached, the sample is firmly inside the holder. When the sample and holder are cooled by the refrigerator, the larger thermal expansion coefficient of the copper further tightens this connection.

A small magnet is mounted inside the bearing shaft for positioning purposes. The field from this magnet is measured with a Hall probe and used to verify angular positioning of the target. The field varies with angle as $\cos\theta$.

The sample holder is connected to the mixing chamber through three copper braids. Each braid consists of 110 strands of .016 cm copper wire extending 15 cm. The braids are long enough to insure a full 360° rotation of the target.

The heat capacity of holmium at 300 mK is 7.3 J/mole-K [Kru69]; 3.6 J of heat must therefore be removed in cooling the sample from 1.2 K to 100 mK. Good thermal connections between the mixing chamber and sample are essential. The largest thermal resistance was in the braids connecting the mixing chamber to the sample holder. This resistance is calculated to be 750 K/W, assuming the screw connections have a thermal resistance of 20 K/W [Lau79]. The sample typically cools from 1.2 K to 100 mK in eight to ten hours.

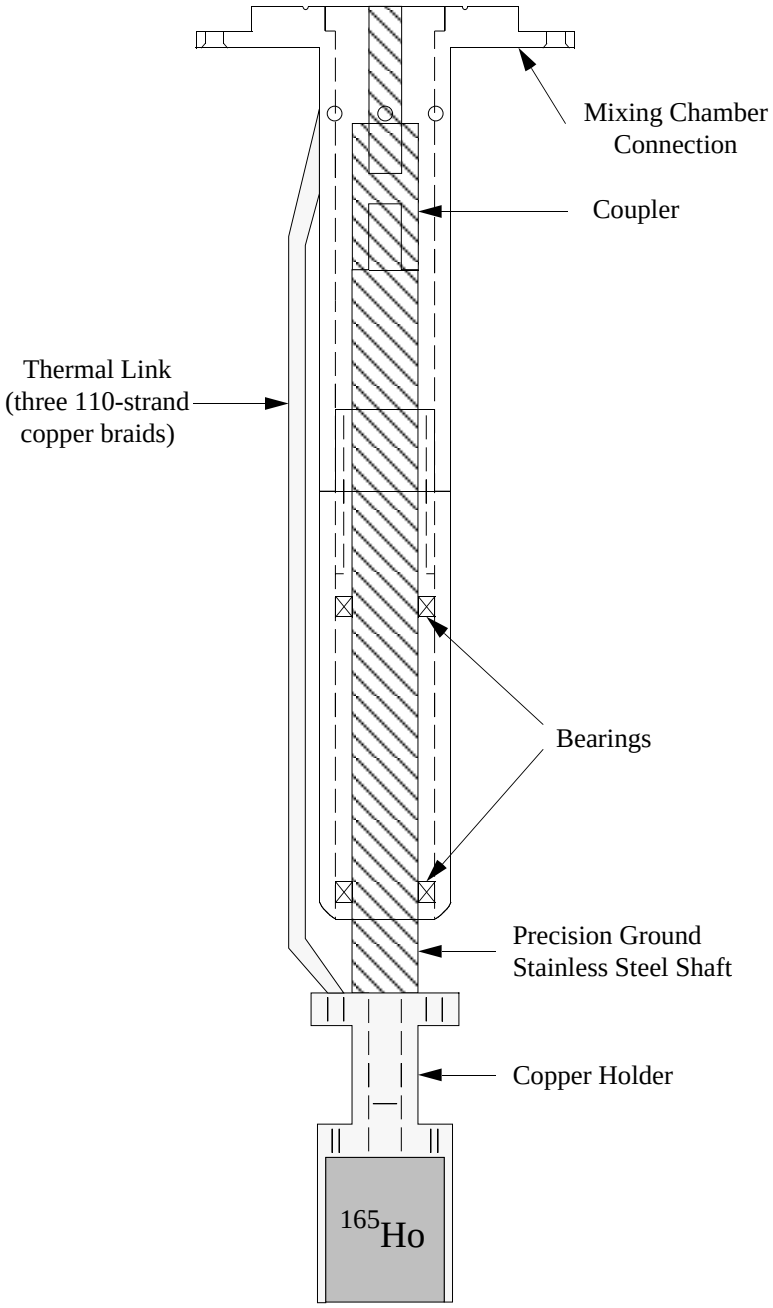

Figure 3.16: The sample holder for the holmium target.

3.4.4 Thermometry

The temperature of the target is measured using resistance thermometry and confirmed by the deformation effect measurements. A calibrated Dale 1000 Ω resistor is mounted to the sample holder and connected to a SHE model PCB conductance bridge. A similar thermometer is connected to the sample holder and used for temperature stabilization. This thermometer is input to a locally designed temperature controller (identical to the one used for the deuterium gas cell temperature control) and drives a 500 Ω metal film resistor connected to the sample holder. The temperature is controlled at 160 mK, corresponding the warmest temperature reached during rotation. Deviations in the sample temperature are less than 2 mK during collection of the data. The thermometers are calibrated against a commercially obtained germanium thermometer.

3.5 Data Acquisition Electronics

Data are taken using the TUNL XSYS [Rob81] data aquisition system running on a DEC μVAX 3200 workstation. Signals are processed using standard NIM electronics and stored using CAMAC modules interfaced to the μVAX using a MBD-11.

The time-reversal measurement utilizes ten neutron detectors, a polarized neutron beam, and a rotating aligned target. Counts from the neutron detectors are routed into different data areas for each neutron spin-state and target alignment angle. Beam current integration is performed and the stability of the electronics is monitored.

The 0° and monitor detector anode signals are transported from the target area to the control room using low loss RG-8 coaxial cables. These signals are fed to a Phillips 708, Octal 300 MHz discriminator and the events above threshold are counted with a Phillips 7132, 32-Channel, 225 MHz scaler. The linear pulses from the detectors are 10 ns full width half maximum and the phototube gains were set to yield maximum pulse heights of −500 mV for the 0° detectors and −150 mV for the monitor detectors (measured using a 50 Ω termination). The discriminator thresholds were set to −40 mV for the 0° detectors

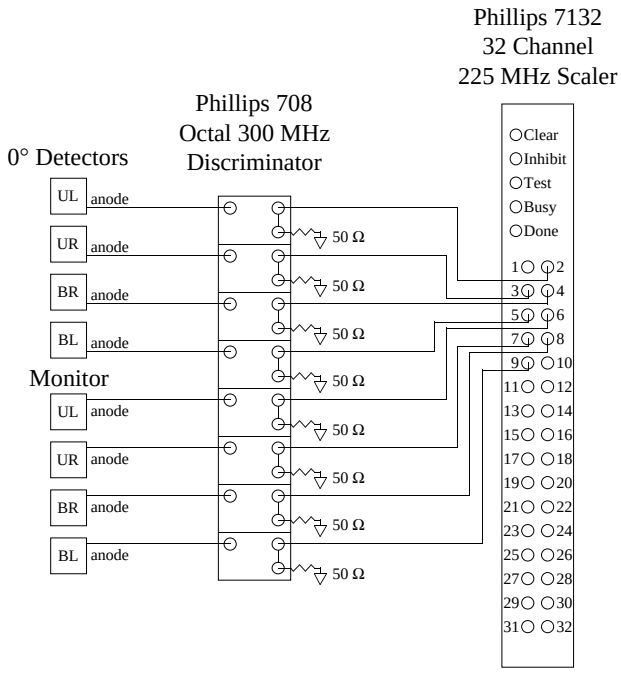

Figure 3.17: Block diagram of the detector electronics

and −25 mV for the monitor detectors and the outputs from the discriminators were set to 10 ns. With 2.0 μA of beam, count rates of 4.4 MHz were observed for the 0° detector array and 14.1 MHz for the monitor detector array. A block diagram of the detector electronics is given in Figure 3.17.

Anode signals from the two polarimeter detectors are fed to a Link 5020 PSD module which discriminates between neutrons and gamma rays. The neutron output signal from the Link module is shaped using a LeCroy 222 gate and delay generator before being counted by the Phillips 7132 scaler. A second LeCroy 222 is configured as a 100 kHz pulser. Its output is ANDed with the live-time output of the Link 5020 module and used for dead-time corrections (N_{gated}). Since the dead-time of the Link 5020 module is approximately 400 ns per event, the dead-time of the system is dominated by this module. The dead-time

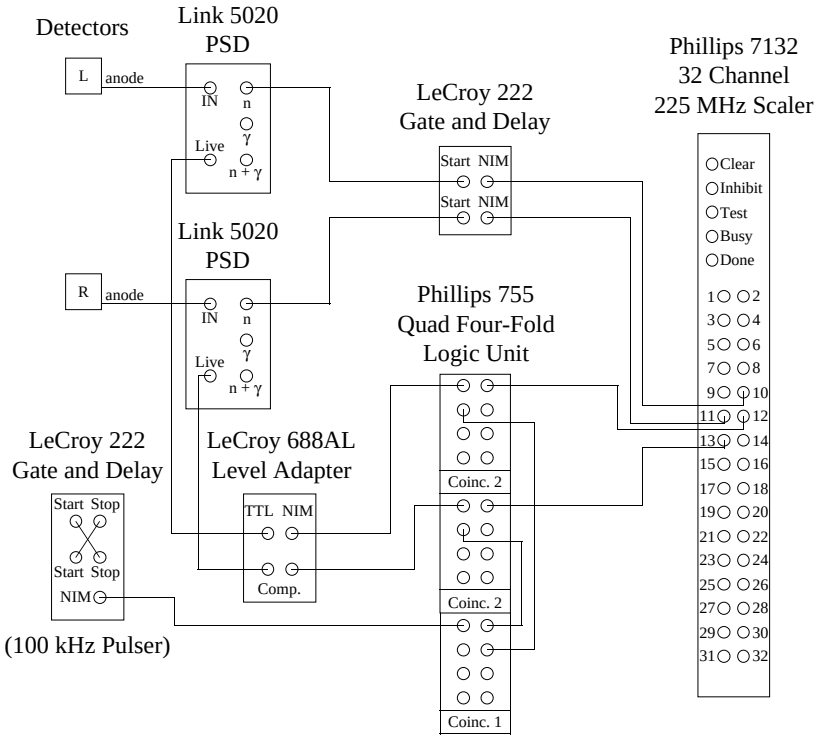

Figure 3.18: Block diagram of the polarimeter electronics

correction factor δ for the polarimeter detectors is calculated using

$$\delta = \frac{N_{pulser}}{N_{gated}}. \tag{3.8}$$

Typical count rates of 70 kHz with dead-times of 10% were observed in each detector. A schematic of the polarimeter detector electronics is given in Figure 3.18.

Beam current integration (BCI) is performed using a TUNL constructed current-to-frequency converter designed by Wilburn [Wil95]. A schematic of the integrator circuit is given in Appendix C (Figures C.7 and C.8). At full scale current, this integrator produces a 500 kHz output pulse train. The charge from the stopped deuteron beam is collected and integrated to monitor the incident flux. A window is set around the beam current to inhibit data collection if the beam current deviates from a set level (typically 20% of the average). Pulses from the integrator are counted using the Phillips 7132 scaler. A block diagram of

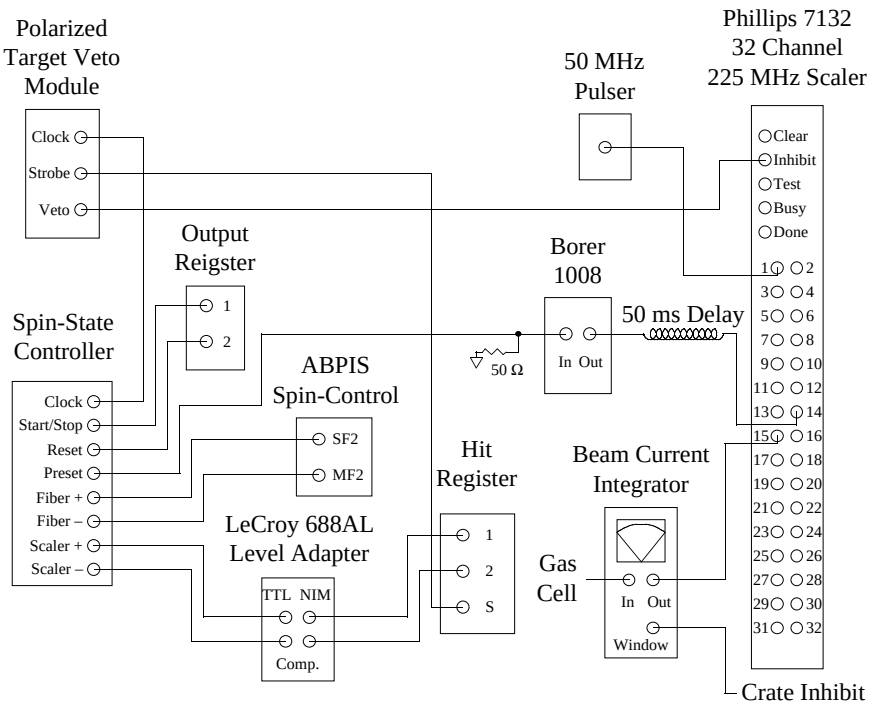

Figure 3.19: Block diagram of the spin-flip timing and beam current integration electronics.

the BCI circuit is included in Figure 3.19.

The neutron spin is toggled every 100 ms in the eight-step sequence $+--+-++-$. Two NIM modules control the spin-flip sequence and the data acquisition system: the TUNL spin-state controller and the polarized target veto module. Circuit schematics for these modules are given in Appendix C (Figures C.3, C.4, and C.5) and the block diagram of the electronics is shown in Figure 3.19.

The spin-state controller (SSC) is driven by an external clock input. Each clock pulse toggles the output of the fiber$^+$ and scaler$^+$ outputs in the eight-step sequence $+--+++-$. The fiber$^-$ and scaler$^-$ outputs are toggled oppositely $(-++-+--+)$. The fiber$^\pm$ outputs (TTL) are connected to the ABPIS transition-oscillator module and used to toggle the RF cavities in the ABPIS to reverse the spin of the deuteron beam (Section 3.2.1). The scaler$^\pm$ outputs are converted to NIM level signals and used to route

the data according to the neutron spin-state. The SSC is inhibited during a CAMAC crate inhibit and is externally reset at the start of each run. The preset output produces a pulse for each eight-step sequence and is used for indexing the spectra.

The polarized target veto module (PTVM) controls the SSC and vetoes the data flow during the time the spins are being flipped. A 50 MHz crystal oscillator is divided down into a 10 Hz clock to drive the SSC. This oscillator is needed to provide the required stability for the circuit. The vetoing is performed in the Phillips 7132 scaler and controlled with the $\overline{\text{TTL}}$ veto output from the PTVM. The veto signal is 7 ms in length, beginning 2 ms before the spin-flip. A strobe pulse (NIM) occurs 1 ms before the spin-flip and is used to set a LAM in the hit register (BiRa 2351) for reading the scalers. A block diagram of the spin-flip electronics is shown in Figure 3.19. A timing diagram of the spin-flip circuit is given in Figure 3.20.

Stability of the electronics is essential in assuring that equal times are spent in each spin-state. A separate 50 MHz oscillator is used as a pulser to test and monitor vetoing of the data. A schematic is given in Appendix C (Figure C.6). The pulses are counted with the Phillips 7132 scaler (see Figure 3.19) and routed according to the neutron spin-state. Eight-step sequences for which the pulser counts differ by more than 100 counts out of 20×10^6 counts in either of the two spin-states are eliminated in the analysis (Section 5.1). The pulser also measures the long-term stability of the circuit.

The target rotation occurs at the end of each run (256 eight-step sequences). The rotation is controlled by an external personal computer connected to a Texas Instruments Model 525 Programmable Controller (TIPC). The angle value is sent to the TIPC from the μVAX using a BiRa 304 isolated output CAMAC module. This output is read by the TIPC and used in a relay ladder logic program running in the TIPC to determine the angle value. The TIPC reads the target angular position of the shaft using the 13 bit binary shaft encoder and compares it with the current angle value. The stepping motor is driven in the appropriate direction to rotate the target. A 22.5° rotation is performed after each run and takes approximately 20 s to complete. Once the angular position is reached,

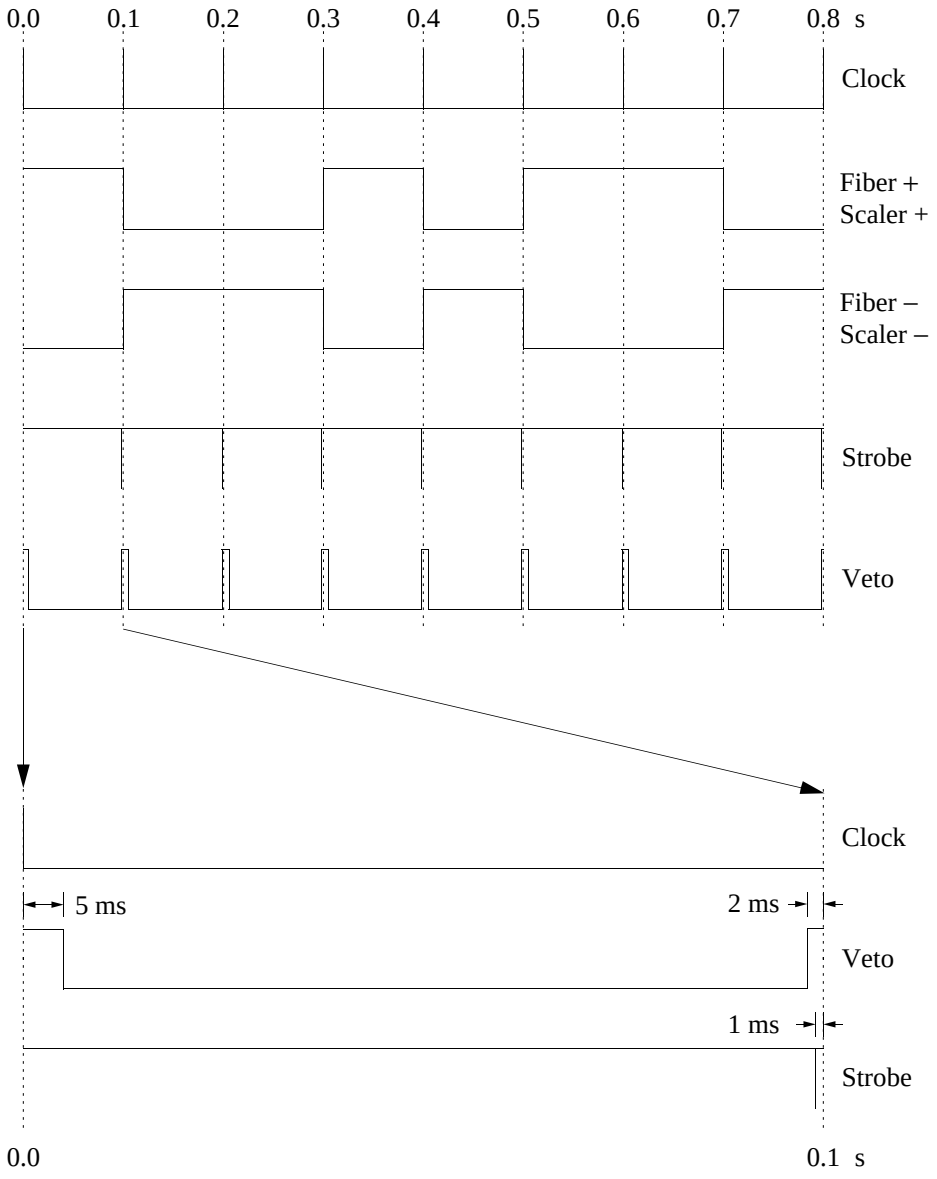

Figure 3.20: Spin-flip timing diagram

the angle is output to a BiRa 322 isolated input CAMAC module and read by the μVAX before data collection begins. Each run lasts approximately four minutes and a complete angular sequence ($-180°$, $-157.5°$, ..., $-22.5°$, $0°$, $22.5°$, ..., $180°$, ..., $-157.5°$) takes approximately two hours.

The data is read by the MBD-11 after each spin-flip. The data are sorted according to the neutron spin-state and stored in the μVAX. The data acquisition system controls the rotation of the target after the Borer 1008 preset scaler has reached 256 eight-step spin sequences. At this time, the data are written to disk and a new run is started. The temperature of the target is stored for each spin sequence using an analog-to-digital converter. The deuterium gas cell pressure and temperature are recorded at the end of each run. Analysis is performed using the XSYS data acquisition system and standard FORTRAN programs.

3.6 Experimental Procedure

Preparation for the FC measurement begins two days prior to the collection of data. The target is first cooled with liquid nitrogen for 12 hours. Next, liquid helium is added to cool the refrigerator and sample to 4.2 K. The ^{3}He is then condensed into the refrigerator and circulated to begin the cooling process. The sample reaches 100 mK in six to eight hours after circulation begins. The following day, the polarized deuteron beam is extracted from the polarized ion source, tuned for maximum intensity and polarization, and then accelerated and transported to the target area.

Measurements begin with a four hour measurement of the deformation effect at 9.4 MeV. Next, the energy of the beam is then lowered to 5.9 MeV where the deformation effect is small for the FC measurement. Data are collected for seven days, stopping every 24 hours to fill the cryostat with liquid nitrogen and liquid helium.

Measurements are taken with the neutron spin direction reversed every 100 ms in the eight-step sequence $+--+-+++-$. The alignment axis of the target is varied every 256 eight-step sequences in the angular sequence $-180° \rightarrow +180° \rightarrow -180°$ in $22.5°$ steps.

This double modulation technique reduces the systematic effects and allows this asymmetry to be measured with high precision.

The final day of this measurement is used to perform measurements of possible T-conserving interactions which could lead to false T-violating asymmetries. Measurements of other parameters needed in the analysis of the data such as the multiple scattering events with the detectors and the ratio of neutron to gamma ray counts are also performed. A second deformation effect measurement is performed to verify the alignment obtained from thermometry and to verify the operation of the rotation apparatus. These measurements are discussed further in Chapter 4.

Analysis of the data is performed off-line at a later time.

Chapter 4

Supplemental Measurements

Analysis of the time-reversal data requires knowledge of various parameters not measurable during the experiment. These include multiple scattering events within the detectors and the background of gamma rays counted. Parameters such as the temperature of the target are known from thermometry, but must be verified using other techniques, and lastly, T-conserving interactions that could mimic a $\sin 2\theta$ angular dependence must be investigated. This chapter serves to present these measurements.

4.1 Multiple Scattering Events

The segmentation of the neutron detectors discussed in Chapter 3 gives rise to multiple scattering events within two or more detectors. These events are counted in multiple detectors, thereby artificially increasing the neutron count rate. Before analysis of the time-reversal data, these events must be removed.

The multiple scattering events — or cross-talk — occurs when a neutron or gamma ray is scattered within one scintillator and then scatters within another. Two counts are therefore stored for one event. The standard mechanism for removing these multiple events is coincidence rejection using NIM electronic logic modules. The large neutron flux into the detectors prohibit the use of such electronics because of the high accidental rate[1] The cross-

[1]The probability that two neutrons arrive in different detectors at the same time, mimicking the cross-talk

talk can however be measured at lower neutron fluxes and a correction factor determined for each detector pair.

The cross-talk measurements are performed at 5.9 MeV (the same energy as the time reversal measurements) using two different beam currents: $I = 1.25$ μA and 0.125 μA. Measurements are performed for both the 0° and monitor detectors. Since the percentage of counts due to cross-talk is directly proportional to the beam current, the accidental rate can be removed by extrapolating to a beam current of $I = 0$ μA.

Data are taken using the detector and discriminator electronics shown in Figure 3.17. The NIM level outputs from the discriminator are connected to a Phillips 755 quad four-fold logic unit, which is used to perform the coincidence measurements. The output of the logic unit is directed into an Ortec 715 counter/timer. The beam current is integrated and routed into the time base of the scaler for beam current normalization.

Four types of measurements are performed: (a) total count rates for each detector, (b) two-fold coincidences between detector pairs, (c) three-fold coincidences, and (d) a four-fold coincidence. These measurements were performed for both detector arrays and for each beam current configuration. The results are summarized in Table 4.1 using the numbering scheme where (1) corresponds to the upper left, (2) the upper right, (3) the lower right, and (4) the lower left detectors with respect to the beam direction. The three- and four-fold coincidence rates are at least two orders of magnitude smaller than the two-fold rate and do not contribute to the total cross-talk. Only the two-fold coincidence rate is therefore used in the analysis of the time-reversal data.

The total number of counts in a detector, N^a, contains the actual yield, N_0^a, plus an additional term due to the cross-talk. Defining $\mathcal{X}(a,b)$ as the cross-talk ratio for a detector pair, the neutron yield for detector number 1 for example is

$$N^1 = (1 + \mathcal{X}(1,2) + \mathcal{X}(1,3) + \mathcal{X}(1,4))\, N_0^1. \tag{4.1}$$

The two-fold coincidence values given in Table 4.1 contain both the cross-talk and accidental rate. We define $\eta(a,b)$ to be the ratio of the number of two-fold coincidences between

effect.

	0°, 1.25 μA	0°, 0.125 μA	Mon., 1.25 μA	Mon., 0.125 μA
Count rate				
1	977612 ± 313	106463 ± 103	2594057 ± 509	293163 ± 171
2	953558 ± 309	102973 ± 101	2590418 ± 509	297469 ± 172
3	974013 ± 312	104552 ± 102	2402893 ± 490	281035 ± 168
4	992392 ± 315	108295 ± 104	2587490 ± 509	305743 ± 175
Two-fold coincidence				
1 & 2	21526 ± 47	1512 ± 12	70085 ± 84	856 ± 9
1 & 3	11552 ± 34	473 ± 7	62427 ± 79	749 ± 9
1 & 4	24124 ± 49	1730 ± 13	69350 ± 83	879 ± 9
2 & 3	20800 ± 46	1445 ± 12	64557 ± 80	901 ± 9
2 & 4	10938 ± 33	425 ± 7	67932 ± 82	828 ± 9
3 & 4	22994 ± 48	1641 ± 13	62966 ± 79	921 ± 10
Three-fold coincidence				
1, 2 & 3	341 ± 6	10 ± 1	1250 ± 12	2 ± 0
1, 2 & 4	370 ± 6	13 ± 1	1170 ± 11	3 ± 0
1, 3 & 4	363 ± 6	12 ± 1	1218 ± 11	2 ± 0
2, 3 & 4	344 ± 6	12 ± 1	1270 ± 11	2 ± 0
Four-fold coincidence				
1, 2, 3 & 4	14 ± 1	1 ± 0	26 ± 2	0 ± 0

Table 4.1: Measurements of the cross-talk between neutron detectors. The numbering scheme for the detectors is described in the text.

Detector pair	0° (%)	Monitor (%)
$\mathcal{X}(1,2)$	0.678 ± 0.006	0.010 ± 0.002
$\mathcal{X}(1,3)$	0.183 ± 0.004	0.006 ± 0.002
$\mathcal{X}(1,4)$	0.759 ± 0.007	0.014 ± 0.002
$\mathcal{X}(2,3)$	0.654 ± 0.006	0.015 ± 0.002
$\mathcal{X}(2,4)$	0.161 ± 0.004	0.007 ± 0.002
$\mathcal{X}(3,4)$	0.727 ± 0.007	0.034 ± 0.002

Table 4.2: Measured cross-talk ratio between detector pairs. The numbering scheme is described in the text.

detectors a and b to the total count rate in the two detectors. This ratio is related to the cross-talk via

$$\eta(a,b) = \frac{\mathcal{X}(a,b)\left(N_0^a + N_0^b\right)}{(N^a + N^b)} + \frac{kI^2}{(N^a + N^b)} \tag{4.2}$$

where the second term denotes the accidental rate. (The accidental rate scales quadratically with beam current I with k denoting the proportionality constant.) We take $N^a \approx N_0^a$ and $N^a \propto I$ which are true at the one percent level, yielding

$$\eta(a,b) = \mathcal{X}(a,b) + k'I. \tag{4.3}$$

Thus, by measuring the ratio $\eta(a,b)$ at two values of I, $\mathcal{X}(a,b)$ can be extracted:

$$\mathcal{X}(a,b) = \frac{1.25\,\eta_{0.125}(a,b) - 0.125\,\eta_{1.25}(a,b)}{1.25 - 0.125}. \tag{4.4}$$

Using the two-fold coincidence values given in Table 4.1, the cross-talk for each detector pair is summarized in Table 4.2.

The number of multiple counts between adjacent detectors is determined by multiplying the average number of counts in a detector pair by the cross-talk percentage between that pair. This procedure is performed for each pair of detectors and the remaining counts are then used in the analysis of the time-reversal data.

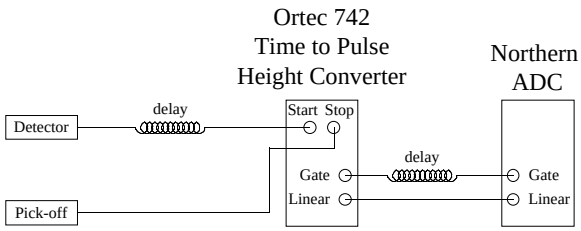

Figure 4.1: The electronics for the time-of-flight measurements.

4.2 Ratio of Neutrons to Gamma Rays

The use of plastic scintillators prohibits pulse shape discrimination between neutrons and gamma rays. Since the time-reversal violating interaction can only arise through neutron scattering events, the "background" of gamma ray counts must be removed before analysis of the data. These counts reduce the magnitude of the T-violating signal.

The ratio of neutrons to gamma rays is measured for the 0° detector array using time-of-flight techniques. A pulsed deuteron beam is incident upon the cryogenically cooled deuterium gas cell to produce neutrons. The deuteron beam pulses pass through a capacitive pick-off loop for timing purposes. The neutrons and gamma rays are transmitted through the holmium target and detected at 0°. The timing of the scintillation pulses is used along with the pick-off signal to determine the time-of-flight spectrum for the reaction.

The electronics for the time-of-flight measurements are shown in Figure 4.1. Measurements are performed individually for the four detectors. An Ortec 467 time to pulse height converter converts the timing difference between the pick-off and scintillation pulses into a voltage pulse. The voltage pulses are then digitized with an ADC and stored using the TUNL data acquisition system.

Two time-of-flight spectrum are taken for each of the four main detectors. A typical spectrum is shown in Figure 4.2. The vertical axis represents the number counts in each channel and the horizontal axis represents the channel number or time segment. The gamma rays reach the detectors first and appear as a small peak in the highest channel numbers.

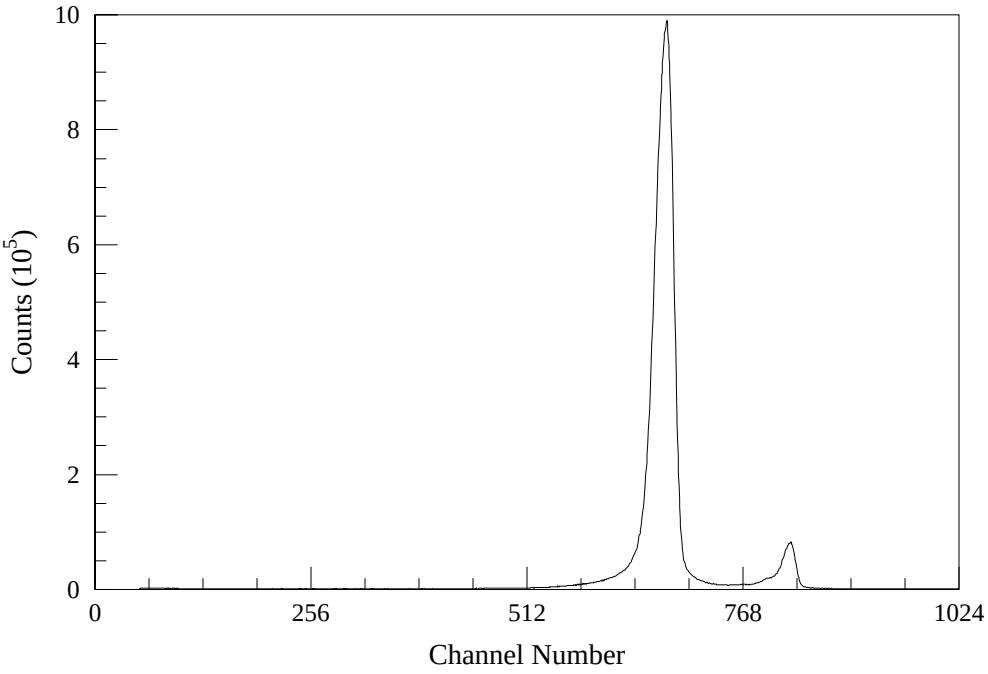

Figure 4.2: Typical time-of-flight spectrum for a 0° detector. The vertical axis depicts the number of counts and the horizontal axis depicts the channel number as described in the text. Time increases from right to left.

The large peak corresponds to the neutrons and occurs at a later time in the lower channels. Each channel corresponds to 0.17 ns.

The ratio of neutrons to gamma rays in an individual detector is determined by dividing the number of counts in the gamma ray peak by the number of counts in the neutron peak. Since the discriminators are set at the same energy, the ratios for all eight of the time-of-flight spectrum are then averaged to determine the normalization factor. These values are summarized in Table 4.3. The corrections are then applied to the asymmetry extracted in Chapter 5.

Measurements of the time-of-flight spectrum for the monitor detectors are not possible due to the short distance separating the detectors from the neutron production cell. The background of gamma rays is expected to be much smaller than observed in the 0° detectors due to the reduced thickness of the scintillation material. This ratio is estimated

Detector	N_γ/N_n (%)
1	6.57 ± 0.02
2	6.32 ± 0.02
3	6.43 ± 0.02
4	6.21 ± 0.02
Average	6.38 ± 0.01

Table 4.3: The ratio of neutrons to gamma rays in the 0° detectors.

to be less than 1% and no corrections are made in the analysis of the time-reversal data.

4.3 Deformation Effect

Measurements of the deformation effect cross section are performed to both verify the tensor alignment of the holmium target obtained from thermometry and confirm the direction of the alignment axis of the holmium crystal. These measurements are performed immediately before and after the time-reversal data are taken. Measurements of the deformation effect cross section at four additional energies were also performed during the initial testing stages of this experiment.

The deformation effect arises due to the non-spherical mass distribution of the holmium nucleus. When the nuclei in the holmium crystal are aligned, the cross section becomes dependent upon the direction of the alignment. The spatial orientation of the nuclei thus allow transmission cross section measurements to probe different axes of the nuclei as the crystal is rotated. The difference between the cross section for an aligned target and an unaligned target is referred to as the deformation effect.

The shape of the holmium nucleus is well known [Kos94, Mar70, Fas73, McC68, Fis67, Mar66, Wag65] and can be described with an angle-dependent radius given by

$$r(\theta) = r_0 A^{\frac{1}{3}} \left(1 + \sum_{K=2,4,6} \beta_K Y_K^0(\theta) \right), \tag{4.5}$$

where $r_0 = 1.26$ fm is the reduced radius, $A = 165$ is the atomic number, β_K is the deformation parameter, and $Y_K^0(\theta)$ is a spherical harmonic. Deformation parameters $\beta_2 = 0.30 \pm 0.025$, $\beta_4 = -0.02 \pm 0.05$, and $\beta_6 = 0.08 \pm 0.13$ have previously been determined for holmium [Kos94]. A deformation parameter of $\beta_2 = 0.3$ implies a highly deformed nucleus.

Deformation effect cross section measurements were performed by transmitting unpolarized neutrons through the aligned ^{165}Ho target. The 0° neutron yield is proportional (via Equation 2.22) to the total cross section, which for an unpolarized neutron beam, consists of the unpolarized and deformation effect partial cross sections:

$$\sigma_T = \sigma_{00} + \tilde{t}_{20}(I)\,\sigma_{02}. \tag{4.6}$$

The deformation effect term exhibits a $\mathrm{P}_2(\cos\theta)$ angular signature (Equation 2.11) and by varying the alignment angle with respect to the beam direction, this angular signature can be used to extract the product $\tilde{t}_{20}(I)\,\sigma_{02}$ from the total cross section through measurements of the neutron yield. Comparison with previous deformation effect measurements provides an independent verification of the magnitude of the tensor alignment $\tilde{t}_{20}(\mathrm{I})$ of the holmium target. The phase of the angular variation of the cross section also determines the direction of the alignment axis of the crystal.

At each of the four energies at which σ_{02} was measured, four to six hours of data were taken with the angle θ between the target alignment axis and neutron momentum varied every four minutes in the angular sequence $-180°$, …, $-22.5°$, $0°$, $+22.5°$, …, $+180°$, …, $-180°$, …. The neutron yield as a function of run number — or angular sequence — was then used to extract the deformation effect term in the total cross section. Data from a measurement of the neutron yield for 9.4 MeV neutrons is shown in Figure 4.3. The oscillation is due to the deformation effect and is superimposed on a large constant background arising from the unpolarized cross section. The slow linear drift is due to gain drifts in the photomultiplier tubes.

The logarithm of the normalized neutron yield as a function of angle — $\ln\left(\frac{N(\theta)}{N_0}\right)$ — is fit to the form $\mathcal{C} + \mathcal{A}\,\mathrm{P}_2(\cos\theta)$ in order to extract the magnitude of the deformation effect

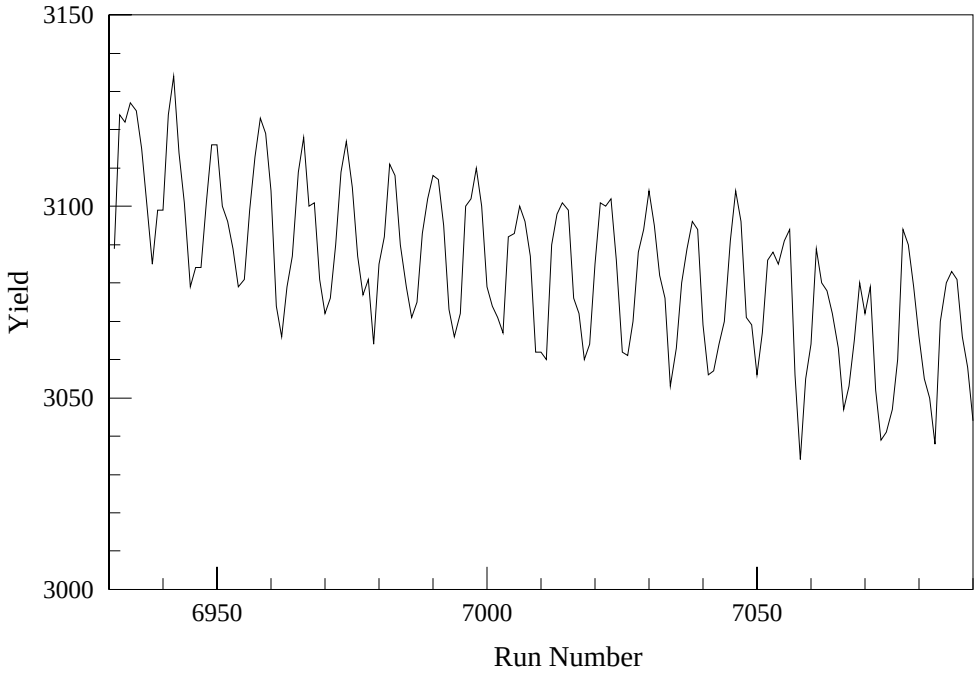

Figure 4.3: The transmission yield for 9.4 MeV neutrons. Each run number corresponds to four minutes of data taken in the angular sequence $-180^\circ \rightarrow +180^\circ \rightarrow -180^\circ$ in 22.5° steps. The oscillation arises from the deformation effect.

term. As with the five-fold correlation term discussed in Chapter 2, the angular dependence is removed

$$\sigma_2 = \frac{\sigma_{02}}{\mathrm{P}_2(\cos\theta)}, \tag{4.7}$$

yielding a quantity which can be directly compared to previous measurements. The angular coefficient $\mathcal{A}$ from the fit is related to the deformation effect cross section via

$$\sigma_2 = \frac{\mathcal{A}}{n\,\tilde{t}_{20}(I)}, \tag{4.8}$$

where $n = 0.065$ at/b is the target thickness and $\tilde{t}_{20}(I)$ is the tensor alignment of the holmium target. The fits are performed using a general least squares routine contained in the Numerical Recipes subroutine SVDFIT[2] [Pre92].

[2]See Chapter 5 for a description of this routine.

Energy (MeV)	$\tilde{t}_{20}(I)$	σ_2 (mb)
1.93	-0.59	-246 ± 41
5.86	-0.62	5 ± 3
6.57	-0.59	-3 ± 8
8.41	-0.59	-174 ± 23
9.37	-0.62	-237 ± 7
10.5	-0.59	-338 ± 44

Table 4.4: Measured values of the deformation effect cross section and the tensor alignment of the target during these measurements.

Measurements of the deformation effect cross section are presented in Table 4.4. The 1.93 MeV measurement was made using the ^{3}H(p, n)^{3}He neutron production reaction. A detailed discussion of this reaction and the tritium production target is given by Wilburn [Wil93]. The remaining measurements were performed using the ^{2}H(d, n)^{3}He reaction discussed in Section 3.3.1. Measurements at 5.86 and 9.37 MeV were performed during the FC experiment and the remaining measurements were performed at an earlier date.

The new deformation effect cross section values are shown in Figure 4.4 in addition to the previously measured values. The six new values are consistent with the previous measurements, thus confirming the target alignment obtained from thermometry. The errors in the deformation effect measurements are dominated purely by non-statistical fluctuations arising from gain drifts in the photomultiplier tubes.

A Fourier transform of the yield can also used to extract the deformation effect term. Using the fast Fourier transform technique provided in the SPEAKEASY computer software package [SPE93], the $P_2(\cos\theta)$ angular signature can be isolated. Since the $P_2(\cos\theta)$ oscillation will have a period of π radians, the power spectrum of the Fourier transform will have a sharp peak at this point. As can be seen from Figure 4.5, the angular signature of the $P_2(\cos\theta)$ is evident. Note that frequency components greater than 4π are aliased into lower frequencies due to the discrete angular rotation sequence (Nyquist's theorem [Tho84]).

The phase of the oscillation in Figure 4.3 is fixed by the location of the crystal align-

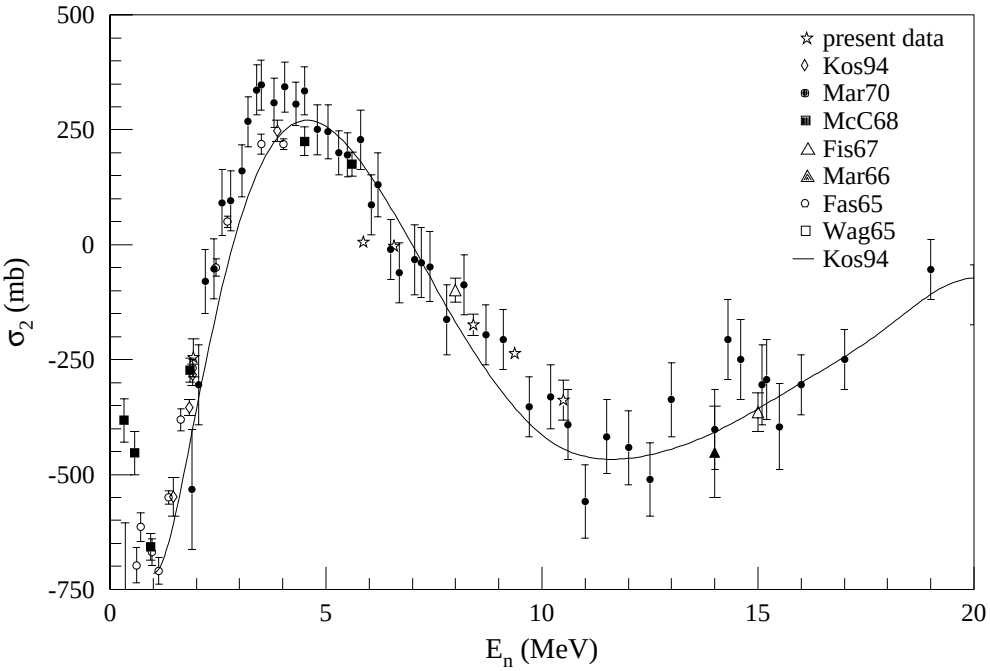

Figure 4.4: The deformation effect cross section as a function of energy. The solid curve corresponds to an optical model fit given by Koster [Kos94].

ment axis. The alignment axis was previously located using x-ray diffraction techniques [Kos90] and the deformation effect measurements are used as independent verification. Using the Macintosh computer package JMP [JMP94], the phase was extracted by performing a non-linear fit to the function $\mathcal{C}+\mathcal{A}\,\mathrm{P}_2(\cos(\theta+\phi))$. A value of $\phi = 1.9^\circ \pm 2.2^\circ$ was extracted for the phase of the oscillation. This phase is consistent with zero and taken to be zero in subsequent analyses.

For the time-reversal measurement, the deformation effect cross section was measured immediately before and after the time reversal data were taken. These measurements were performed at 9.4 MeV where the deformation effect is large. In order to reduce systematic effects that might arise from the deformation effect term, the time reversal measurement is performed at 5.9 MeV where the deformation effect cross section is small. These effects and others are discussed further in the next section.

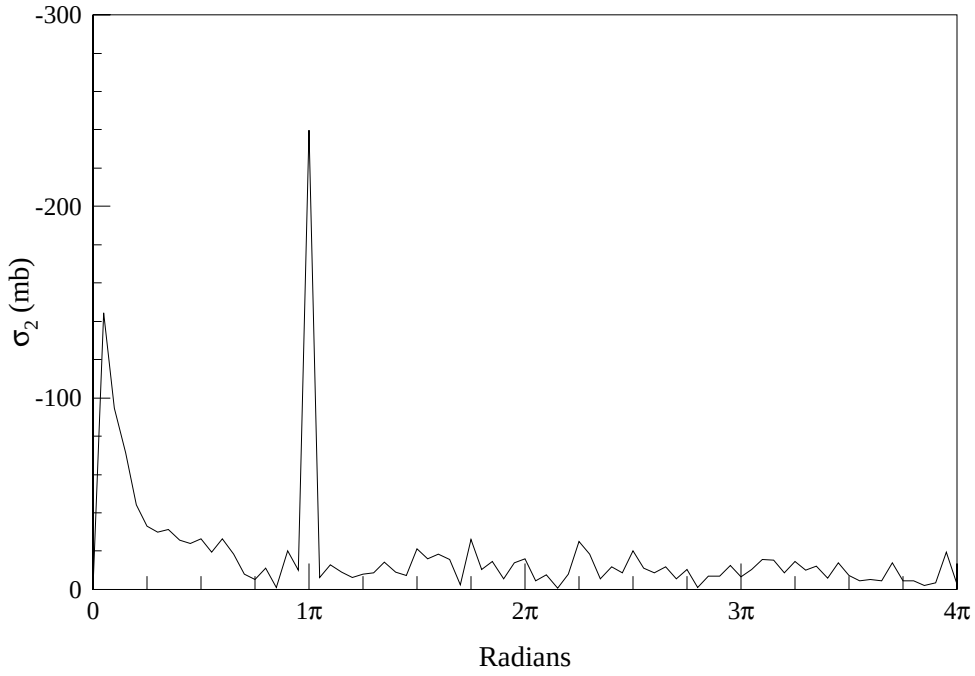

Figure 4.5: The Fourier transform of the 9.4 MeV neutron yield given in Figure 4.3. The vertical axis is normalized to give the magnitude of the deformation effect cross section.

4.4 Systematic Effects

Possible time-reversal conserving interactions that could mimic the $\sin 2\theta$ angular signature of the five-fold correlation term, independent of systematic considerations, have been discussed previously in Section 2.2.4. Systematic effects that could lead to a false asymmetry such as detector and target misalignments and finite size effects, for example, must be considered. Although most of these effects can not generate the $\sin 2\theta$ angular signature of the FC, upper bounds on the magnitude of these interactions must be estimated before excluding them in the analysis of the time-reversal data.

To begin, it is useful to identify effects that are known to be present and the level at which they become observable. The deformation effect is discussed in the previous section. It is measured to be $\sim 10^{-3}$ times the total cross section, and has a $\cos 2\theta$ angular dependence independent of the neutron spin. A term arises from the unequal tensor polar-

izations of the two spin-states of the deuteron beam. The difference in these polarizations contributes a constant offset in the asymmetry. It is measured to be equal to or less than 5×10^{-4}. Two reactions that possess analyzing powers are present: the $^2\mathrm{H}(\vec{\mathrm{d}}, \vec{\mathrm{n}})^3\mathrm{He}$ neutron production reaction and $^{165}\mathrm{Ho}(\vec{\mathrm{n}}, \vec{\mathrm{n}})$ elastic scattering. The magnitude of the analyzing power in the neutron production reaction is $\sim 10^{-2}$, while the small angle ($< 2^\circ$) Mott-Schwinger analyzing power in $\mathrm{n} + ^{165}\mathrm{Ho}$ elastic scattering is ~ 1. Lastly, the neutron spin is vertical to within 5° and the position of the alignment axis of the holmium crystal is known to within $\lesssim 4.1^\circ$.

The following subsections examine possible systematic effects in detail and set limits on mechanisms that could contribute to the normalized asymmetry.

4.4.1 Misalignments

Only one term in the cross section can directly contribute to a $\sin 2\theta$ angular dependence (Section 2.2.1). This is the partial cross section $\sigma_{12}(\Lambda = 2)$ which depends on $(\hat{\boldsymbol{s}} \cdot \hat{\boldsymbol{I}})(\hat{\boldsymbol{I}} \cdot \hat{\boldsymbol{k}})$. The angular dependence arises when the neutron spin has a component in the horizontal direction, directed along the x-axis, perpendicular to the momentum of the beam. The $(\hat{\boldsymbol{s}} \cdot \hat{\boldsymbol{I}})$ term will have a $\sin\theta$ dependence, and when combined with the $\cos\theta$ dependence of the $(\hat{\boldsymbol{I}} \cdot \hat{\boldsymbol{k}})$ term, can generate the $\sin 2\theta$ dependence of the FC term. This direct contribution term is expected to be negligible because the term is parity violating ($\sim 10^{-6}$) and must also couple with the deformation effect ($\sim 10^{-3}$) to be present. However, we have attempted to set a bound on this term experimentally.

The measurement was performed by placing the neutron spin in the horizontal x-z plane, perpendicular to the neutron momentum. This maximizes any effect. Data were taken using the angular sequence used in both the deformation effect and time-reversal measurements. The direction of the neutron spin was reversed every 100 ms in the eight-step sequence $+\ -\ -\ +\ -\ +\ +\ -$ and 256 eight-step sequences were accumulated at each angle. One complete angular sequence was taken, consisting of 32 runs. The beam polarization was 67% and the target alignment was 90%. (The same magnitude as in the FC

measurement, thus allowing a direct comparison between the measured asymmetries). The neutron yield was corrected for both dead-time and cross-talk using the same procedures discussed in Chapter 5. An asymmetry was formed between neutron spin states and fit to the form $\mathcal{C} + \mathcal{D}\sin 2\theta$. The coefficient $\mathcal{D}$ was measured to be $(-1.0 \pm 1.2) \times 10^{-5}$, consistent with zero.

In the time-reversal measurement the neutron spin is directed along the vertical y-axis or perpendicular to the horizontal x-z plane, so the $(\hat{\boldsymbol{s}} \cdot \hat{\boldsymbol{I}})(\hat{\boldsymbol{I}} \cdot \hat{\boldsymbol{k}})$ interaction term is suppressed by at least one order of magnitude. Also, a further factor of two suppression is expected because only the horizontal component of the neutron spin that is perpendicular to the neutron momentum can contribute to the $\sin 2\theta$ signature. Experimentally, the $(\hat{\boldsymbol{s}} \cdot \hat{\boldsymbol{I}})(\hat{\boldsymbol{I}} \cdot \hat{\boldsymbol{k}})$ interaction term is therefore $\lesssim 5 \times 10^{-7}$, below the limits of the actual time reversal measurement[3].

False asymmetries arising from misalignments of the target can occur in a number of ways. First consider a misalignment of the c-axis of the crystal. This can not be large, because the deformation effect measurements confirm that this direction is known to within $1.9^\circ \pm 2.2^\circ$ (Section 4.3). But a c-axis misalignment can present a problem if the $\cos 2\theta$ term is non-zero. The misalignment mixes the amplitudes of the $\sin 2\theta$ and $\cos 2\theta$ terms in the asymmetry; $A(\sin\phi \, \sin 2\theta + \cos\phi \, \cos 2\theta)$, where ϕ is the misalignment angle of the c-axis, measured to be less than 4.1°. The $\cos 2\theta$ component in the asymmetry is non-zero[4] and $\lesssim 1 \times 10^{-5}$. The contribution to the $\sin 2\theta$ component is at most 7×10^{-7}, below the limits of the present measurement.

A second c-axis misalignment issue is the reproducibly of the angle between the different rotation directions. The angular position of the target is measured with a shaft encoder located at the top of the cryostat. The torque on the thin shaft extending to the sample holder can change the actual angle of the target. The reproducibility of the angle of the target was measured using a laser directed onto a plane mirror attached to the

[3]The results of the time-reversal measurement are presented in Chapter 5 and the $\sin 2\theta$ component of the asymmetry is measured to be $(1.1 \pm 1.0) \times 10^{-6}$.

[4]The $\cos 2\theta$ component in the normalized asymmetry is $(8.5 \pm 1.5) \times 10^{-6}$. This term is attributed to a combination of the deformation effect and an analyzing power reaction coupled with a detector misalignment.

target. The reflected beam was directed onto a wall several meters away, allowing a precise measurement of the relative angular position. Deviations between rotation directions were measured to be less than $\pm 1^\circ$ (Chapter 3), and therefore are smaller than the 7×10^{-7} limits set by the angular phase of the deformation effect cross section.

A misalignment of the rotation axis of the target can also produce a reduced target thickness due the beam passing only through one side of the target. The target was aligned optically and is centered to within 0.25 mm at room temperature. At operating temperatures below 1 K, a horizontal position displacement due to thermal contraction is not expected due to the symmetric design of the mounting apparatus. A 1 mm displacement would reduce the target thickness by 5×10^{-3}. To simulate a time-reversal violating signature, this effect must couple with both an angle dependent interaction such as the deformation effect (which is $\sim 10^{-3}$) and an analyzing power effect (which is $\sim 10^{-2}$) in order to produce a spin-dependent angular signature. These effects are thus $\lesssim 5 \times 10^{-8}$.

Variations in the target thickness can give rise to angle dependent effects. For example, if the cross sectional area of the target is oval in shape, this could, when coupled with a holmium analyzing power effect, lead to a angular dependence in the asymmetry. The thickness of the target is circular to within 0.1 mm, leading to a maximum transmission asymmetry $\sim 10^{-4}$. The n $+^{165}$ Ho analyzing power reaction further reduces this effect by $\sim 10^{-2}$. The effect is thus $\lesssim 10^{-6}$. In fact, it is only a problem if both the 0° detector is misaligned and the angular signature arising from the variation in target thickness has a $\sin 2\theta$ angular dependence, neither of which is evident in the data.

A left-right movement of the target during the rotation sequence can also produce an angle dependent variation in target thickness. As above, this variation must couple with a n $+^{165}$ Ho analyzing power effect ($\sim 10^{-2}$) to contribute to the asymmetry. Left-right movement of the target was measured to be less than 0.5 mm at room temperature, yielding maximum variations in the target thickness of $\sim 10^{-4}$, therefore setting similar bounds $\lesssim 10^{-6}$ on a contribution from this term.

A misalignment of either the zero degree or monitor detector leads to a constant

offset in the asymmetry due to the analyzing power of the ^{2}H$(\vec{\mathrm{d}},\vec{\mathrm{n}})^3$He reaction. Alignment of the detectors was performed using an optical transit and the detectors are centered to within 2 mm, yielding a maximum misalignment angle of 0.2°. The false asymmetry arising from such a misalignment is derived by Koster [Kos90] and is given by

$$\mathcal{E} = \frac{m\,\delta\,(P_n^+ - P_n^-)}{2 + m\,\delta\,(P_n^+ + P_n^-)} \tag{4.9}$$

where $P_n^{\pm}$ is the neutron polarization, δ is the misalignment angle of the detector, and m is the linear component of the analyzing power ($A_y(\theta) = m\theta$). The average value of P_n for this experiment was 67% and the maximum difference between $P_n^{\pm}$ was less than 10%. Using the analyzing power for the ^{2}H$(\vec{\mathrm{d}},\vec{\mathrm{n}})^3$He reaction ($A_y(20°) = -.02$ with $m = -.06$ [Gus83]), neutron polarizations of $P_n^+ \sim 74\%$ and $P_n^- \sim 60\%$, and a misalignment angle of $\delta = 0.2°$, the constant asymmetry arising from a misalignment of the 0° detector is thus $\lesssim 10^{-5}$. This term is considerably smaller than the term arising from the difference in tensor polarizations ($\sim 5\times10^{-4}$) and can only contribute when combined with an angular dependent interaction such as the deformation effect ($\sim 10^{-3}$). These effects are thus $\lesssim 10^{-8}$ and are therefore negligible.

Large analyzing powers from small angle neutron scattering within the holmium sample are possible via Mott-Schwinger scattering. These effects have been measured for neutron scattering in lead [Hus77], having values as large as $A_y(1°) \simeq 1.0$. These effects are symmetric about 0° and the large size of the detectors will average out contributions from these effects. The outer edges of the 0° detector are at ±5° with respect to the holmium target and the analyzing power at this angle is $\simeq$ 0.2. An effect from this term would arise from a misalignment of the 0° detector, causing the average analyzing power on the two sides of the detector to be unequal. For a 0.2° misalignment of the 0° detector array, a contribution to the asymmetry is $\sim 10^{-2}$. In fact, a $\cos 2\theta$ variation in the asymmetry arising from the deformation effect ($\sim 10^{-3}$) coupled with an anayzing power reaction is present at the $\sim 10^{-5}$ level, consistent with this estimation. To contribute to the FC term of interest however, the angle dependent interaction must exhibit a $\sin 2\theta$ angular

signature. No T-conserving interactions are known to exhibit this angular signature and thus a combination of two interactions must combine to produce a $\sin 2\theta$ component in the asymmetry. Contributions to the FC term in the asymmetry from small angle Mott-Schwinger scattering are therefore negligible.

4.4.2 Beam and Detector Related Effects

False asymmetries can arise from intensity and polarization changes in the deuteron beam, which lead to similar changes in the neutron beam. Large density and temperature changes in the neutron production target can produce similar effects. These fluctuations are ideally removed by the combination of normalization to the monitor detector array and the fast spin-flip sequence.

The neutron production target can produce variations in the neutron flux due to density changes within the gas cell. When the deuteron beam is stopped in the gas cell, it deposits up to 6 W of heat into the cell. This heat is removed by the liquid nitrogen bath and the system takes about one hour to reach thermal equilibrium. The density changes are time dependent and will produce an exponential decrease in the normalized yield. Temperature stabilization of the neutron production target is therefore required to remove effects from these terms. Prior to the time-reversal measurement, variations in the neutron flux due to beam heating were observed and a discussion of the effects are presented in Appendix D. Variations in the yield when normalized to the beam current are $\sim 10-20\%$ and an asymmetry formed between these yields typically shows time dependent variations $\sim 10^{-3}$ for a 80 K temperature rise. The temperature of the gas cell was stabilized to with 0.5 K as discussed in Chapter 3, reducing these variations by two orders of magnitude. Normalization to the monitor further reduces these effects by an order of magnitude. These effects are discussed further in Appendix D and contributions from this effect are $\lesssim 3\times10^{-7}$ and do not contribute to the asymmetry.

Effects arising from terms independent of the neutron polarization such as gain drifts in the photomultiplier tubes are removed by the eight-step spin sequence and target

rotation. A detailed discussion of these terms is presented in Appendix E. Effects from polarization independent terms are shown to be less than $\sim 10^{-9}$.

4.4.3 Miscellaneous Effects

The neutrons produced in the giant dipole resonance (γ,n) reactions can contribute to the asymmetry. Cross sections for these reactions are $\sim$ 20 mb [Kel69], two orders of magnitude smaller than the neutron cross section. Further, the ratio of neutrons to gamma rays is measured to be 6.4%. The gamma rays resulting from the stopped deuteron beam have energy of $\sim$ 7 MeV and higher energy gamma rays produced directly by the deuteron beam are not expected. The ratio of gamma rays alone suppresses contributions from (γ,n) reactions by an order of magnitude and the small number of higher energy gamma rays in the giant resonance region (10-20 MeV) further suppresses this effect. An angle dependent term such as the deformation effect ($\sim 10^{-3}$) must couple with a spin-dependent analyzing power effect $\sim 10^{-1}$ to produce an angular signature. Effects from (γ,n) reactions are thus $\lesssim 10^{-7}$ even if all of the gamma rays have energies in the giant dipole resonance region.

A rotation of the neutron spin due the magnetic fields within the target can lead to a horizontal component of the neutron spin in the x-z plane. This horizontal component can then interact through the $(\hat{\boldsymbol{s}} \cdot \hat{\boldsymbol{I}})(\hat{\boldsymbol{I}} \cdot \hat{\boldsymbol{k}})$ term to produce a $\sin 2\theta$ angular dependence. As a worst case, assume all of the domains in the sample are in the same direction and each has a maximum internal field of 3 T. The neutron will interact with this field over the length of the sample ($\sim$ 2.5 cm), producing a maximum rotation of 0.04°. Thus neutron spin rotations due to the magnetic fields in the target are negligible.

In conclusion, T-conserving false asymmetries are measured to be smaller than those of the FC term of interest, allowing this measurement of the neutron transmission asymmetry to test time-reversal invariance directly.

Chapter 5

Data Analysis

Data were taken in two angular rotation sequences for the time-reversal measurement. The first data set was taken in the angular rotation sequence $-180^\circ \rightarrow +180^\circ \rightarrow -180^\circ$ in 22.5° steps. At each angle, 256 eight-step neutron spin sequences were accumulated using the sequence $+\ -\ -\ +\ -\ +\ +\ -$. The second data set was taken using the same neutron spin sequence but with an angular sequence of $-135^\circ \rightarrow +135^\circ \rightarrow -135^\circ$ in 90° steps. At each angle, 1024 eight-step sequences were accumulated. This angle sequence maximizes sensitivity to the $\sin 2\theta$ component of interest, but information on higher order components are lost. The two data sets are analyzed as separate measurements and combined in the final step of the analysis.

During collection of the data, counts from each neutron detector are routed and stored according to both the neutron spin-state and eight-step sequence number. Sequences which fail to meet rejection criteria (specified later) are removed and the remaining data are corrected for both dead-time and detector cross-talk. The neutron yield for each spin-state is normalized to the counts in the monitor detector array and an asymmetry for each eight-step sequence is formed between the two neutron spin-states. The 4096 asymmetries for a complete angular rotation sequence in a single rotation direction are then fit to a trigonometric series to extract the angular components in the asymmetry. These components are averaged for each rotation sequence and the amplitude of the T-violating term in the asym-

metry is extracted. This chapter describes the rejection scheme used in the data analysis, the corrections for dead-time and cross-talk, the statistical analysis, the curve fitting of the data, and concludes with the extraction of the T-violating spin-correlation coefficient.

5.1 Data Rejection and Dead-Time Corrections

Precise measurements of an analyzing power require that equal amounts of time are spent in the two neutron spin-states. Eight-step sequences with unequal times, whether caused by electronic inhibits or beam current fluctuations, are eliminated as a first step in the analysis.

The first criteria used for rejection of the data insures that the beam current remains consistent throughout the eight-step sequence. The beam current is collected and integrated using the electronics discussed in Chapter 3 and an inhibit window is placed around the average value of the beam current. Deviations in the beam current of more than $\sim 30\%$ of the average raise the inhibit of the CAMAC crate, thereby inhibiting data collection. Eight-step sequences in which these events occur are removed in the analysis using a pulser rejection system.

During data collection, counts from a 50 MHz pulser are routed and stored in the same manner as counts from the neutron detectors. Since the number of pulser counts in each spin-state remains constant with time, sequences in which this number deviates by more than 100 counts from the average are removed[1]. A typical time spectrum of the pulser counts for a 256 spin-state sequence is shown in Figure 5.1. Each channel corresponds to an eight-step sequence or 0.4 s of data and the dips in the spectrum occur when the CAMAC crate is inhibited by the beam current window.

The second rejection criteria utilizes a software window placed around the average value of the beam current. The average value is calculated for each 256 sequence run and sequences where the number of beam current pulses differ by more than $\pm 20\%$ of the mean

[1]The maximum asymmetry in an individual eight-step sequence arising from unequal times is thus $\lesssim 5 \times 10^{-6}$.

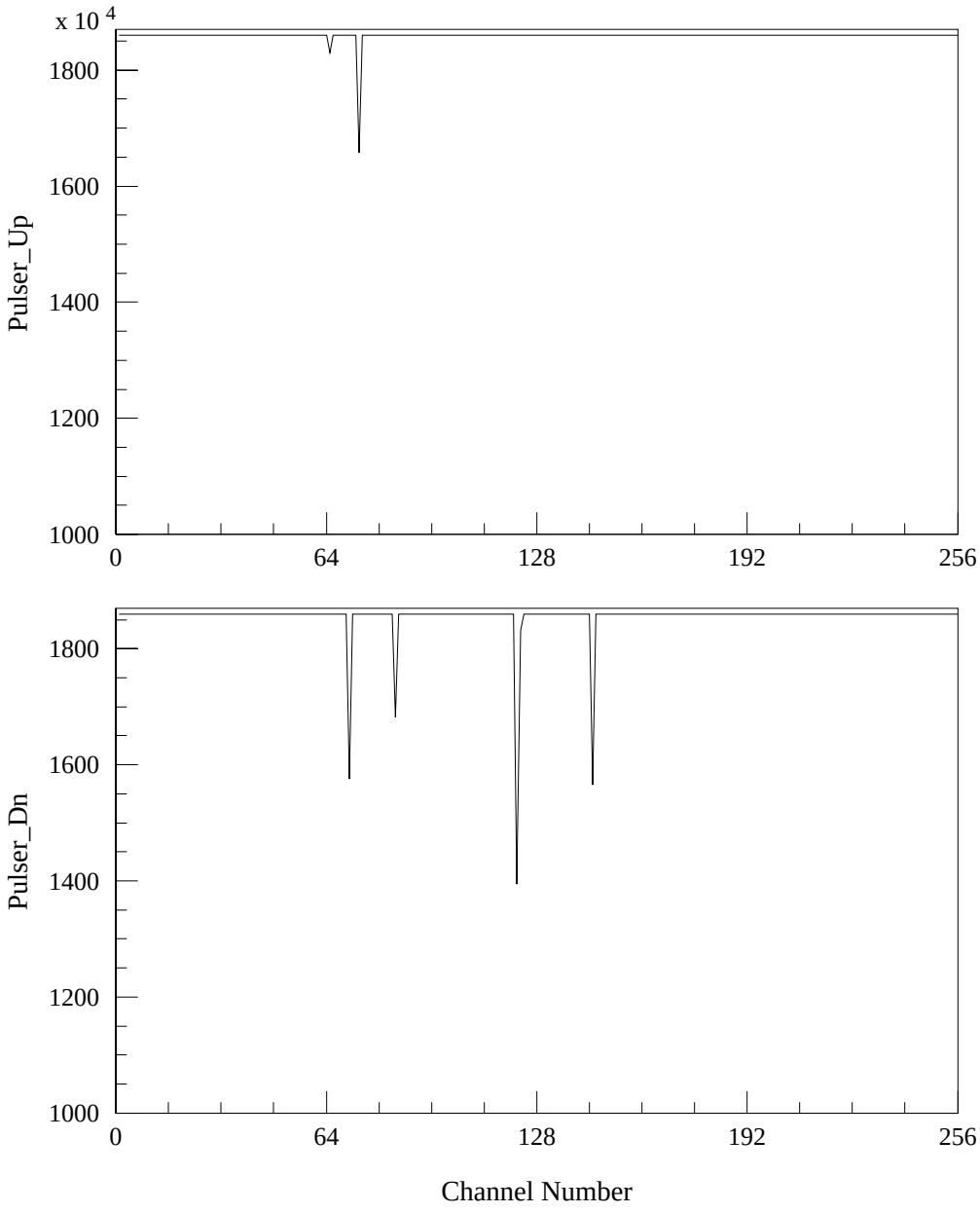

Figure 5.1: A sample pulser spectrum for one 256 spin-sequence run. The dips correspond to sequences in which the CAMAC crate was inhibited. Data is rejected if either of the two spectra contain deviations of more than 100 counts from the average.

are removed. This insures a consistent beam current during both an individual eight-step sequence and the entire 256 sequence run.

An asymmetry is then calculated for the beam current counts in the two spin-states and averaged over the entire run. Sequences in which this asymmetry exhibits a five or more standard deviation fluctuation from the average are removed. Ideally, the monitor normalization would remove effects arising from unequal beam currents, but as discussed in Appendix D, this normalization only suppresses these effects by an order of magnitude.

The final rejection criteria uses the monitor detector array. An asymmetry is formed between the counts in the two neutron spin states for each of the individual monitor detectors and an average value and standard deviation is determined for the entire run. Sequences where the asymmetry in two or more monitor detectors exhibit a more than four standard deviation fluctuation from the mean are removed.

This set of rejection criteria removes a total of 1.4% of the accumulated data. The first subset of data consists of 1568 runs of 256 sequences per run. A total of 5243 spin-sequences are removed, comprising 1.3% of the total number of eight-step sequences. The second subset contains 264 runs of 1024 sequences per run. A total of 4607 or 1.7% of these sequences are removed. The pulser rejection scheme accounts for 35% of the data removed with the remaining contributed to the beam current and asymmetry rejection criteria.

The next procedure in the analysis of the data is corrections to the yields for both the dead-time in the detectors and the cross-talk between adjacent detectors. Dead-time in the data acquisition electronics can arise from each of the three components within the system: the CAMAC scaler, the discriminator, and the time width of the voltage pulse from the detectors. The scaler operates at 225 MHz and the discriminator at 300 MHz. The contributions from either of these two components are negligible compared to the 10 ns width of the voltage pulse. The dead-time is dominated by the length of this pulse, yielding for example, a 10% dead-time at a count rate of 10 MHz. The dead-time correction factor $\delta_i^{\pm}$ can thus be calculated (assuming it arises completely from the width of the voltage

pulse) for an individual detector i using

$$\delta_i^{\pm} = 1 + \frac{N_i^{\pm}}{3.72 \times 10^7}, \tag{5.1}$$

where $N_i^{\pm}$ is the count rate in an individual 0° or monitor detector and 3.72×10^7 is the maximum number of counts for a 100 MHz pulser in a given spin-state[2]. The dead-time corrections are applied individually to the detectors ($\tilde{N}_i'^{\pm} = \delta_i^{\pm} N_i^{\pm}$). Typical corrections were $\sim .5$ % for the 0° detectors and ~ 1 % for the monitor detectors.

Once dead-time corrections are made, corrections for the cross-talk between detector pairs can be performed for both the 0° and monitor detectors. Using the measured cross-talk values presented in Table 4.1, the cross-talk corrected yields $\tilde{N}_i^{\pm}$ for both the 0° and monitor detectors are given for example in detector (1) by

$$\begin{aligned} \tilde{N}_1^{\pm} &= \tilde{N}_1'^{\pm} - \frac{\mathcal{X}(1,2)}{2}\left(\tilde{N}_2'^{\pm} + \tilde{N}_1'^{\pm}\right) \\ &\quad - \frac{\mathcal{X}(1,3)}{2}\left(\tilde{N}_3'^{\pm} + \tilde{N}_1'^{\pm}\right) - \frac{\mathcal{X}(1,4)}{2}\left(\tilde{N}_4'^{\pm} + \tilde{N}_1'^{\pm}\right). \end{aligned} \tag{5.2}$$

Similar expressions are used in correcting the yield for the other three detectors.

5.2 Statistical Analysis

The corrected yields are then used in forming a normalized asymmetry $\mathcal{E}_i$ for each of the four 0° detectors in each eight-step sequence. The four detector asymmetries are then combined to form an average asymmetry for the sequence. This section describes the procedures for forming these asymmetries and the associated errors in the measurements.

The normalized asymmetry for an individual 0° detector i is calculated using Equation 2.23 or

$$\mathcal{E}_i = \frac{\frac{\tilde{N}_i^+(0^\circ)}{\tilde{N}_i^-(0^\circ)} - \mathcal{M}}{\frac{\tilde{N}_i^+(0^\circ)}{\tilde{N}_i^-(0^\circ)} + \mathcal{M}}, \tag{5.3}$$

where $\tilde{N}_i^{\pm}(0^\circ)$ corresponds to the number of counts in a given 0° detector and $\mathcal{M}$ corresponds to the monitor normalization factor. Ideally, the monitor normalization factor $\mathcal{M}$

[2]The time spent in an individual spin-state for an eight-step sequence is 0.093 s/spin-state × 4 spin-states.

is calculated as the ratio of the total number of counts in the two spin-states of the four monitor detectors:

$$\mathcal{M} = \frac{\tilde{N}_1^+(M) + \tilde{N}_2^+(M) + \tilde{N}_3^+(M) + \tilde{N}_4^+(M)}{\tilde{N}_1^-(M) + \tilde{N}_2^-(M) + \tilde{N}_3^-(M) + \tilde{N}_4^-(M)} \tag{5.4}$$

However, this ratio does not remove effects arising from the drifts in efficiencies of the individual detectors and must therefore be formed in such a way to remove these effects.

The count rate in a given detector is proportional to both the incident neutron flux $I_i^{\pm}$ and the detector efficiency ϵ_i, ($\tilde{N}_i^{\pm} \propto I_i^{\pm}\,\epsilon_i$). By forming a ratio between the number of counts in the two spin-states for a given detector, the efficiency will cancel, thus leaving the ratio of the count rates in the detector equal to the ratio of the incident fluxes:

$$\frac{\tilde{N}_i^+}{\tilde{N}_i^-} = \frac{I_i^+\,\epsilon_i}{I_i^-\,\epsilon_i} = \frac{I_i^+}{I_i^-}. \tag{5.5}$$

The fluctuations in an asymmetry arising from detector efficiencies are thus completely removed using this technique.

The monitor normalization factor $\mathcal{M}$ can be calculated to good approximation using the ratio of the geometric means of the four monitor detectors:

$$\mathcal{M} = \sqrt[4]{\prod_{i=1}^{4} \frac{\tilde{N}_i^+(\mathrm{M})}{\tilde{N}_i^-(\mathrm{M})}}. \tag{5.6}$$

The geometric mean approximation is equal to the arithmetic mean for identical sample values and is slightly less than the arithmetic mean for numbers that are similar in size. For the present arrangement, the counts in the four monitor detectors are equal to within 10%, allowing this approximation to be sufficient. The normalization to the geometric mean greatly reduces the non-statistical fluctuations that could appear from detector efficiency changes and is therefore superior to the arithmetic mean.

The statistical error in $\mathcal{M}$ is determined using the errors from the number of counts in each individual detector. Assuming a binomial distribution where the error in an individual measurement of $\tilde{N}$ counts is given by $\Delta\tilde{N} = \sqrt{\tilde{N}}$, the error in $\mathcal{M}$ is given by

$$\Delta\mathcal{M} = \frac{\mathcal{M}}{4}\sqrt{\sum_{i=1}^{4}\left[\frac{\delta_i^+(\mathrm{M})}{\tilde{N}_i^+(\mathrm{M})} + \frac{\delta_i^-(\mathrm{M})}{\tilde{N}_i^-(\mathrm{M})}\right]} \tag{5.7}$$

using standard error propagation techniques [Bev69]. The factors $\delta_i^{\pm}(\mathrm{M})$ are the dead-time correction factors for the monitor detectors.

The average asymmetry of the detectors is formed by averaging the individual asymmetries of the four detectors:

$$\mathcal{E} = \frac{1}{4}\sum_{i=1}^{4}\mathcal{E}_i. \tag{5.8}$$

However, the error in $\mathcal{E}$ can not be calculated by combining the four individual errors, $\Delta\mathcal{E}_i$, since correlations exist due to the normalization to the single value of $\mathcal{M}$. The error in the asymmetry is thus given by

$$\Delta\mathcal{E} = \frac{\mathcal{M}}{2}\sqrt{\sum_{i=1}^{4}\frac{\left(\frac{\tilde{N}_i^+(0^\circ)}{\tilde{N}_i^-(0^\circ)}\right)^2\left[\frac{\delta_i^+(0^\circ)}{\tilde{N}_i^+(0^\circ)}+\frac{\delta_i^+(0^\circ)}{\tilde{N}_i^-(0^\circ)}\right]}{\left(\frac{\tilde{N}_i^+(0^\circ)}{\tilde{N}_i^-(0^\circ)}+\mathcal{M}\right)^4}+\left[\sum_{i=4}^{4}\frac{\left(\frac{\Delta\mathcal{M}}{\mathcal{M}}\frac{\tilde{N}_i^+(0^\circ)}{\tilde{N}_i^-(0^\circ)}\right)}{\left(\frac{\tilde{N}_i^+(0^\circ)}{\tilde{N}_i^-(0^\circ)}+\mathcal{M}\right)^2}\right]^2}. \tag{5.9}$$

The values of $\mathcal{E}$ and $\Delta\mathcal{E}$ for each spin state are then used in the extraction of the angular components. For display purposes, an average asymmetry for each run of 256 eight-step sequences is calculated and shown in Figure 5.2 for a 40 hour time segment of data. Each run corresponds to the average asymmetry for an angular position when taken in the 22.5° rotation sequence. A T-violating signal would appear as a $\sin 2\theta$ oscillation on top of the constant background, similar to the oscillations arising from the deformation effect shown in Figure 4.3. No oscillation is present and a fit to this data can be used to extract an upper bound on the T-violating FC term of interest.

5.3 Least Squares Fitting

The magnitude of the angular components in the asymmetry is extracted using a least squares fit to the form

$$\mathcal{E}(x) = a_0 + \sum_{k=1}^{7} a_k \sin\left(k\theta(x)\right) + \sum_{k=1}^{8} b_k \cos\left(k\theta(x)\right) \tag{5.10}$$

for the 22.5° rotation sequence and

$$\mathcal{E}(x) = a_0 + \sum_{k=1}^{2} a_k \sin\left(k\theta(x)\right) + b_1 \cos\left(\theta(x)\right) \tag{5.11}$$

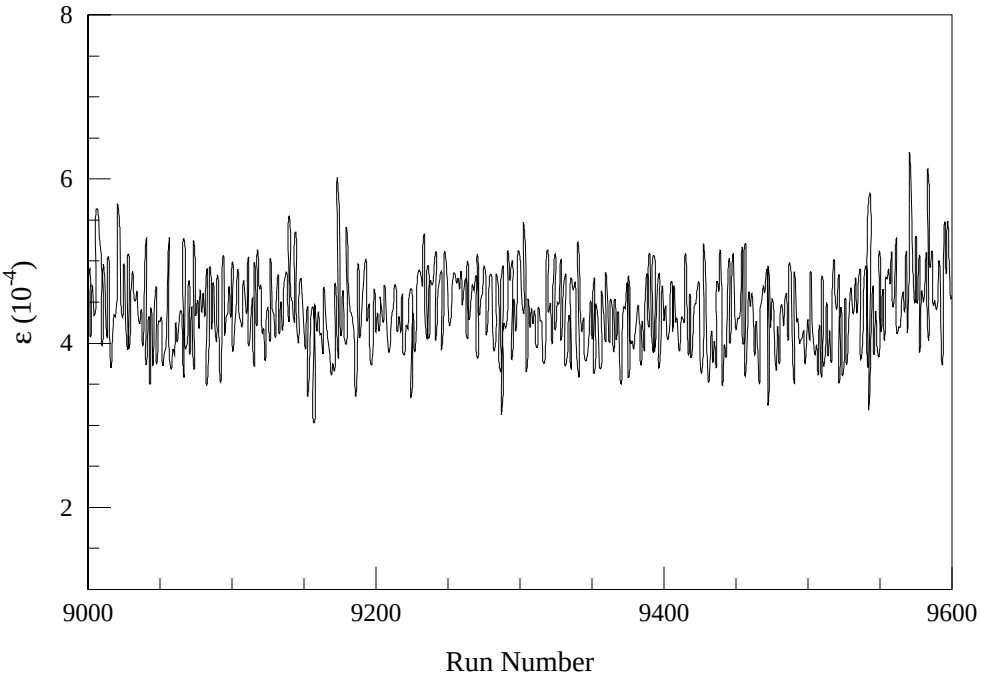

Figure 5.2: The normalized spin-flip asymmetry for 5.9 MeV neutrons. Each run corresponds to the average value of the asymmetry for the 256 spin-sequences taken in the 22.5° angular sequence.

for the 90° rotation sequence. Here, $\theta(x)$ for the 22.5° rotation sequence is related to x via

$$\theta(x) = \pi\left(\frac{x}{8} - 1\right) \tag{5.12}$$

and for the 90° rotation sequence via

$$\theta(x) = \pi\left(\frac{x}{2} - \frac{3}{4}\right). \tag{5.13}$$

The integer x is given by $x = 0, 1, \ldots, m-1$ for a clockwise rotation and $x = m-1, m-2, \ldots, 0$ for a counterclockwise rotation. The number of angles in the sequence determines m, where for the 22.5° rotation sequence $m = 16$ and for the 90° rotation sequence $m = 4$. The number of trigonometric terms included in Equations 5.10 and 5.11 are determined using the angle of rotation with Nyquist's theorem [Tho84]. Higher frequency components can exist, but will be aliased into the lower frequency terms.

For fitting purposes, the complete set of data is divided into subsets consisting of a complete angular rotation in one direction. For example, in the 22.5° rotation sequence, each subset would consist of 16 runs either starting at an angle of −180° or +180°. The amplitudes a_k and b_k given in Equation 5.10 or 5.11 are determined for each subset and the values of these coefficients are then averaged to extract the amplitudes for the entire set of data.

The general least squares fit is performed using the method of singular value decomposition (SVD) [Pre92]. In a standard least squares routine, the chi-square (χ^2) of the fitting function is minimized to extract the best fit to the data. For a function that has basis components that fit the data equally well (as is expected for all of the trigonometric terms in this function), the inversion matrix for the normal equations of the fit can develop singularities. The technique of SVD is the method of choice in such a fit because singularities are avoided, providing a proper least squares fit to the data.

The fits were performed using the Numerical Recipes subroutine SVDFIT [Pre92]. The angular position θ and the corresponding asymmetry $\mathcal{E} \pm \Delta\mathcal{E}$ for each eight-step sequence are used to extract the fitting coefficients a_k and b_k defined by Equation 5.10 or 5.11. The output of the subroutine SVDFIT contains both the fitting coefficients and the SVD of the data. The SVD array is then used with the subroutine SVDVAR to extract the statistical error in the fitting coefficients.

The total error or sample standard deviation (containing both the statistical and non-statistical contributions to the error) can be calculated using a weighted standard deviation [Bev69]

$$\sigma_k = \xi_k \sqrt{\frac{\displaystyle\sum_{j=1}^{N} \frac{1}{(N-M-1)} \frac{1}{(\Delta\mathcal{E})_j^2} \left(\mathcal{E}_j - \mathcal{E}_{fit}\right)^2}{\displaystyle\sum_{j=1}^{N} \frac{1}{N} \frac{1}{(\Delta\mathcal{E})_j^2}}}, \tag{5.14}$$

where ξ_k is the correlation coefficient, $\mathcal{E}_j$ is an individual eight-step asymmetry with error $\Delta\mathcal{E}_j$, $\mathcal{E}_{fit}$ is the asymmetry calculated using Equation 5.10 or 5.11 and the extracted values of the fitting coefficients a_k and b_k, N is the total number of eight-step sequences included in

the fit, and M is the number of trigonometric terms in the fit. The correlation coefficients ξ_k for the fitting coefficients are extracted using the same procedure described above in extracting the statistical error, but with the error for each eight-step asymmetry set to $\Delta\mathcal{E}_i = 1.0$. The errors returned from the SVDVAR routine thus contain only the correlations in the fitting parameters and can be included directly into the calculation of the standard deviation. Both the statistical error and standard deviation are calculated for the fitting coefficients.

The fitting procedure was first tested using randomly generated data sets consisting of Gaussian distributed noise on a constant background. Three sets were generated, one with random noise alone, one with a $2\sigma \sin 2\theta$ oscillation included in addition to the noise, and one with a $5\sigma \sin 2\theta$ oscillation included in the same manner. Each data set was then fit to Equation 5.10 above and values for both the coefficients a_k and b_k and their standard deviations were extracted. The results from these fits are summarized in Table 5.1.

The fitting coefficients extracted from the random noise data set show no evidence of any non-statistical effects. The data set containing the $2\sigma \sin 2\theta$ oscillation similarly shows no non-statistical effects. This is expected since five greater than 1σ effects are should arise due purely to statistical fluctuations. The $5\sigma \sin 2\theta$ term in the third set of data is clearly present and can be extracted using this fitting procedure. Thus this fitting procedure can extract small angular oscillations appearing on top of a large constant background.

In the fit to the time-reversal data, all fifteen of the angular fitting coefficients contained in Equation 5.10 are expected to be zero under ideal conditions. Since each is an independent variable, the values extracted should be gaussian distributed about zero. Therefore, one expects 68% of these coefficients to be less than 1σ from zero, 95% to be less than 2σ from zero, and 99.7% to be less than 3σ from zero. This implies that on average, 10 coefficients would lie between 0 and 1σ from zero, 4 coefficients would lie between 1σ and 2σ from zero, and one coefficient would lie between 2σ and 3σ from zero. Fits to numerous sets of random noise verify these distributions of the fitting coefficients.

The same fitting procedures applied to the sets of randomly generated noise are

Random Noise					
Fitting Coefficient		T-ratio	Fitting Coefficient		T-ratio
Constant	$-499.86 \pm .11 \times 10^{-5}$	475.1	$\cos\theta$	$-.07 \pm .15 \times 10^{-5}$	.5
$\sin\theta$	$-.20 \pm .15 \times 10^{-5}$	1.4	$\cos 2\theta$	$-.18 \pm .15 \times 10^{-5}$	1.2
$\sin 2\theta$	$.05 \pm .15 \times 10^{-5}$	.4	$\cos 3\theta$	$-.15 \pm .15 \times 10^{-5}$	1.0
$\sin 3\theta$	$-.14 \pm .15 \times 10^{-5}$	1.0	$\cos 4\theta$	$.03 \pm .15 \times 10^{-5}$	.2
$\sin 4\theta$	$.17 \pm .15 \times 10^{-5}$	1.1	$\cos 5\theta$	$.20 \pm .15 \times 10^{-5}$	1.4
$\sin 5\theta$	$-.09 \pm .15 \times 10^{-5}$	.6	$\cos 6\theta$	$.16 \pm .15 \times 10^{-5}$	1.1
$\sin 6\theta$	$-.20 \pm .15 \times 10^{-5}$	1.4	$\cos 7\theta$	$-.03 \pm .15 \times 10^{-5}$	.2
$\sin 7\theta$	$-.28 \pm .15 \times 10^{-5}$	1.9	$\cos 8\theta$	$.01 \pm .15 \times 10^{-5}$	.1
Random Noise + $2\sigma \sin 2\theta$					
Constant	$-500.35 \pm .11 \times 10^{-5}$	475.6	$\cos\theta$	$.03 \pm .15 \times 10^{-5}$	.2
$\sin\theta$	$-.15 \pm .15 \times 10^{-5}$	1.0	$\cos 2\theta$	$.21 \pm .15 \times 10^{-5}$	1.4
$\sin 2\theta$	$.20 \pm .15 \times 10^{-5}$	1.4	$\cos 3\theta$	$-.02 \pm .15 \times 10^{-5}$	.1
$\sin 3\theta$	$.08 \pm .15 \times 10^{-5}$	.5	$\cos 4\theta$	$.21 \pm .15 \times 10^{-5}$	1.4
$\sin 4\theta$	$.08 \pm .15 \times 10^{-5}$	.5	$\cos 5\theta$	$.06 \pm .15 \times 10^{-5}$	.4
$\sin 5\theta$	$-.02 \pm .15 \times 10^{-5}$	.1	$\cos 6\theta$	$-.04 \pm .15 \times 10^{-5}$	.3
$\sin 6\theta$	$.14 \pm .15 \times 10^{-5}$	.9	$\cos 7\theta$	$.20 \pm .15 \times 10^{-5}$	1.4
$\sin 7\theta$	$.11 \pm .15 \times 10^{-5}$	.8	$\cos 8\theta$	$.10 \pm .11 \times 10^{-5}$	.9
Random Noise + $5\sigma \sin 2\theta$					
Constant	$-498.67 \pm .11 \times 10^{-5}$	474.0	$\cos\theta$	$.07 \pm .15 \times 10^{-5}$	.5
$\sin\theta$	$.23 \pm .15 \times 10^{-5}$	1.5	$\cos 2\theta$	$-.31 \pm .15 \times 10^{-5}$	2.1
$\sin 2\theta$	$.85 \pm .15 \times 10^{-5}$	5.7	$\cos 3\theta$	$-.08 \pm .15 \times 10^{-5}$	.5
$\sin 3\theta$	$-.07 \pm .15 \times 10^{-5}$	.5	$\cos 4\theta$	$-.08 \pm .15 \times 10^{-5}$	.6
$\sin 4\theta$	$.10 \pm .15 \times 10^{-5}$	.7	$\cos 5\theta$	$.15 \pm .15 \times 10^{-5}$	1.0
$\sin 5\theta$	$-.16 \pm .15 \times 10^{-5}$	1.1	$\cos 6\theta$	$.05 \pm .15 \times 10^{-5}$	.4
$\sin 6\theta$	$-.03 \pm .15 \times 10^{-5}$	.2	$\cos 7\theta$	$.09 \pm .15 \times 10^{-5}$	.6
$\sin 7\theta$	$.24 \pm .15 \times 10^{-5}$	1.6	$\cos 8\theta$	$-.13 \pm .11 \times 10^{-5}$	1.2

Table 5.1: The effects of the addition of a $\sin 2\theta$ signal in a randomly generated set of data. The T-ratio is defined as the ratio of the extracted value of the fitting coefficient to its standard deviation.

applied to the asymmetries in the time-reversal measurement. A general least squares fit is performed on each subset of data consisting of a complete rotation in one direction. The fitting coefficients are then combined using a weighted average to obtain the coefficients for the entire data set. In the first data set, 98 subsets of data are fit individually and the fitting coefficients averaged using the statistical error in the fitting coefficients as the weighting factor. The second data set contains 66 subsets and are fit and averaged similarly. The average values of the fitting coefficients for the two sets of data are summarized in Table 5.2. The statistical error and standard deviation are in very good agreement and have been quoted to four significant figures to quantify this agreement. The data suggest that the cosine coefficients contain non-statistical fluctuations as would be expected from the discussion presented in Appendix E, whereas these non-statistical terms are removed in the sine coefficients. The values of the sine coefficients of the fit are consistent with gaussian statistics and no anomalies are observed.

Once the fitting procedure is performed on the time reversal data, the fitting coefficients and their associated statistical errors and standard deviations are averaged to determine the value of the $\sin 2\theta$ coefficient for the combined set of data. The two values are combined using a standard weighted average, yielding a coefficient of

$$a_2 = 1.1 \pm 1.0 \pm 1.0 \times 10^{-6} \tag{5.15}$$

for the $\sin 2\theta$ term. The first value corresponds to the central value of the measurement, the second value corresponds to the statistical error, and the third value corresponds to the total error or standard deviation. Since the two errors are equal within the limits of this measurement, only one error will be used in further discussions of this measurement.

The spin-correlation coefficient A_5 must next be calculated using the amplitude a_2 of the $\sin 2\theta$ oscillation. Experimental quantities such as the polarizations and target thickness are removed, leaving a quantity which can be directly compared with measurements in other systems. Measurements of the beam polarization and target alignment are discussed in the next section, followed by the calculation of the spin-correlation coefficient A_5.

22.5° Rotation Sequence		
Coefficient ± Stat. Error ± Std. Deviation		T-ratio
Constant	$-433.21 \pm .1053 \pm .1054 \times 10^{-5}$	411.5
$\sin\theta$	$-.42 \pm .1489 \pm .1491 \times 10^{-5}$	2.8
$\sin 2\theta$	$.18 \pm .1489 \pm .1491 \times 10^{-5}$	1.2
$\sin 3\theta$	$.12 \pm .1489 \pm .1491 \times 10^{-5}$	.8
$\sin 4\theta$	$-.02 \pm .1489 \pm .1491 \times 10^{-5}$	.2
$\sin 5\theta$	$-.06 \pm .1489 \pm .1491 \times 10^{-5}$	.4
$\sin 6\theta$	$-.13 \pm .1489 \pm .1491 \times 10^{-5}$	.9
$\sin 7\theta$	$-.05 \pm .1489 \pm .1491 \times 10^{-5}$	.3
$\cos\theta$	$-.47 \pm .1489 \pm .1491 \times 10^{-5}$	3.2
$\cos 2\theta$	$.86 \pm .1489 \pm .1491 \times 10^{-5}$	5.8
$\cos 3\theta$	$.00 \pm .1489 \pm .1491 \times 10^{-5}$	.0
$\cos 4\theta$	$-.17 \pm .1489 \pm .1491 \times 10^{-5}$	1.1
$\cos 5\theta$	$.28 \pm .1489 \pm .1491 \times 10^{-5}$	1.9
$\cos 6\theta$	$.18 \pm .1489 \pm .1491 \times 10^{-5}$	1.2
$\cos 7\theta$	$-.23 \pm .1489 \pm .1491 \times 10^{-5}$	1.5
$\cos 8\theta$	$.18 \pm .1053 \pm .1054 \times 10^{-5}$	2.6
90° Rotation Sequence		
Constant	$-567.93 \pm .1400 \pm .1398 \times 10^{-5}$	405.7
$\sin\theta$	$.10 \pm .1980 \pm .1977 \times 10^{-5}$	.5
$\sin 2\theta$	$.05 \pm .1400 \pm .1398 \times 10^{-5}$	.4
$\cos\theta$	$-.41 \pm .1980 \pm .1977 \times 10^{-5}$	2.1

Table 5.2: The fitting coefficients of the least squares fit to the two sets of time-reversal data. Note the close agreement between the statistical error and the standard deviation.

$K^{y}_{y'}(0°)$	0.58 ± 0.03
$A_{zz}(0°)$	-0.51 ± 0.01
$A_{y}(36°)$	$0.039 \pm .002$
$A_{yy}(36°)$	0.24 ± 0.01

Table 5.3: Known parameters of the ^{2}H$(\vec{\mathrm{d}},\vec{\mathrm{n}})^3$He reaction. Values at 0° are taken from [Lis75] and values at 36° are taken from [Gus83].

5.4 Beam and Target Polarizations

The beam polarization is measured using the left-right asymmetry of the ^{2}H$(\vec{\mathrm{d}},\vec{\mathrm{n}})^3$He reaction. The experimental setup for this measurement is discussed in Chapter 3 and the framework for extracting the neutron polarization is presented in Chapter 2. The average asymmetry for the two spin-states ($\mathcal{E}_{LR} = 0.5(\mathcal{E}^{+}_{LR} + \mathcal{E}^{-}_{LR})$) is formed in a manner to remove the unknown detector efficiency and is given by

$$\mathcal{E}_{LR} = \frac{\sqrt{\frac{N^{+}_{L}}{N^{-}_{L}}\frac{N^{-}_{R}}{N^{+}_{R}}} - 1}{\sqrt{\frac{N^{+}_{L}}{N^{-}_{L}}\frac{N^{-}_{R}}{N^{+}_{R}}} + 1}, \tag{5.16}$$

where L and R denote the left and right detectors and $\pm$ denote the neutron spin state. The counts in the two detectors are corrected for dead-time and spin-states failing the rejection criteria discussed above are removed. The asymmetry is then used along with the parameters from the polarization transfer reaction to extract the average neutron polarization.

The left-right asymmetry was measured to be 0.048 ± 0.00001 during the time-reversal measurement. When combining this value with the known parameters of the ^{2}H$(\vec{\mathrm{d}},\vec{\mathrm{n}})^3$He reaction summarized in Table 5.3, a neutron polarization of $P_n = 0.67 \pm 0.05$ is determined.

The target alignment is calculated using the temperature of the sample and the known temperature dependence of the alignment presented in Chapter 2. The temperature was controlled at 160 mK with fluctuations of about 2 mK. The error in the temperature arises from both these fluctuations and the calibration of the Dale thermometer. This

a_2	$1.1 \pm 1.0 \times 10^{-6}$
ϕ	0.0638 ± 0.0001
P_n	0.67 ± 0.05
$\tilde{t}_{20}$	0.62 ± 0.03
n	0.065
σ_0	5.14

Table 5.4: A summary of the experimental parameters in the time-reversal measurement. The target thickness n is calculated in Appendix B using Monte-Carlo techniques. The unpolarized cross section σ_0 is taken from the optical model predictions of [McL88].

thermometer was calibrated against a Lake Shore calibrated germanium thermometer. The error in the germanium calibration is 3% at this temperature, resulting in an error of 5% in the calibration of the Dale thermometer. The measured temperature of the sample was taken as $T = 160 \pm 8$ mK. Combining this value with the measured values of the energy eigenvalues of the magnetic dipole and electric quadrupole interactions presented in Chapter 2, a target alignment of $\tilde{t}_{20}^{planar} = 1.36 \pm .07$ is determined. This is approximately 90% of the maximum value.

5.5 Spin-Correlation Coefficient

The final step in the analysis procedure is the calculation of the spin-correlation coefficient A_5. This coefficient is related to the amplitude of the $\sin 2\theta$ coefficient a_2, the beam polarization and target alignment, the target thickness, the unpolarized cross section, and the background of gamma rays.

The spin-correlation coefficient is given by

$$A_5 = \frac{a_2(1+\phi)}{P_n \tilde{t}_{20} n \sigma_0}, \tag{5.17}$$

where ϕ represents the background of gamma rays. This background has the effect of artificially lowering the asymmetry and must be corrected for when calculating the spin-correlation coefficient. Using the experimental parameters summarized in Table 5.4, the

spin-correlation coefficient is determined to be

$$A_5 = 8.6 \pm 7.7 \times 10^{-6}. \tag{5.18}$$

This value is consistent with time reversal invariance and sets a bound at the 95% confidence level of

$$A_5 \leq 2.2 \times 10^{-5}. \tag{5.19}$$

Chapter 6

Results and Conclusions

In order to compare the results extracted in the previous chapter with time-reversal measurements in other systems, the spin-correlation coefficient A_5 must be converted into a fundamental quantity. The conversions of A_5 into either $\bar{g}_\rho$ (the ratio of T-violating to T-conserving coupling constants) or α_T (the ratio of T-violating to T-conserving nuclear matrix elements) has been discussed in detail in Chapter 2. Using this framework and the value of A_5 extracted in Chapter 5

$$A_5 = 8.6 \pm 7.7 \times 10^{-6}, \tag{6.1}$$

a bound on $\bar{g}_\rho$ can be extracted and is given by

$$\bar{g}_\rho = 2.3 \pm 2.1 \times 10^{-2}. \tag{6.2}$$

For comparison purposes, the value of $\bar{g}_\rho$ can be converted into α_T, yielding

$$\alpha_T = 2.8 \pm 2.5 \times 10^{-4}. \tag{6.3}$$

This value thus sets a bound on time-reversal violation at the 95% confidence level of

$$\alpha_T \lesssim 7.1 \times 10^{-4}. \tag{6.4}$$

This bound can now be compared with measurements of time-reversal invariance in other systems.

Previously, the detailed balance measurement of Blanke *et al.* [Bla83] had provided the most stringent direct test of time-reversal invariance. They tested detailed balance through differential cross section measurements of the mirror reactions $^{27}\mathrm{Al}(\mathrm{p},\alpha)^{24}\mathrm{Mg}$ and $^{24}\mathrm{Mg}(\alpha,\mathrm{p})^{27}\mathrm{Al}$. Measurements were performed in the resonance region ($\sim$ 10 MeV) with the differential cross sections for the two reactions agreeing to within $\Delta = 5.1 \times 10^{-3}$ (80% confidence).

Numerous analyses have been performed to relate Δ to either ξ (the ratio of T-violating to T-conserving amplitudes in the reaction) or α_T. Ultimately, a bound on $\bar{g}_\rho$ is desired, but none of the analyses perform this final step. Therefore, we compare this experiment with our value of α_T.

The original analysis performed by Blanke *et al.* [Bla83] extracts a bound of $\xi \leq 5 \times 10^{-4}$ (80%). This result depends on the unknown phase between the T-violating and T-conserving parts of the reaction amplitude. In fact, if this phase is $\frac{\pi}{2}$, this measurement provides no information on ξ. Harney *et al.* [Har90] have further criticized the extraction of ξ by noting that the bound is not independent of the normalization procedure. Finally, the step in converting ξ to α_T is not performed.

A preliminary analysis by Boosé *et al.* [Boo86a] completes this step by converting ξ to α_T. Using the value of ξ quoted by Blanke *et al.*, they extract a bound on α_T of 2.7×10^{-3} (80%). A complete analysis [Boo86b] does not however give an α_T value. Further, both analyses contain an erroneous factor of $\frac{1}{4}$ in the definition of the observable [Har90].

An independent analysis performed by French *et al.* [Fre87] extracts a bound on α_T of 3.5×10^{-3} (99%). This analysis pays careful attention to confidence limits, but ignores the statistical error in the original data, thus artifically lowering the bound.

The most recent limit has been presented by Harney *et al.* [Har90], yielding a value of $\alpha_T = 2.6 \times 10^{-4}$ at the 80% confidence level. This is the most precise value claimed in the literature, but it gains a questionable factor of $\frac{1}{n}$ in precision by grouping data points that lie within a given correlation length into a single measurement, yielding n independent measurements. The bound thus depends heavily on the correlation length and the grouping

of the data. Typical values of n were 26 to 44.

An analysis similar to Harney *et al.* has been performed by Bunakov *et al.* [Bun93] using a Bayesian approach. They extract a similar value of $\xi = 1.33 \times 10^{-3}$ (80%) compared to the analysis of Harney ($\xi = 1.25 \times 10^{-3}$ (80%)), but do not convert this value to a bound on α_T. This analysis also contains the factor of $\frac{1}{n}$, depending upon the correlation length and grouping of the data.

The analyses by Harney *et al.* [Har90] and Bunakov *et al.* [Bun93] obtain a lower bound by grouping data into independent measurements. Davis has shown that the T-violating observable when energy-averages are considered, is the variance of the deviation of the cross section from zero [Dav88]. Thus independent measurements at the same precision can not be used to lower the variance, but serve only to raise the confidence level of the bound.

The comparison of our value of $\bar{g}_\rho$ to the detailed balance measurements depends heavily on which analysis is chosen. The most recent analyses of Harney *et al.* [Har90] and Bunakov *et al.* [Bun93] obtain a factor of ten lower bound using the questionable procedure of grouping the data into independent measurements. We believe this procedure is not valid and therefore compare our results to the bounds set by French *et al.* [Fre87] and Boosé *et al.* [Boo86a][1]. Using these for comparison, our measurement represents an improvement of a factor of four to five over the detailed balance measurements of Blanke *et al.* [Bla83].

A second set of measurements that set constraints on the P-conserving, T-violating interaction are the P-non-conserving, T-violating electric dipole moment (edm) measurements. Haxton *et al.* [Hax94] have identified three mechanisms whereby P-non-conserving, T-violating observables can be generated through weak corrections to P-conserving, T-violating interactions. Measurements of the neutron electric dipole moment ($d \lesssim 8 \times 10^{-26}$ e cm [Smi90, Alt92]) and the atomic electric dipole moment of ^{199}Hg ($d \lesssim 1.3 \times 10^{-27}$ e cm [Jac93]) are used to set constraints on α_T. The neutron edm bound on α_T depends inversely on the as of yet unknown P-violating πNN coupling constant f_π [Hax94].

[1] In a similar comparison, Haxton *et al.* [Hax94] chooses to compare their results to those set by French *et al.* [Fre87].

This term is predicted to be large in meson exchange models [Des80], but measurements to date have shown the value is small and consistant with zero [Ade85]. Since the magnitude of this term is controversial, we do not consider this mechanism further.

The atomic edm measurement of ^{199}Hg, on the other hand, sets a bound independent of f_π, that is $\alpha_T \lesssim 1.1 \times 10^{-4}$ at the 95% confidence level [Hax94]. This bound is more restrictive than the bound set by the present measurement, but we emphasize it is not a bound on a dynamical process. The P-conserving, T-violating bounds set from dipole moment measurements are indirect bounds on α_T. Values of α_T arising from these edm measurements are complementary to the bounds set by the present direct measurement.

The present bound of $\alpha_T \lesssim 7 \times 10^{-4}$ represents the most precise direct test of parity-conserving, time-reversal invariance in nuclear physics. It represents a factor of four improvement over the previous measurements of Blanke *et al.* [Bla83, Boo86a, Fre87].

Future improvements of the direct bounds on P-conserving, T-violating interactions using measurements of the five-fold correlation term in the total cross section are possible in the epithermal energy regime. These measurements take advantage of resonance enhancements. A search for resonances suitable for such a test has been carried out, and a number of candidates have been located [Huf95]. Neutron depolarization in the crystal is a potential problem, and measurements of the neutron depolarization in holmium have been performed [Alf95]. Future measurements searching for d-wave admixtures (required for a FC test) in small s-wave resonances in holmium are planned. A FC measurement in the resonance region could in favorable cases lower the direct bounds on time-reversal invariance by one to two orders of magnitude.

Appendix A

Spin-Dependent Cross Section

For a given reaction $\vec{\mathrm{A}}\,(\vec{\mathrm{a}},\mathrm{a}')\,\mathrm{A}'$, the total angular momentum, $\boldsymbol{J} = \boldsymbol{\ell} + \boldsymbol{s} + \boldsymbol{I}$, is conserved. The spin-orbit spin-coupling scheme is used to couple the incident projectile spin, s, the target spin, I, and their relative angular momentum, ℓ:

$$\boldsymbol{\ell} + \boldsymbol{s} = \boldsymbol{j} \qquad \boldsymbol{j} + \boldsymbol{I} = \boldsymbol{J}. \tag{A.1}$$

The total cross section, σ_T, is given by the generalized spin-dependent optical theorem

$$\begin{aligned} \sigma_T &= 4\pi\lambda\!\!\!^{-}\mathrm{Im}\left\{\mathrm{Tr}\left(\rho_{Mm,M'm'}\, f'_{M'm',Mm}\,(0^\circ)\right)\right\} \\ &= 4\pi\lambda\!\!\!^{-}\mathrm{Im}\left\{\sum_{Mm}\sum_{M'm'} \rho_{Mm,M'm'}\, f'_{M'm',Mm}\,(0^\circ)\right\}, \end{aligned} \tag{A.2}$$

where $\rho_{Mm,M'm'}$ is the density matrix and $f'_{M'm',Mm}\,(0^\circ)$ is the forward scattering amplitude [Phi63]. Since the polarizations of the target and incident beam are uncoupled, the density matrix can be factored into a direct product of the density matrices of the individual nuclei

$$\rho_{Mm,M'm'} = \rho_{MM'}\,\rho_{mm'}, \tag{A.3}$$

and can further be expressed in terms of statistical tensors t_{kq} (Section 2.1) using

$$\rho_{MM'} = \sum_{kq} t_{kq}\,(-1)^{J-M}\,\hat{J}^{-1}\left\langle JJM', -M|kq\right\rangle \tag{A.4}$$

where $\hat{J} = \sqrt{(2J+1)}$ [Sat83]. Insertion of Equation A.4 into Equation A.3 yields the generalized density matrix expressed in terms of statistical tensors

$$\begin{aligned}\rho_{Mm,M'm'} &= \sum_{KQkq} t_{KQ}(I) t_{kq}(s) \, (-1)^{I+s-M-m} \, \hat{I}^{-1} \hat{s}^{-1} \\ &\quad \times \left\langle IIM' - M | KQ \right\rangle \left\langle ssm' - m | kq \right\rangle . \end{aligned} \tag{A.5}$$

The generalized spin-dependent scattering amplitude is given by Satchler [Sat83] and is expressed in terms of angular momentum coupling constants and the S-matrix for the given reaction. For arbitrary angles θ and ϕ, the scattering amplitude is

$$\begin{aligned} f'_{M'm',Mm}(\theta,\phi) &= \frac{\lambda\!\!\!^{-}}{2i} \sum_{JM_J} \sum_{\substack{\ell' \ell \\ j' j}} \langle \ell s 0 m | j m \rangle \, \langle j I m M | J M_J \rangle \\ &\quad \times \left\langle \ell' s M'_\ell m' | j' M_J - M' \right\rangle \hat{\ell} e^{i(\sigma_\ell + \sigma'_\ell)} \\ &\quad \times \left\langle j' I M_J - M', M' | J M_J \right\rangle \\ &\quad \times (4\pi)^{\frac{1}{2}} \, Y_{\ell'}^{M'_\ell}(\theta,\phi) \left[S^J_{\ell' j', \ell j} - \delta_{\ell' \ell} \delta_{j' j} \right] , \end{aligned} \tag{A.6}$$

where $\lambda\!\!\!^{-}$ is the reduced wavelength and $\langle ab\alpha\beta | c\gamma \rangle$ is a standard Clebsch-Gordan coefficient [Bri71]. In the forward direction, $(0^\circ, \phi) \equiv \hat{\boldsymbol{k}}$, the spherical harmonic $Y_{\ell'}^{M'_\ell}(0^\circ, \phi)$ is restricted to $M'_\ell = 0$ due to symmetry. Also, the Coulomb Phase Shift, σ_ℓ, can easily be shown to vanish for neutron scattering:

$$\sigma_\ell = \arg \Gamma (\ell + 1 + i n) \tag{A.7}$$

where n is the usual Coulomb parameter,

$$n = \frac{Z_a Z_A e^2 \mu}{\hbar^2 k} = 0. \tag{A.8}$$

This implies that

$$\begin{aligned} \sigma_\ell &= \arg \Gamma (\ell + 1) = 0 \\ \sigma'_\ell &= \arg \Gamma (\ell' + 1) = 0. \end{aligned} \tag{A.9}$$

Including these conditions into Equation A.6 gives the complete forward scattering amplitude:

$$f'_{M'm',Mm}(0^\circ,\phi) = \frac{\lambda\!\!\!^{-}}{2i} \sum_{JM_J} \sum_{\substack{\ell' \ell \\ j' j}} \hat{\ell} \, \langle \ell s 0 m | j m \rangle \, \langle j I m M | J M_J \rangle$$

$$\times \left\langle \ell' s 0 m' | j' M_J - M' \right\rangle \left\langle j' I (M_J - M') M' | J M_J \right\rangle$$
$$\times (4\pi)^{\frac{1}{2}} Y^0_{\ell'}(\hat{\boldsymbol{k}}) \left[S^J_{\ell' j', \ell j} - \delta_{\ell' \ell} \delta_{j' j} \right]. \quad \text{(A.10)}$$

Substitution of Equations A.5 and A.10 into Equation A.2 gives an expression for the total cross section:

$$\begin{aligned} \sigma_T &= \mathrm{Im}\Bigg\{ \frac{(4\pi)^{\frac{3}{2}}}{2i} \lambda\!\!\!^{-2} \sum_{\substack{Kk \\ Qq}} \sum_{JM_J} \sum_{\substack{\ell' \ell \\ j' j}} \sum_{\substack{Mm \\ M' m'}} t_{KQ}(I)\, t_{kq}(s) \\ &\quad \times (-1)^{I+s-M-m}\, \hat{I}^{-1} \hat{s}^{-1} \hat{\ell} \left\langle II M' - M | KQ \right\rangle \\ &\quad \times \left\langle ss m' - m | kq \right\rangle \left\langle \ell s 0 m | j m \right\rangle \left\langle j I m M | J M_J \right\rangle \left\langle \ell' s 0 m' | j' m' \right\rangle \\ &\quad \times \left\langle j' I m' M' | J M_J \right\rangle Y^0_{\ell'}(\hat{\boldsymbol{k}}) \left[S^J_{\ell' j', \ell j} - \delta_{\ell' \ell} \delta_{j' j} \right] \Bigg\}. \end{aligned} \quad \text{(A.11)}$$

For convenience, define Ψ to be

$$\Psi = \sum_{\substack{MM' \\ M_J}} (-1)^{-M-m} \left\langle j I m M | J M_J \right\rangle \left\langle II M' - M | KQ \right\rangle \left\langle j' I m' M' | J M_J \right\rangle \quad \text{(A.12)}$$

where

$$\begin{aligned} \sigma_T &= \mathrm{Im}\Bigg\{ \frac{(4\pi)^{\frac{3}{2}}}{2i} \lambda\!\!\!^{-2} \sum_{\substack{Kk \\ Qq}} \sum_{J} \sum_{\substack{\ell' \ell \\ j' j}} \sum_{mm'} t_{KQ}(I)\, t_{kq}(s)\, \Psi \\ &\quad \times (-1)^{I+s}\, \hat{s}^{-1} \hat{I}^{-1} \hat{\ell} \left\langle ss m' - m | kq \right\rangle \left\langle \ell s 0 m | j m \right\rangle \\ &\quad \times \left\langle \ell' s 0 m' | j' m' \right\rangle Y^0_{\ell'}(\hat{\boldsymbol{k}}) \left[S^J_{\ell' j', \ell j} - \delta_{\ell' \ell} \delta_{j' j} \right] \Bigg\}. \end{aligned} \quad \text{(A.13)}$$

Converting the Clebsch-Gordan coefficients in Equation A.12 into Wigner *3-j* symbols using

$$\left\langle ab\alpha\beta | c - \gamma \right\rangle = (-1)^{a-b-\gamma} (2c+1)^{\frac{1}{2}} \begin{pmatrix} a & b & c \\ \alpha & \beta & \gamma \end{pmatrix} \quad \text{(A.14)}$$

[Bri71] gives

$$\begin{aligned} \Psi &= \sum_{\substack{MM' \\ M_J}} (-1)^{-M-m} (-1)^{j+j'-2I+2M_J+Q} (2J+1) \hat{K} \\ &\quad \times \begin{pmatrix} j & I & J \\ m & M & -M_J \end{pmatrix} \begin{pmatrix} I & I & K \\ M' & -M & -Q \end{pmatrix} \begin{pmatrix} j' & I & J \\ m' & M' & -M_J \end{pmatrix}. \end{aligned} \quad \text{(A.15)}$$

After rearranging terms using the symmetry properties of the *3-j* symbols

$$\begin{aligned}\begin{pmatrix} a & b & c \\ \alpha & \beta & \gamma \end{pmatrix} &= (-1)^{a+b+c} \begin{pmatrix} b & a & c \\ \beta & \alpha & \gamma \end{pmatrix} \\ &= (-1)^{-a-b-c} \begin{pmatrix} a & b & c \\ -\alpha & -\beta & -\gamma \end{pmatrix} \end{aligned} \tag{A.16}$$

[Bri71] one obtains

$$\begin{aligned}\Psi &= \sum_{\substack{MM' \\ M_J}} (-1)^{-M-m} (-1)^{j+j'-2I+2M_J+Q} (2J+1)\hat{K} \\ &\times \begin{pmatrix} j & J & I \\ -m & M_J & -M \end{pmatrix} \begin{pmatrix} I & K & I \\ -M' & Q & M \end{pmatrix} \begin{pmatrix} J & I & j' \\ M_J & -M' & -m' \end{pmatrix}. \end{aligned} \tag{A.17}$$

Since $M_J = M + m = M' + m'$, one can rewrite Equation A.17 into a form that can be readily simplified:

$$\begin{aligned}\Psi &= (-1)^{j-I+Q+m'-m} (2J+1)\hat{K} \sum_{\substack{MM' \\ M_J}} (-1)^{j'-I+m+M'} \\ &\times \begin{pmatrix} j & J & I \\ -m & M_J & -M \end{pmatrix} \begin{pmatrix} I & K & I \\ -M' & Q & M \end{pmatrix} \begin{pmatrix} J & I & j' \\ M_J & -M' & -m' \end{pmatrix}. \end{aligned} \tag{A.18}$$

Carrying out the summations using

$$\begin{aligned} W(abcd;ef) &\begin{pmatrix} c & a & f \\ \gamma & \alpha & \phi \end{pmatrix} = \\ &\sum_{\beta\delta\epsilon} (-1)^{f-e-\alpha-\delta} \begin{pmatrix} a & b & e \\ \alpha & \beta & -\epsilon \end{pmatrix} \begin{pmatrix} d & c & e \\ \delta & \gamma & \epsilon \end{pmatrix} \begin{pmatrix} b & d & f \\ \beta & \delta & -\phi \end{pmatrix}, \end{aligned} \tag{A.19}$$

[Bri71] one obtains

$$\Psi = (-1)^{j-I+Q+m'-m} (2J+1)\hat{K} W\left(jJKI; Ij'\right) \begin{pmatrix} K & j & j' \\ Q & -m & m' \end{pmatrix}. \tag{A.20}$$

Substituting Ψ into Equation A.13 yields

$$\begin{aligned}\sigma_T &= \mathrm{Im}\Bigg\{\frac{(4\pi)^{\frac{3}{2}}}{2i}\lambda\!\!\!^{-2}\sum_{KkQq} t_{KQ}(I)\, t_{kq}(s)\,(-1)^{I+s}\sum_{\ell'\ell j'j}\hat{\ell}\hat{I}^{-1}\hat{s}^{-1}\hat{K} \\ &\quad\times\sum_{J}(2J+1)\sum_{mm'}(-1)^{j-I+Q+m'-m}\,W\big(jJKI;Ij'\big) \\ &\quad\times\begin{pmatrix} K & j & j' \\ Q & -m & m' \end{pmatrix}\big\langle ssm'-m|kq\big\rangle\,\langle \ell s0m|jm\rangle \\ &\quad\times\big\langle \ell' s0m'|j'm'\big\rangle\, Y^0_{\ell'}(\hat{\boldsymbol{k}})\left[S^J_{\ell'j',\ell j}-\delta_{\ell'\ell}\delta_{j'j}\right]\Bigg\}. \end{aligned} \tag{A.21}$$

Converting the remaining Clebsch-Gordan coefficients into *3-j* symbols and rearranging the order of the Racah coefficients using $W(abcd;ef) = W(badc;ef)$ [Bri71] one obtains

$$\begin{aligned}\sigma_T &= \mathrm{Im}\Bigg\{\frac{(4\pi)^{\frac{3}{2}}}{2i}\lambda\!\!\!^{-2}\sum_{KkQq} t_{KQ}(I)\, t_{kq}(s)\sum_{J}(2J+1)\sum_{\ell'\ell j'j}\hat{\ell}\hat{I}^{-1}\hat{s}^{-1}\hat{K}\hat{k}\hat{j}\hat{j}' \\ &\quad\times\sum_{mm'}(-1)^{j+I+Q+m'-m}\,(-1)^{\ell+\ell'-2s+q+m+m'}\,W\big(JjIK;Ij'\big) \\ &\quad\times\begin{pmatrix} K & j & j' \\ Q & -m & m' \end{pmatrix}\begin{pmatrix} s & s & k \\ m' & -m & -q \end{pmatrix}\begin{pmatrix} \ell & s & j \\ 0 & m & -m \end{pmatrix} \\ &\quad\times\begin{pmatrix} \ell' & s & j' \\ 0 & m' & -m' \end{pmatrix} Y^0_{\ell'}(\hat{\boldsymbol{k}})\left[S^J_{\ell'j',\ell j}-\delta_{\ell'\ell}\delta_{j'j}\right]\Bigg\}. \end{aligned} \tag{A.22}$$

Rearranging the *3-j* symbols into a form that can be simplified gives

$$\begin{aligned}\sigma_T &= \mathrm{Im}\Bigg\{\frac{(4\pi)^{\frac{3}{2}}}{2i}\lambda\!\!\!^{-2}\sum_{\substack{Kk\\Qq}} t_{KQ}(I)\, t_{kq}(s)\sum_{J}(2J+1)\sum_{\substack{\ell'\ell\\j'j}}\hat{\ell}\hat{I}^{-1}\hat{s}^{-1}\hat{K}\hat{k}\hat{j}\hat{j}' \\ &\quad\times\sum_{mm'}(-1)^{j+2m'+\ell+\ell'-s+Q+q}\,(-1)^{7s+2k+2j'+j+2\ell'+\ell} \\ &\quad\times W\big(JjIK;Ij'\big)\begin{pmatrix} k & s & s \\ -q & m' & -m \end{pmatrix}\begin{pmatrix} K & j' & j \\ -Q & -m' & m \end{pmatrix} \\ &\quad\times\begin{pmatrix} j' & \ell' & s \\ -m' & 0 & m' \end{pmatrix}\begin{pmatrix} j & \ell & s \\ m & 0 & -m \end{pmatrix} Y^0_{\ell'}(\hat{\boldsymbol{k}})\left[S^J_{\ell'j',\ell j}-\delta_{\ell'\ell}\delta_{j'j}\right]\Bigg\}. \end{aligned} \tag{A.23}$$

After noting that $j'+m'$ must be an integer, the sum over the m's can be carried out using

$$\sum_b (2b+1)\begin{pmatrix} a & b & c \\ \alpha & \beta & \gamma \end{pmatrix}\begin{pmatrix} b & e & h \\ \beta & \epsilon & \eta \end{pmatrix}\begin{Bmatrix} a & b & c \\ d & e & f \\ g & h & i \end{Bmatrix} = \sum_{\phi\nu\delta\rho}\begin{pmatrix} c & f & i \\ \gamma & \phi & \nu \end{pmatrix}\begin{pmatrix} a & d & g \\ \alpha & \delta & \rho \end{pmatrix}\begin{pmatrix} d & e & f \\ \delta & \epsilon & \phi \end{pmatrix}\begin{pmatrix} g & h & i \\ \rho & \eta & \nu \end{pmatrix}, \tag{A.24}$$

[Bri71] which yields

$$\begin{aligned}\sigma_T &= \mathrm{Im}\Bigg\{\frac{(4\pi)^{\frac{3}{2}}}{2i}\lambda\!\!\!^{-2}\sum_{KkQq} t_{KQ}(I)\,t_{kq}(s)\sum_{\ell'\ell j'j}\hat{\ell}\hat{I}^{-1}\hat{s}^{-1}\hat{K}\hat{k}\hat{j}\hat{j} \\ &\quad\times(-1)^{2j+2s+\ell'+Q+q}\sum_J(2J+1)W\big(JjIK;Ij'\big)\sum_\Lambda(2\Lambda+1) \\ &\quad\times\begin{pmatrix} K & \Lambda & k \\ -Q & M_\Lambda & -q \end{pmatrix}\begin{pmatrix} \Lambda & \ell' & \ell \\ M_\Lambda & 0 & 0 \end{pmatrix}\begin{Bmatrix} K & \Lambda & k \\ j' & \ell' & s \\ j & \ell & s \end{Bmatrix} \\ &\quad\times Y^0_{\ell'}(\hat{\boldsymbol{k}})\left[S^J_{\ell' j',\ell j}-\delta_{\ell'\ell}\delta_{j'j}\right]\Bigg\}.\end{aligned} \tag{A.25}$$

From the second *3-j* symbol in Equation A.25, $M_\Lambda = 0$. Likewise, from the first *3-j* symbol, $Q = -q$. Rearranging the *3-j* and *9-j* symbols gives

$$\begin{aligned}\sigma_T &= \mathrm{Im}\Bigg\{\frac{(4\pi)^{\frac{3}{2}}}{2i}\lambda\!\!\!^{-2}\sum_{Kk}\sum_q t_{K-q}(I)\,t_{kq}(s)\sum_J(2J+1)\sum_{\ell'\ell j'j}\hat{\ell}\hat{I}^{-1}\hat{s}^{-1}\hat{K}\hat{k}\hat{j}\hat{j}' \\ &\quad\times(-1)^{2j+2s+\ell'+K+\Lambda+k}W\big(JjIK;Ij'\big)\sum_\Lambda(2\Lambda+1)\begin{pmatrix} \Lambda & k & K \\ 0 & q & -q \end{pmatrix} \\ &\quad\times\begin{pmatrix} \ell & \Lambda & \ell' \\ 0 & 0 & 0 \end{pmatrix}\begin{Bmatrix} j' & \ell' & s \\ j & \ell & s \\ K & \Lambda & k \end{Bmatrix}Y^0_{\ell'}(\hat{\boldsymbol{k}})\left[S^J_{\ell' j',\ell j}-\delta_{\ell'\ell}\delta_{j'j}\right]\Bigg\}.\end{aligned} \tag{A.26}$$

If $\ell+\Lambda+\ell'$ is odd, the Clebsch-Gordan coefficient $\langle \ell\Lambda 00|\ell' 0\rangle$ is zero. Also, since $j+s$ must be an integer, most of the factors of -1 can be eliminated. After converting the *3-j* symbols into Clebsch-Gordan coefficients one obtains

$$\begin{aligned}\sigma_T &= \mathrm{Im}\Bigg\{ \frac{(4\pi)^{\frac{3}{2}}}{2i}\lambda\!\!\!^{-2} \sum_{Kk}\sum_{\Lambda q} t_{K-q}\,(I)\, t_{kq}\,(s) \sum_{J}(2J+1)\sum_{\substack{\ell'\ell\\ j'j}} \hat{\ell}\hat{I}^{-1}\hat{s}^{-1}\hat{k}\hat{j}\hat{j}' \\ &\quad \times (-1)^{K+q}\, W\big(JjIK;Ij'\big)\,\hat{\Lambda}^2\,\langle \Lambda k 0 q|Kq\rangle\,\big\langle \ell\Lambda 00|\ell' 0\big\rangle \\ &\quad \times \begin{Bmatrix} j' & \ell' & s \\ j & \ell & s \\ K & \Lambda & k \end{Bmatrix} Y^0_{\ell'}(\hat{\boldsymbol{k}})\left[S^J_{\ell' j',\ell j} - \delta_{\ell'\ell}\delta_{j' j}\right]\Bigg\}. \end{aligned} \tag{A.27}$$

Equation A.27 can easily be rewritten into the form of Hnizdo and Gould [Hni94b]. Noting that $T^J_{\ell' j'\ell j} = (1/2i)[S^J_{\ell' j',\ell j} - \delta_{\ell\ell'}\delta_{jj'}]$ and

$$\langle \Lambda k 0 q|Kq\rangle = (-1)^{\Lambda+2k-K-q}\frac{\hat{K}}{\hat{\Lambda}}\,\langle kKq\,-q|\Lambda 0\rangle\,, \tag{A.28}$$

the total cross section in the spin-orbit representation can be rewritten as a sum of partial cross sections that depend on the rank of the polarization of the beam (k) and target(K). Factoring out the diagonal polarization tensors $\tilde{t}_{kq}$ defined by Equation 2.2, one obtains an expression for the total cross section

$$\sigma_T = \sum_{kK}\tilde{t}_{k0}(s)\tilde{t}_{K0}(I)\sigma_{kK}, \tag{A.29}$$

where

$$\begin{aligned}\sigma_{kK} &= \frac{(4\pi)^{\frac{5}{2}}}{\hat{s}\hat{I}}\lambda\!\!\!^{-2}\mathrm{Im}\sum_{\Lambda q}(-1)^{\Lambda}\hat{\Lambda}\,\langle kKq\,-q|\Lambda 0\rangle\, Y^q_k(\hat{\boldsymbol{s}})\, Y^{-q}_K(\hat{\boldsymbol{I}}) \\ &\quad \times \sum_{J\ell j\ell' j'}(2J+1)\hat{\ell}\hat{\ell'}^{-1}\hat{j}\hat{j}'\, Y^0_{\ell'}(\hat{\boldsymbol{k}})\,\big\langle l\Lambda 00|l' 0\big\rangle \\ &\quad \times W\big(JjIK;Ij'\big)\begin{Bmatrix} \ell & s & j \\ \Lambda & k & K \\ \ell' & s & j' \end{Bmatrix} T^J_{\ell' j'\ell j}. \end{aligned} \tag{A.30}$$

Using the property of the spherical harmonics

$$Y^0_{\ell'}(\hat{\boldsymbol{k}}) = \sqrt{\frac{4\pi}{(2\ell'+1)}} = \frac{\hat{\Lambda}}{\hat{\ell}'} Y^0_{\Lambda}(\hat{\boldsymbol{k}}) \tag{A.31}$$

and the tensor product notation given by Equation 2.9, we obtain the form given by Hnizdo and Gould [Hni94b]:

$$\sigma_T = \sum_{kK} \tilde{t}_{k0}(s)\tilde{t}_{K0}(I)\sigma_{kK} \tag{A.32}$$

where

$$\begin{aligned}
\sigma_{kK} &= 4\pi\lambda\!\!\!^{-2}\frac{\hat{k}\hat{K}}{\hat{s}\hat{I}}\mathrm{Im}\sum_{\Lambda}\hat{\Lambda}C_{kK\Lambda}(\hat{\boldsymbol{s}}\hat{\boldsymbol{I}}\hat{\boldsymbol{k}})\sum_{J\ell j\ell' j'}\hat{\ell}\hat{j}\hat{j}'\left\langle \ell\Lambda 00|\ell' 0\right\rangle \\
&\quad \times W\left(JjIK;Ij'\right)\left\{\begin{array}{ccc} \ell & s & j \\ \Lambda & k & K \\ \ell' & s & j' \end{array}\right\} T^J_{\ell' j' \ell j}
\end{aligned} \tag{A.33}$$

and

$$C_{kK\Lambda}(\hat{\boldsymbol{s}}\hat{\boldsymbol{I}}\hat{\boldsymbol{k}}) = \frac{(4\pi)^{\frac{3}{2}}}{\hat{k}\hat{K}}\left[\left[Y^q_k(\hat{\boldsymbol{s}})\otimes Y^{-q}_K(\hat{\boldsymbol{I}})\right]_{\Lambda 0}\otimes Y^0_{\Lambda}(\hat{\boldsymbol{k}})\right]_{00}. \tag{A.34}$$

Appendix B

Multiple Scattering Events

Monte-Carlo calculations of the neutron transport through the experimental setup are performed to estimate the percentage of scattered events reaching the 0° detectors. These calculations are performed on a Sun Sparc-2 using the computer code MCNP-4A [JFB93] — or the Monte-Carlo N-Particle Transport Code System. This code is used for neutron transport calculations through three-dimensional volumes using the current ENDF neutron cross sections to model the reactions.

The three-dimensional geometry for the calculation is specified in the input file. Outer surfaces of the materials are specified using planes, cylinders, cones, or spheres. Volume elements are then specified by the union of these surfaces to define a closed cell. The cell is parameterized by specifying its material composition and density.

The amount of computer time required for a calculation increases exponentially with the number of geometrical cells. To minimize the time required for these calculations, only relevant materials were included in the geometry. For the present calculations, the geometry includes the following materials: the copper and gold surrounding the deuterium gas cell, the copper coldfinger and stainless steel housing of the gas cell, the lower sections of the liquid nitrogen jacket, the liquid helium jacket, and the vacuum cans for the dilution refrigerator, the holmium target and its mounting apparatus, and the monitor and 0° detector arrays. These include all materials within the solid angle of the 0° detector and the immediate

surrounding area.

The neutron production target was modeled using a general source tailored to the ^{2}H(d, n)^{3}He reaction. The neutrons emerge in a uniform distribution from a cylindrical volume of diameter 0.63 cm and length 3.81 cm. The neutron energy is chosen randomly between 5 and 8 MeV. The flux from the reaction is forward peaked about the direction of the neutron momentum using an exponential weighting of the form $p(\mu) = ce^{a\mu}$, where μ specifies the direction cosine. The coefficient a was determined using a fit to the known angular cross section of the ^{2}H(d, n)^{3}He reaction, yielding a value of $a = 24.6$.

The material cells and neutron source parameters are included in the input file for the calculations. A sample input file is given at the end of this appendix. The first section of the file defines the material cells using the union of the surfaces defined in the section immediately following. The next sections define the materials used in the calculations, the rotation angles for surfaces not perpendicular to the coordinate axes, the source configuration, and the tally cards which will be discussed later. The remaining lines specify the cut-off energy for neutrons in the simulation (taken to be 1.5 MeV), the number of neutrons produced in the production cell, and the starting random number. Note that the code is designed so that two calculations using the same random number and geometry are identical.

Calculations were performed for a number of geometries in the initial design stages of this experiment. The locations of the detectors and neutron production target are chosen such that unscattered neutrons reaching the 0° detectors must pass through the holmium sample. Quantities such as multiple scattering events — or cross-talk — between the detectors are estimated from these calculations. Cross-talk values of $\sim 1\%$ are calculated between the 0° detectors, consistent with the measured values presented in Chapter 4.

The code MCNP can tally the number of neutrons passing through a surface and flag neutrons that scatter before reaching this surface. These tally mechanisms are used to estimate the effective target thickness, the efficiencies of both the 0° and monitor detectors, and the number of neutrons reaching the detector from small angle scattering within the

holmium.

The experimental setup for the time reversal measurement is used in calculating the small angle scattering events within the holmium sample. Information contained within the tally outputs give the number of neutrons entering a surface having scattered somewhere, but give no information on the location of this scattering event. Multiple tallies must therefore be used to extract the small angle scattering percentage within the holmium.

The small angle scattering events — or inscattering — within the holmium is determined using the tally outputs tracking the number of neutrons that scatter, pass through the holmium, and pass through the front surface of the 0° detector array. A second Monte-Carlo calculation is performed with an empty cell in place of the holmium sample extracting the same information. Combining the information contained in these two calculations, the small angle scattering events within the holmium sample is determined.

Three calculations are performed for both the sample in and sample out configurations. For consistency, the neutron projections for each pair of calculations were identical using the same initial random number. The results of these calculations suggest that $\sim 1\%$ of the counts in the 0° detector arise from small angle scattering events within the holmium sample.

Scattering events from other sources into the 0° detectors can not be estimated because the majority of these scattering events occur before the sample, in the area surrounding the gas cell. In principle, these scattered neutrons do not effect the time-reversal measurement because the majority of these neutrons pass through the holmium. These events are less than 10% of the total count rate and the percentage that enter the detector not passing through the holmium is less than 1%.

The above calculations can also be used to measure the thickness of the holmium sample. Taking the ratio of the number of neutrons that scatter within the holmium to the total number that enter the sample, and using the known cross section of $\sigma = 5.1$ b, the target thickness is found to be $n = 0.065$ at/b. This value is larger than the chord approximation value of Koster [Kos90], which yielded $n = 0.058$ at/b. The MCNP calculation

takes into account the non-uniform beam profile, in which a larger neutron flux passes through the center of the target than at the edges, increasing the effective target thickness. A target thickness of $n = 0.065$ at/b is used in the analysis of the time-reversal data presented in Chapter 6.

The relative efficiencies of the two sets of detectors can be calculated in the same manner by taking the ratio of the number of neutrons scattered within the scintillation material to the number of neutrons entering. These calculations were used in the initial design stages of the experiment to determine the optimum thickness for the monitor detector array. This thickness was chosen to be 1.27 cm based on the detector efficiency and count rates in the photomultiplier tubes. In the present experimental setup, these efficiencies were calculated for both detector arrays. The 0° detector array has an efficiency of 62% and the monitor array has an efficiency of 15%.

In summary, these calculations set limits on small angle scattering events within the holmium sample, determine the effective target thickness of the holmium sample, and estimate the efficiencies of the two detector arrays. These calculations were also essential in the initial design stages of this experiment.

```
Sample input file for the MCNP calculations using the geometry of the FC expt.
1      0           24 -25 -26                  $ BEAM SPOT OF GAS CELL (GC)
2      1 -8.80     29 -30 -27                  $ HOLMIUM (HO)
3      2 -1.032    -21 22 15 -19 20 -18        $ DETECTOR TOP LEFT
4      2 -1.032    -21 22 19 -16 20 -18        $ DETECTOR TOP RIGHT
5      2 -1.032    -21 22 15 -19 17 -20        $ DETECTOR BOTTOM LEFT
6      2 -1.032    -21 22 19 -16 17 -20        $ DETECTOR BOTTOM RIGHT
7      2 -1.032    1 -2(-10 19 14 -12:-14 12 20 $ MONITOR 1 (MO)
                   -7:-3 12 14 -7 -10)         $
8      2 -1.032    1 -2(-10 -19 14 11:-14 -11   $ MONITOR 2
                   20 8:-4 -11 14 8 -10)       $
9      2 -1.032    1 -2(9 19 -13 -12:13 12 -20  $ MONITOR 3
                   -7:-5 12 -13 -7 9)          $
10     2 -1.032    1 -2(9 -19 -13 11:13 -11 -20 $ MONITOR 4
                   8 :-6 -11 -13 8 9)          $
11     3 -2.70     -116 115 -146 143           $ OUTER WALL (OW)
12     3 -2.70     -114 113 -140 141           $ LN2 JACKET (LN2)
13     4 -7.9      -112 111 -138 135           $ LHE DEWAR (LHE)
14     4 -7.9      -110 109 -132 133           $ DR VACUUM CAN (DRVC)
15     4 -7.9      -131 154 -147 109           $ TOP OF DRVC
16     4 -7.9      -133 134 -110               $ BOTTOM OF DRVC
17     4 -7.9      -137 138 -148 111           $ TOP OF LHE
18     4 -7.9      -135 136 -112               $ BOTTOM OF LHE
19     3 -2.70     -139 140 -149 113           $ TOP OF LN2
20     3 -2.70     -141 142 -114               $ BOTTOM OF LN2
21     3 -2.70     -145 146 -150 115           $ TOP OF OW
22     3 -2.70     -143 144 -116               $ BOTTOM OF OW
23     4 -7.9      -108 -103 106               $ COLDFINGER (CF)
                     #(-105 -108 107 106)      $
24     5 -8.96     -35 36 -25 24               $ COPPER GAS CELL BODY
25     6 -19.3     -36 33 -25 24:25 -34 -35    $ GOLD SLEEVE
26     5 -8.96     -41 42 -43 44 45 -46 35     $ GC CLAMP
27     5 -8.96     -47 48 -42                  $ GC COLDFINGER
28     5 -8.96     -49 53 29 -30 :30 -106 107  $ COPPER THING
                     -49:-51 106 107 -52:-105  $ LHE WOULD BE 135 -111
                     -49 107 52                $ 151 -138
29     4 -7.9      -63 -60 59 66               $ VACUUM HOUSING
30     4 -7.9      -62 63 -60                  $ TOP OF VACUUM HOUSING
31     4 -7.9      -61 -64 65 60               $ VACUUM FLANGE HOUSING
32     0           54 -55 -58 29 -30           $ TALLY CELL #1
33     0           56 -57 58 29 -30            $ TALLY CELL #2
34     0           -23 155 31 #(-151 152 -153) $ WORLD #1 (INCL CANS)
                     #11 #12 #13 #15 #17       $
                     #18 #19 #20 #21 #22       $
35     0           -151 152 -153 #2 #14 #16 #23 $ WORLD #2 (INCL HO & CF)
                     #28 #32 #33               $
36     0           -31 -32 #1 #24 #25 #26      $ WORLD #3 (INCL GS)
                     #27 #29 #30 #31           $
37     0           -31 32 20 #7 #8             $ WORLD #4 (INCL MO 1&2)
38     0           -31 32 -20 #9 #10           $ WORLD #5 (INCL MO 3&4)
39     0           -155 #3 #4 #5 #6            $ WORLD #4 (INCL DETECT)
40     0           23                          $ VOID

1        PY  -8.414                $ BACK OF MO (1/2" THICK)
2        PY  -7.144                $ FRONT OF MO
```

```
3        P    1 0 1 3.592            $ TOP LEFT SIDE OF MO
4        P   -1 0 1 3.592            $ TOP RIGHT SIDE OF MO
5        P    1 0 -1 3.592           $ BOTTOM LEFT SIDE OF MO
6        P   -1 0 -1 3.592           $ BOTTOM RIGHT SIDE OF MO
7        PX   2.54                   $ RIGHT SIDE OF MO
8        PX  -2.54                   $ LEFT SIDE OF MO
9        PZ  -2.54                   $ BOTTOM OF MO
10       PZ   2.54                   $ TOP OF MO
11       PX  -.9525                  $ LEFT OF MO BEAM HOLE
12       PX   .9525                  $ RIGHT OF MO BEAM HOLE
13       PZ  -.9525                  $ BOTTOM OF MO BEAM HOLE
14       PZ   .9525                  $ TOP OF MO BEAM HOLE
15     1 PX   0                      $ LEFT OF DETECTOR SETUP
16     2 PX   0                      $ RIGHT OF DETECTOR SETUP
17     3 PZ   0                      $ BOTTOM OF DETECTOR SETUP
18     4 PZ   0                      $ TOP OF DETECTOR SETUP
19       PX   0                      $ VERTICAL PLANE TO SEGMENT DETECTOR
20       PZ   0                      $ HORIZONTAL PLANE TO SEGMENT DETECTOR
21       PY   90.488                 $ BACK OF DETECTOR
22       PY   85.408                 $ FRONT OF DETECTOR
23       SO   200                    $ WORLD
24       PY  -14.6                   $ BACK OF GC
25       PY  -10.78                  $ FRONT OF GC
26       CY   .3175                  $ CYLINDER FOR GC
27       CZ   1.14554                $ CYLINDER OF HO
29       PZ  -1.397                  $ BOTTOM OF HO
30       PZ   1.397                  $ TOP OF HO
31       S    0 -22.83 -2.5 17.75    $ WORLD DIVISION #7
32       PY  -8.415                  $ WORLD DIVISION #8
33       CY   .42545                 $ CYLINDER FOR GOLD SLEEVE
34       PY  -10.73                  $ THICKNESS OF GOLD DISK
35       CY   .635                   $ CYLINDER FOR COPPER GC BODY
36       CY   .47625                 $ OUTER CYLINDER FOR GOLD
37       C/Z  0 -13.013 2.54         $ CYLINDER OF GC OUTER HOUSING
38       C/Z  0 -13.013 2.6162       $ 30 MILS THICK
39       PZ  -1.27                   $ BOTTOM OF OUTER HOUSING
40       PZ   1.27                   $ TOP OF OUTER HOUSING
41       PZ   .9525                  $ TOP OF GAS CELL CLAMP
42       PZ  -.9525                  $ BOTTOM OF GAS CELL CLAMP
43       PX   1.1113                 $ RIGHT OF GC CLAMP
44       PX  -1.1113                 $ LEFT OF GC CLAMP
45       PY  -13.965                 $ BACK OF GC CLAMP
46       PY  -12.06                  $ FRONT OF GC CLAMP
47       C/Z  0 -13.013 .9525        $ GC COLDFINGER CYLINDER
48       PZ  -10                     $ LENGTH OF GC COLDFINGER
49       CZ   1.4288                 $ OUTER EDGE OF HO COPPER (CU)
51       CZ   .357                   $ OUTER SHAFT OF MIDDLE OF HO CU
52       PZ   3.937                  $ BOTTOM OF TOP OF HO CU
53       CZ   1.15                   $ INSIDE OF COPPER THING
54       CZ   1.1475                 $ TALLY SURFACE #1
55       CZ   1.1485                 $ TALLY SURFACE #2
56       CZ   1.1470                 $ TALLY SURFACE #3
57       CZ   1.1480                 $ TALLY SURFACE #4
58       PY   0                      $ TALLY SURFACE #5
59       C/Z  0 -13.012 2.45         $ INNER CYLINDER
```

```
60       C/Z  0 -13.012 2.55          $ OUTER CYLINDER
61       C/Z  0 -13.012 4.00          $ FLANGE CYLINDER
62       PZ   2.76                    $ TOP OF HOUSING
63       PZ   2.65                    $ DITTO
64       PZ  -2.35                    $ FLANGE
65       PZ  -3.62                    $ FLANGE
66       PZ  -11.22                   $ BOTTOM OF HOUSING
103      PZ   19.812                  $ TOP OF CF
104      PZ   18.542                  $ BOTTOM OF TOP INSERT ON CF
105      PZ   4.572                   $ TOP OF INSERT FOR COPPER ON CF
106      PZ   2.032                   $ BOTTOM OF CF
107      CZ   0.125                   $ TOP OF CF SHAFT
108      CZ   0.24985                 $ CF SHAFT
109      CZ   2.4511                  $ INSIDE OF DRVC
110      CZ   2.54                    $ OUTSIDE OF DRVC
111      CZ   2.794                   $ INSIDE OF LHE
112      CZ   2.8575                  $ OUTSIDE OF LHE
113      CZ   3.7306                  $ INSIDE OF LN2
114      CZ   3.81                    $ OUTSIDE OF LN2
115      CZ   4.9213                  $ INSIDE OF OW
116      CZ   5.08                    $ OUTSIDE OF OW
131      PZ   23.67                   $ TOP OF TOP OF DRVC
132      PZ   23.34                   $ TOP OF DRVC
133      PZ  -5.544                   $ BOTTOM OF DRVC
134      PZ  -5.874                   $ BOTTOM OF BOTTOM OF DRVC
135      PZ  -8.414                   $ BOTTOM OF LHE
136      PZ  -8.890                   $ BOTTOM OF BOTTOM OF LHE
137      PZ   22.38                   $ TOP OF TOP OF LHE
138      PZ   21.47                   $ TOP OF LHE
139      PZ   19.53                   $ TOP OF TOP OF LN2
140      PZ   18.92                   $ TOP OF LN2
141      PZ  -10.32                   $ BOTTOM OF LN2
142      PZ  -10.95                   $ BOTTOM OF BOTTOM OF LN2
143      PZ  -11.91                   $ BOTTOM OF OW
144      PZ  -12.22                   $ BOTTOM OF BOTTOM OF OW
145      PZ   16.99                   $ TOP OF OW TOP PLATE
146      PZ   15.34                   $ TOP OF OW
147      CZ   5.24                    $ OUTER EDGE OF TOP OF DRVC
148      CZ   8.255                   $ OUTER EDGE OF TOP OF LHE
149      CZ   18.415                  $ OUTER EDGE OF TOP OF LN2
150      CZ   22.86                   $ OUTER EDGE OF TOP OF OW
151      CZ   2.55                    $ WORLD DIVISION #3
152      PZ  -6                       $ WORLD DIVISION #4
153      PZ   23.35                   $ WORLD DIVISION #5
154      PZ   23.36                   $ BOTTOM OF TOP OF DRVC MODIFIED W/ GAP
155      SY   88.0  20                $ WORLD DIVISION #6

MODE N
IMP:N 1 38R 0
M1       67165.01c   1                    $ HOLMIUM 165
M2       1001.50c  0.5238 6012.50c 0.4762 $ POLYVINYL TOLUENENE
M3       13027.50c   1                    $ ALUMINUM
M4       26000.55c 0.69  24000.50c 0.16   $ STAINLESS STEEL
         28000.50c 0.10  25055.51c 0.02   $
         42000.51c 0.02  14000.51c 0.01   $
```

```
M5      29000.50c   1                   $ COPPER
M6      79197.10C   1                   $ GOLD
C
TR1*    0.000 -20.130 0.00   3.29 86.71 90.00 93.29 3.29 90.00 90.00 90.00 0.00
TR2*    0.000 -20.130 0.00   3.29 93.29 90.00 86.71 3.29 90.00 90.00 90.00 0.00
TR3*    0.000 -20.130 0.00   0.00 90.00 90.00 90.00 3.29 93.29 90.00 86.71 3.29
TR4*    0.000 -20.130 0.00   0.00 90.00 90.00 90.00 3.29 86.71 90.00 93.29 3.29
C
SDEF   ERG=D1 POS=0 -12.69 0 CEL=1 RAD=D2 EXT=D3 AXS=0 1 0
       DIR D5 VEC 0 1 0
SI1    5 8
SP1    0 1
SI2    0.3175
SP2    -21 0
SI3    1.235
SP3    -21 0
SP5    -31 24.562
F11:N  54
FT11   INC
FU11   0 100
FC11   NEUTRONS INTO FRONT TALLY SURFACE
F21:N  30
CF21   30
FT21   INC
FU21   0 100
FC21   NEUTRONS THRU FRONT TALLY SURFACE AND INTO TOP OF HOLMIUM
F31:N  29
CF31   30
FT31   INC
FU31   0 100
FC31   NEUTRONS THRU FRONT TALLY SURFACE AND INTO BOTTOM OF HOLMIUM
F41:N  56
CF41   30
FT41   INC
FU41   0 100
FC41   NEUTRONS THRU HOLMIUM AND INTO REAR TALLY SURFACE
F51:N  56
CF51   30
FT51   INC
FU51   0 100
FC51   NEUTRONS THRU HOLMIUM OR FRONT TALLY SURFACE AND INTO REAR TALLY SURFACE
F61:N  22
CF61   30
FT61   INC
FU61   0 100
FC61   NEUTRONS THRU FRONT TALLY SURFACE AND INTO FRONT OF DETECTOR
F71:N  21
CF71   30
FT71   INC
FU71   0 100
FC71   NEUTRONS THRU FRONT TALLY SURFACE AND INTO REAR OF DETECTOR
F81:N  22
CF81   2
FT81   INC
FU81   0 100
```

```
FC81   NEUTRONS THRU HOLMIUM AND INTO FRONT OF DETECTOR
F91:N  21
CF91   2
FT91   INC
FU91   0 100
FC91   NEUTRONS THRU HOLMIUM AND INTO REAR OF DETECTOR
F101:N 22
CF101  31
FT101  INC
FU101  0 100
FC101  NEUTRONS THRU REAR TALLY SURFACE AND INTO FRONT OF DETECTOR
F111:N 21
CF111  31
FT111  INC
FU111  0 100
FC111  NEUTRONS THRU REAR TALLY SURFACE AND INTO REAR OF DETECTOR
F121:N 22
CF121  30 2
FT121  INC
FU121  0 100
FC121  NEUTRONS THRU FRONT TALLY SURFACE OR HO AND INTO FRONT OF DETECTOR
F131:N 21
CF131  30 2
FT131  INC
FU131  0 100
FC131  NEUTRONS THRU FRONT TALLY SURFACE OR HO AND INTO REAR OF DETECTOR
F141:N 22
CF141  31 2
FT141  INC
FU141  0 100
FC141  NEUTRONS THRU HO OR REAR TALLY SURFACE AND INTO FRONT OF DETECTOR
F151:N 21
CF151  31 2
FT151  INC
FU151  0 100
FC151  NEUTRONS THRU HO OR REAR TALLY SURFACE AND INTO REAR OF DETECTOR
F161:N 22
CF161  30 31
FT161  INC
FU161  0 100
FC161  NEUTRONS THRU FRONT OR REAR TALLY SURFACE AND INTO FRONT OF DETECTOR
F171:N 21
CF171  30 31
FT171  INC
FU171  0 100
FC171  NEUTRONS THRU FRONT OR REAR TALLY SURFACE AND INTO REAR OF DETECTOR
F181:N 22
CF181  30 31 2
FT181  INC
FU181  0 100
FC181  NEUTRONS THRU HO OR FRONT OR REAR TALLY AND INTO FRONT OF DETECTOR
F191:N 21
CF191  30 31 2
FT191  INC
FU191  0 100
```

```
FC191  NEUTRONS THRU HO OR FRONT OR REAR TALLY AND INTO REAR OF DETECTOR
PHYS:N 25
CUT:N  J 1.5 3J
C
NPS    100000
PRINT  126
DBCN   1376393645937
```

Appendix C

Electronic Schematics

Schematics for equipment designed and built for this experiment are archived in this Appendix. Figures C.1 and C.2 are the schematics for the photomultiplier tube bases for both the 0° and monitor detectors. The voltage distributions for both sets of detectors are given in Tables C.1 and C.2. Figure C.3 is the schematic for the spin-state controller used to flip the neutron spin every 100 ms in the eight-step sequence $+\ -\ -\ +\ -\ +\ +\ -$. Figures C.4 and C.5 are schematics for the vetoing circuit. Figure C.6 is the schematic for the 50 MHz pulser used to test the stability of the vetoing circuit. And lastly, Figures C.7 and C.8 are the schematics for the beam current integrator.

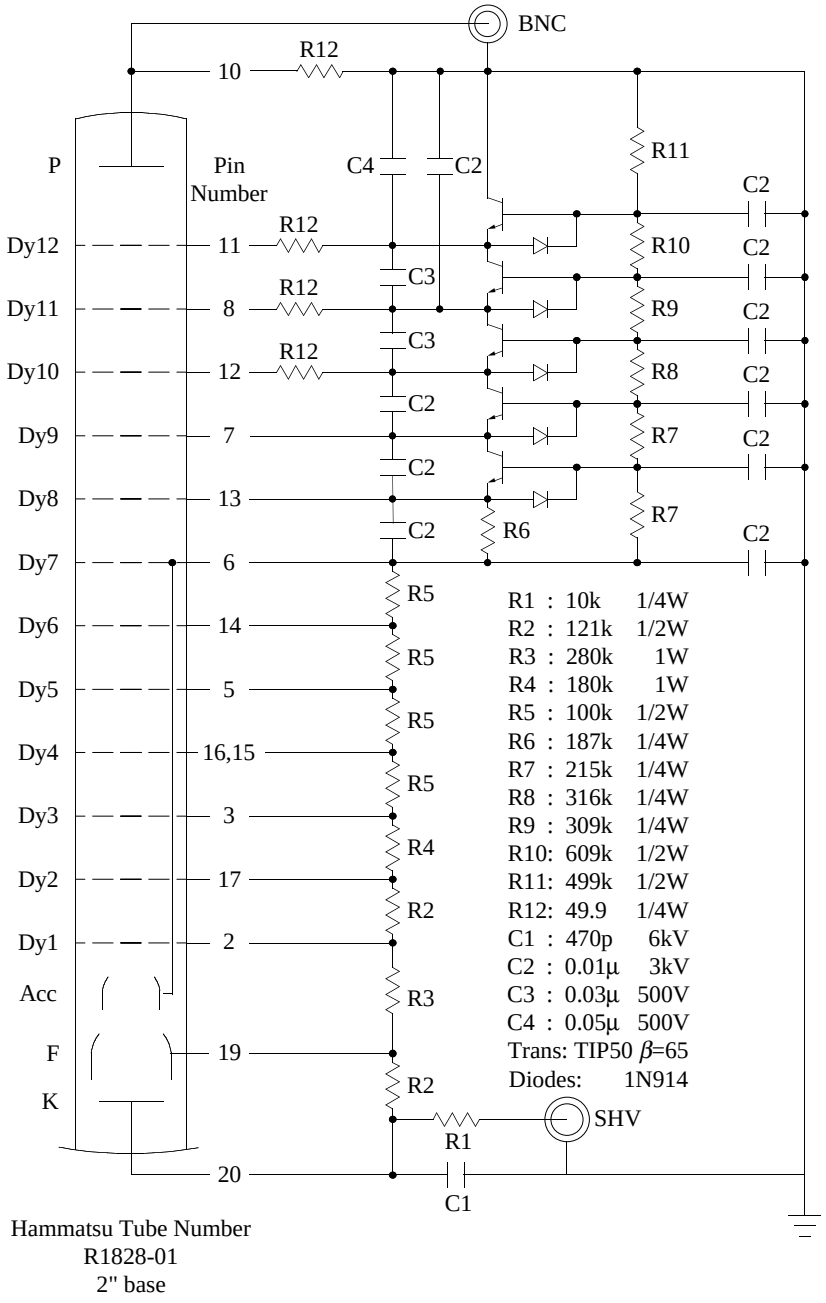

Figure C.1: Schematic for 0° detector photomultiplier tube voltage divider circuit.

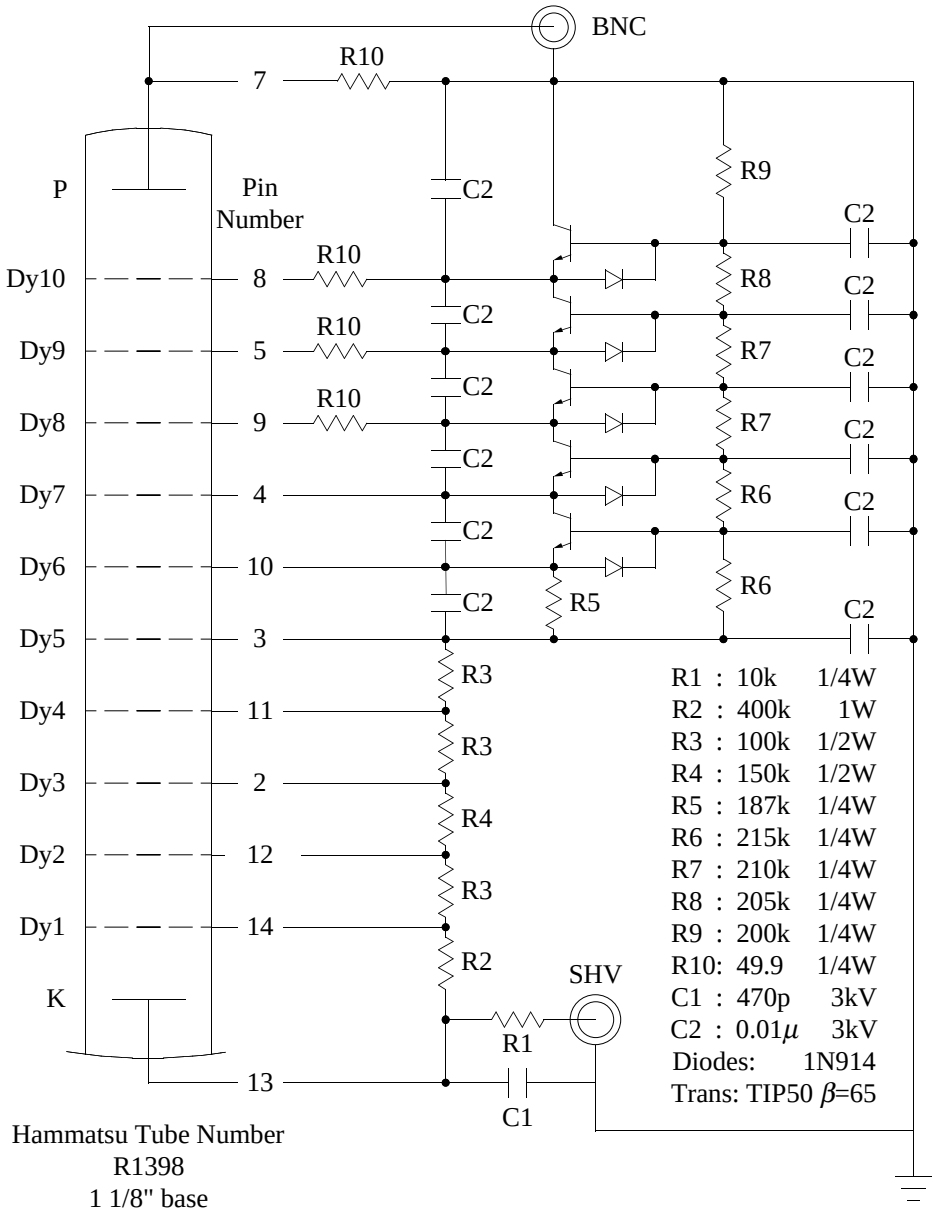

Figure C.2: Schematic for the monitor detector photomultiplier tube voltage divider circuit.

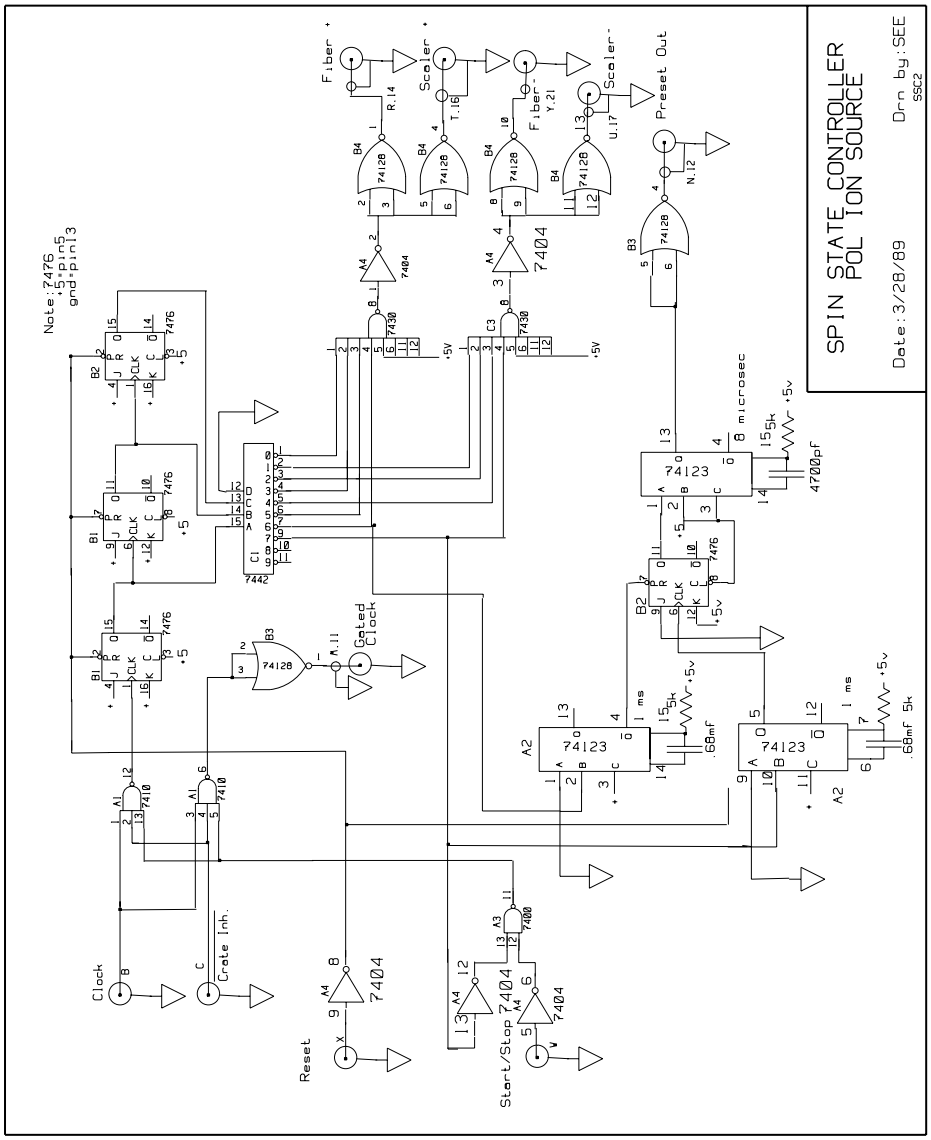

Figure C.3: Schematic of the polarized ion source spin-state controller. This module generates the eight-step spin sequence $+\ -\ -\ +\ -\ +\ +\ -$ used to toggle the spin-state of the beam.

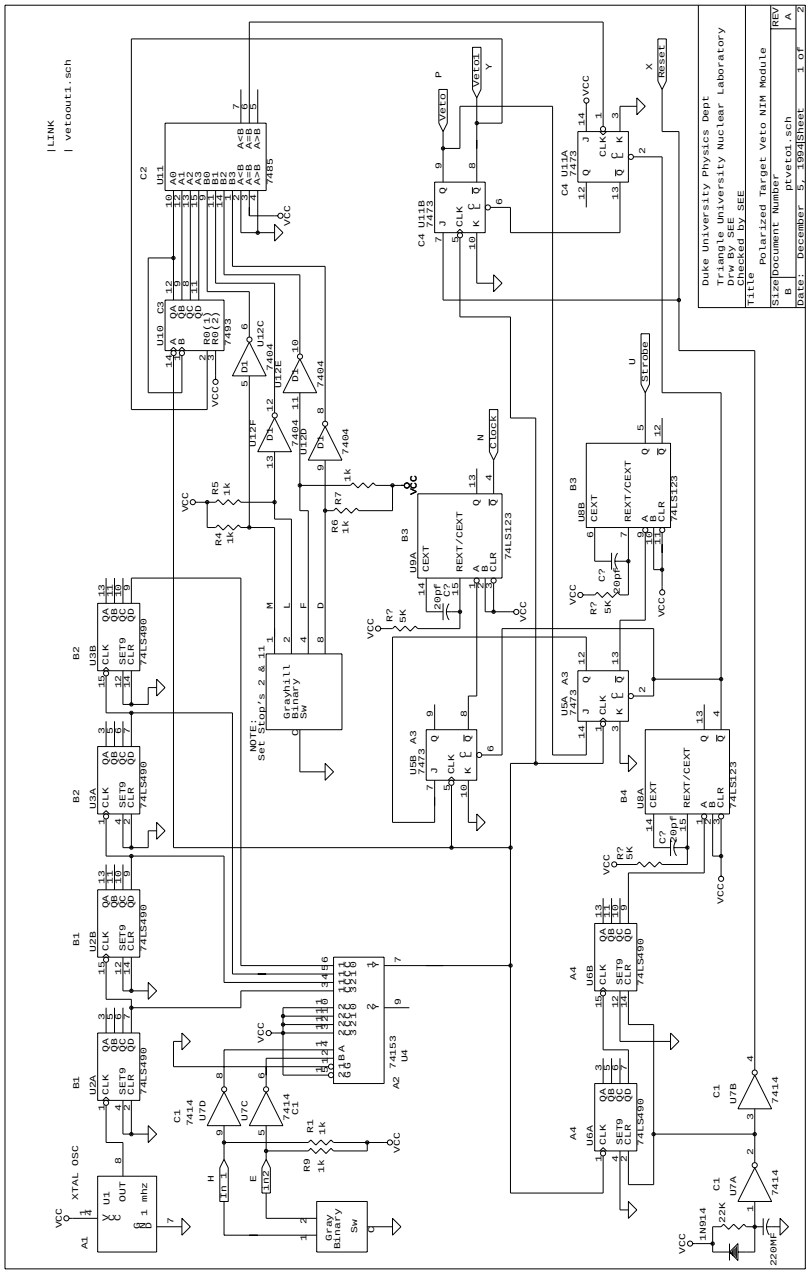

Figure C.4: Schematic of the polarized target veto module (part 1). This module generates the clock signal used to drive the spin-state controller, generates a strobe pulse to signal reading of the scalars during the spin-flip, and generates a veto signal to inhibit the scalars during the spin-flip.

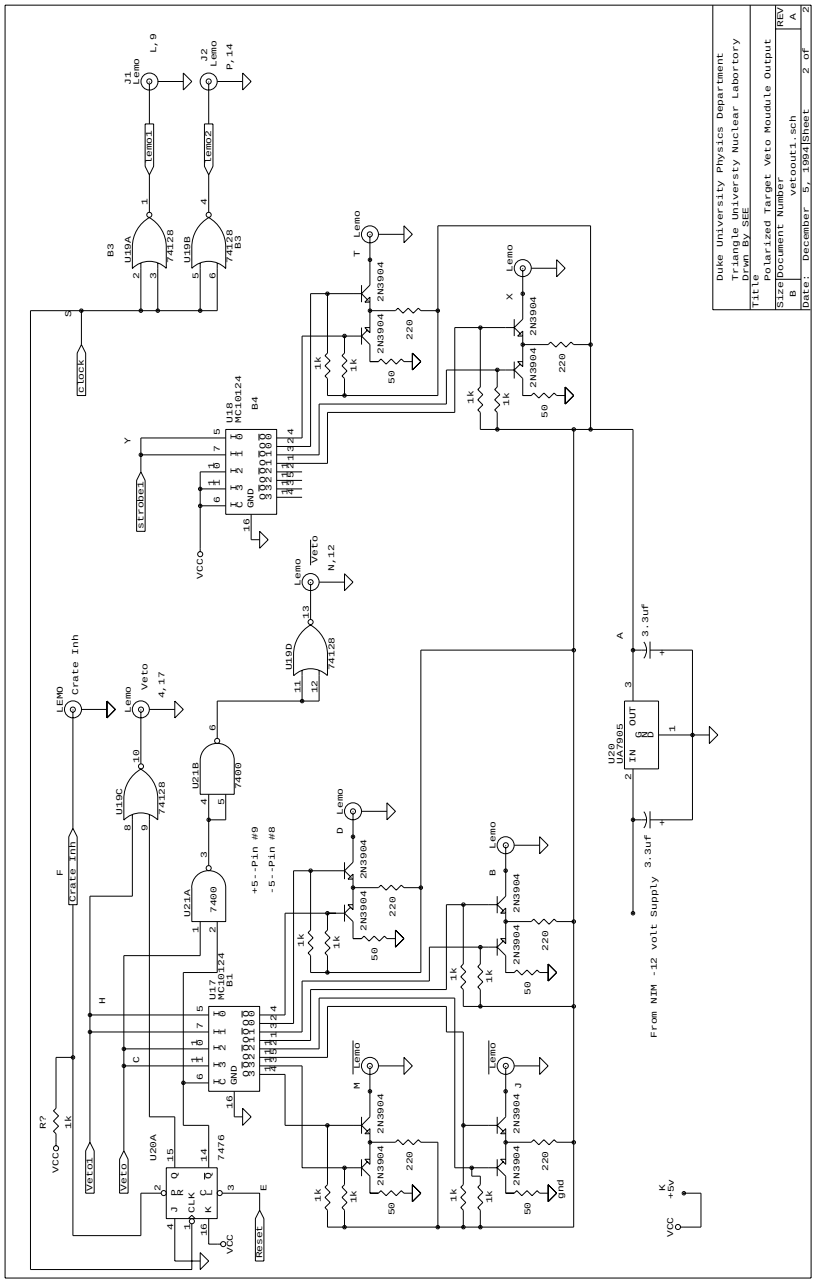

Figure C.5: Schematic of the polarized target veto module (part 2). This module generates the clock signal used to drive the spin-state controller, generates a strobe pulse to signal reading of the scalars during the spin-flip, and generates a veto signal to inhibit the scalars during the spin-flip.

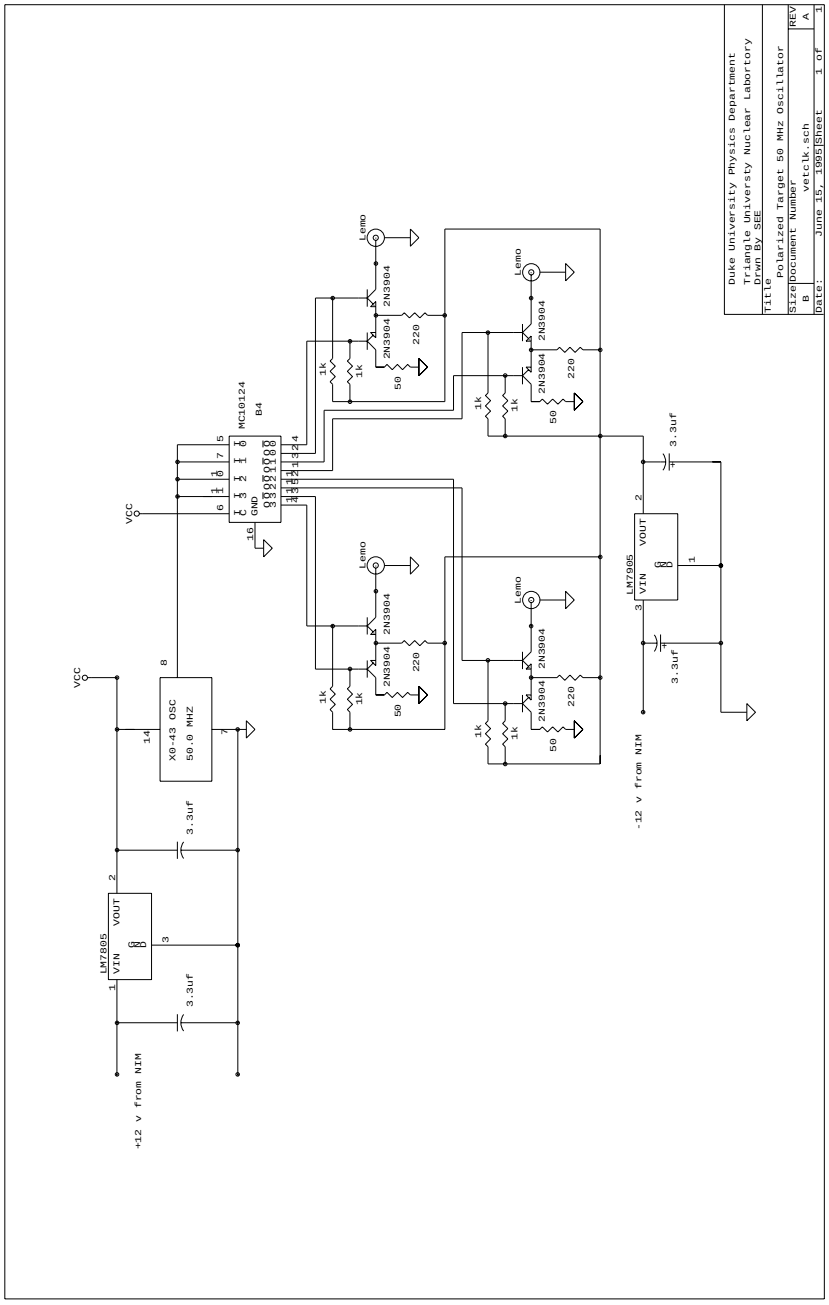

Figure C.6: Schematic of the 50 MHz pulser used for vetoing and stability tests.

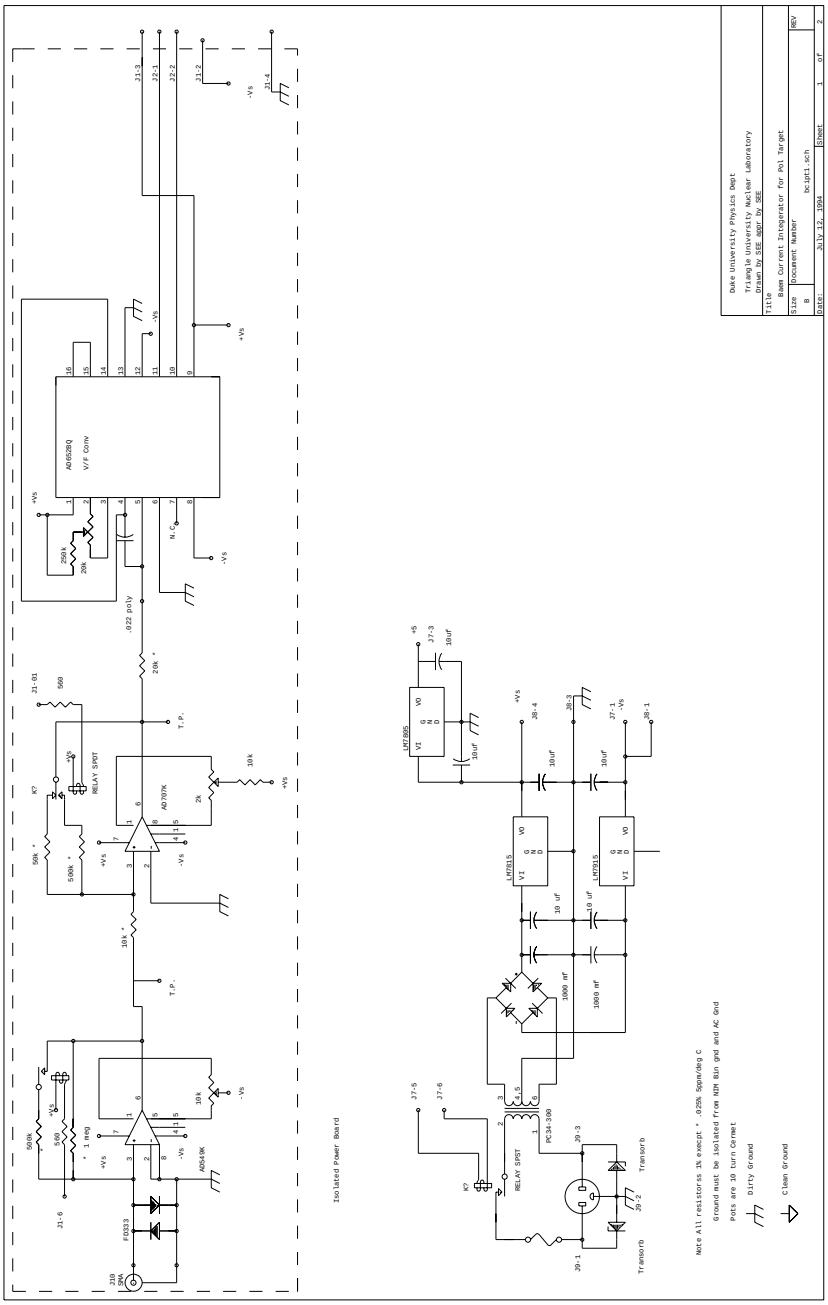

Figure C.7: Schematic of the beam current integrator circuit (part 1).

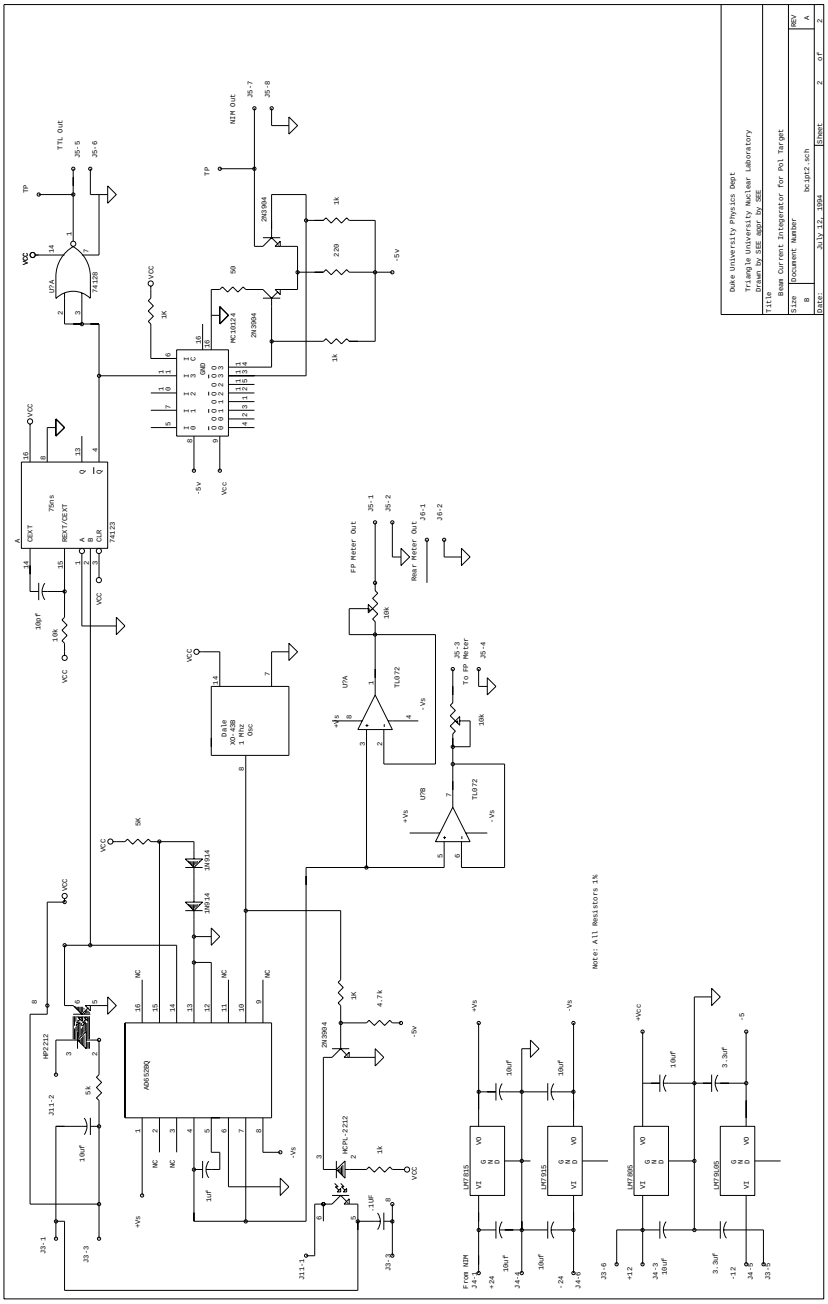

Figure C.8: Schematic of the beam current integrator circuit (part 2).

Dynode Number	Pin Number	Top Left	Top Right	Bottom Right	Bottom Left
K	20	-2517	-2517	-2518	-2517
F	19	-2373	-2373	-2373	-2372
1	2	-2034	-2031	-2033	-2039
2	17	-1982	-1889	-1891	-1896
3	3	-1693	-1690	-1692	-1697
4	16,15	-1576	-1574	-1575	-1579
5	5	-1460	-1457	-1459	-1463
6	14	-1344	-1342	-1343	-1346
7	6	-1228	-1226	-1227	-1231
8	13	-1120	-1117	-1118	-1121
9	7	-1000	-999	-999	-1003
10	12	-822	-821	-823	-825
11	8	-646	-645	-646	-648
12	11	-292	-293	-293	-294
P	10	0	0	0	0

Table C.1: The voltage distributions of each of the 0° detector phototube bases for a fixed input voltage.

Dynode Number	Pin Number	Top Left	Top Right	Bottom Right	Bottom Left
K	13	-2014	-2015	-2013	-2014
1	14	-1462	-1465	-1464	-1465
2	12	-1323	-1326	-1324	-1327
3	2	-1115	-1117	-1116	-1119
4	11	-977	-978	-978	-981
5	3	-839	-840	-840	-843
6	10	-704	-704	-705	-708
7	4	-562	-563	-563	-566
8	9	-422	-423	-423	-425
9	5	-280	-281	-281	-282
10	8	-140	-140	-140	-140
P	7	0	0	0	0

Table C.2: The voltage distributions of each of the monitor detector phototube bases for a fixed input voltage.

Appendix D

Beam Heating Effects

The 6 MeV polarized neutron beam used in this experiment is produced using a 3 MeV polarized deuteron beam and the $^2\mathrm{H}(\vec{\mathrm{d}},\vec{\mathrm{n}})^3\mathrm{He}$ reaction. The deuteron beam is incident upon a cryogenically cooled deuterium gas cell and is stopped upon exit of the cell with a gold foil. The 2 μA of beam can deposit up to 6 W of heat into the cell. This heat can cause large variations in the temperature of the cell, and thus large fluctuations in the density of the gas within the cell.

The deposited heat is removed from the cell by a copper coldfinger extending into a liquid nitrogen bath. Once the beam is placed on the cell, thermal equilibrium is reached in about one hour, with a temperature rise of 80 K occurring. These temperature variations occur on the same time scale as a rotation sequence of the target and thus can contribute time-dependent terms to the normalized asymmetry. In the time-reversal measurement, effects arising from temperature variations are suppressed by controlling the temperature of the gas cell and normalizing the neutron flux. However, in the initial stages of this experiment, temperature stabilization of the gas cell was not performed and the resulting drifts in both the yields and asymmetries are discussed in this appendix.

The neutron yields can be normalized to either the number of counts from the beam current integration or the number of counts in the monitor detector array. The monitor normalization is superior because it suppresses most of the fluctuations in the neutron flux,

whereas the beam current normalization only suppresses fluctuations in the intensity of the deuterium beam. Thus, the beam current normalization fails to remove any effects related to either changes in the gas cell or in the tensor polarization of the beam. When investigating effects that arise from the gas cell, however, beam current normalization will maximize these effects and thus will be used in the initial discussion of beam heating effects.

When the deuteron beam is placed on the gas cell, the temperature in the gas cell rises, resulting in a decrease in the density of the gas within the cell. The product of density and thickness ρt decreases and thus the neutron flux decreases given a constant beam current. The decrease in flux will appear as an exponential decay in the yield for both spin-states with a time constant equal to the thermal time constant for the cooling system of the cell. Such an effect in the yield has been observed and the yield for the two spin-states is shown in Figure D.1 for two detectors. The vertical axis represents the beam current normalized yield and the horizontal axis represents the run number or angular sequence. Each run corresponds to approximately four minutes worth of data taken in the angular sequence $-180°, \ldots, -22.5°, 0°, 22.5°, \ldots, +180°, \ldots, -180°$. Beam was placed onto the cold ($\sim$ 86 K) gas cell at run number 7479. The beam heating caused the neutron yield to exponentially decrease until thermal equilibrium ($\sim$ 168 K) was reached around run number 7530. The time constant for this decay is roughly 30 minutes.

An asymmetry is formed between the two yields and is shown in Figure D.2 for both a left and right detector with respect to the beam direction. The time drifts in the asymmetry are due to the failure of the eight-step sequence in removing polarization dependent terms in the yield (discussed further in Appendix E). These terms arise from the unequal tensor polarizations in the deuteron beam and result in a constant offset in the asymmetry. Both the vector and tensor analyzing powers contribute to the offset in the asymmetry in the individual detectors. But when combined to form an average asymmetry, the offsets from the vector analyzing power cancel, leaving only the tensor analyzing power to contribute.

Evidence for beam effects in the asymmetry from the exponential changes in the

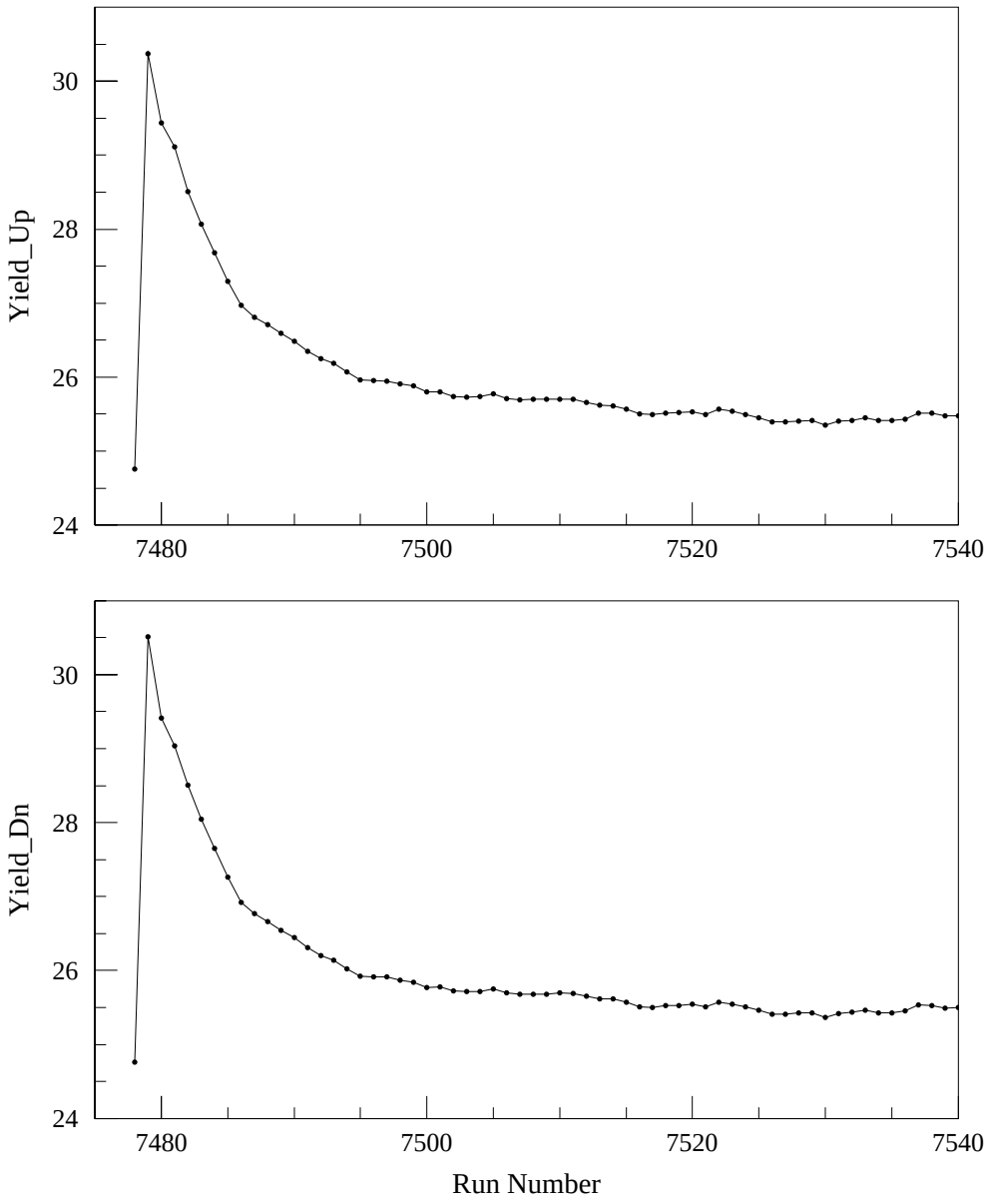

Figure D.1: Effects of beam heating in the beam current normalized yield. The two graphs represent the yield for the two neutron spin-states (arbitrary units) as a function of run number or angular sequence.

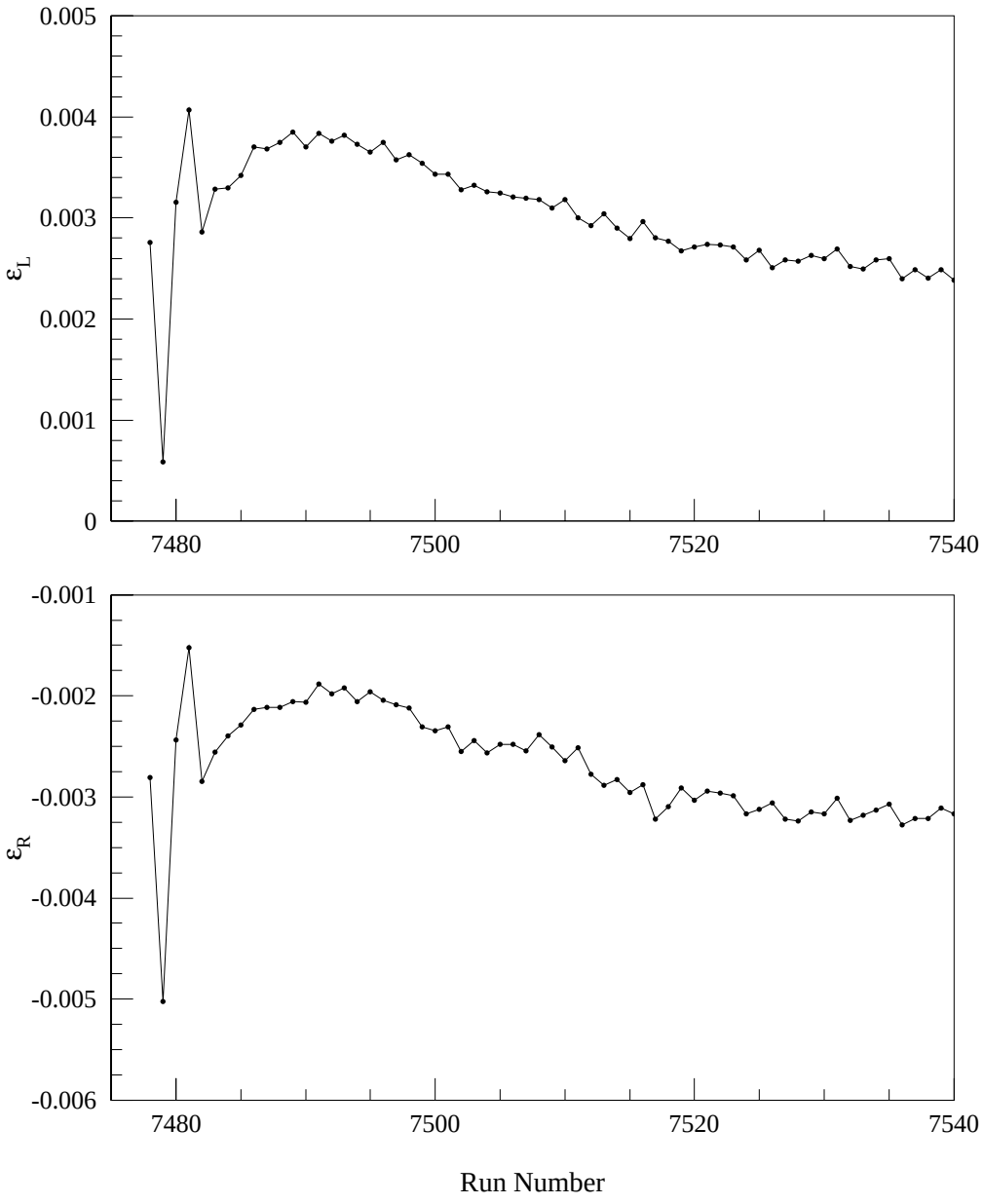

Figure D.2: Effects of beam heating in the beam current normalized asymmetry. The upper graph depicts the asymmetry in a left detector with respect to the beam direction and the lower graph depicts the asymmetry in a right detector.

yield appears as drifts in the asymmetries in the individual detectors. The effects could arise from either vector or tensor analyzing power terms, but by comparing the detector asymmetries for the individual left and right detectors, the effect can clearly be contributed to arising from tensor analyzing power terms as will be discussed below.

Using the asymmetries shown in Figure D.2, the constant offset in the left detector is of opposite sign to the offset in the right detector, whereas the effects from beam heating contribute with the same sign. The nature of this sign difference can be explained using a model in which the neutron flux consists of a constant term with an exponential decay in time superimposed, taking the form

$$I \propto 1 + \alpha e^{-\omega t}. \tag{D.1}$$

A fit to the actual yields confirms a time dependence of this form, and this dependence is then combined with the flux from the neutron production reaction at a small angle ϕ yielding

$$I^{\pm}(\phi) = I_0^{\pm}\left(1 \pm \frac{3}{2}P_z^{\pm}A_y(\phi) + \frac{1}{4}P_{zz}^{\pm}A_{zz}(\phi)\right)\left(1 + \alpha e^{-\omega t}\right), \tag{D.2}$$

where $A_y(\phi)$ and $A_{zz}(\phi)$ are the vector and tensor analyzing powers for the reaction and P_z and P_{zz} are the vector and tensor polarizations of the deuteron beam. Noting that the tensor analyzing power is symmetric about 0° ($A_{zz}(\phi) = A_{zz}(-\phi)$) while the vector analyzing power is antisymmetric ($A_y(\phi) = -A_y(-\phi)$), the asymmetry for either the left (L) or right (R) detector is given by[1]

$$\mathcal{E}_{L/R} = \pm\frac{3}{4}\left(P_z^{+} + P_z^{-}\right)|A_y(\phi)|\left(1 + \alpha e^{-\omega t}\right) + \frac{1}{8}\left(P_{zz}^{+} - P_{zz}^{-}\right)A_{zz}(\phi)\left(1 + \alpha e^{-\omega t}\right). \tag{D.3}$$

The component of the asymmetry due to vector analyzing power effects reverses sign between the left and right detectors while the component arising from tensor analyzing power effects will remain the same sign. Thus since the beam heating effects in the asymmetry do not change sign for the left and right detectors, they must arise from tensor analyzing power effects not removed by the eight-step neutron spin sequence. The failure of the eight-step sequence in removing this term is discussed further in Appendix E.

[1]Note that for simplicity, equal incident beam currents for the two spin-states are assumed (ie. $I_0^{+} = I_0^{-}$).

Normalization to the monitor detector counts greatly reduces beam heating effects. This reduction can be quantified by comparing the asymmetries using the two normalizations. Figure D.3 shows both the monitor normalized yield and the monitor normalized asymmetry for the data shown in Figures D.1 and D.2. The drifts in the beam current normalized data are suppressed but are still present in the monitor normalized data. A polynomial fit to the asymmetry can be performed on both the beam current normalized and monitor normalized asymmetries to extract the linear and quadratic time dependences. A ratio formed either between the linear or quadratic terms for the two fits will give the suppression factor for time dependent drifts from normalization to the monitor. A fit to the asymmetry in each detector was performed and the ratio of fitting coefficients gave a factor of 12 suppression in each case. The monitor normalization thus suppresses both linear and quadratic time dependent effects by an order of magnitude.

During the time-reversal measurement, the temperature of the gas cell is controlled to within 0.5 K during collection of the data. Controlling the temperature thus reduces these fluctuations two orders of magnitude ($\sim 0.5/80 = 160$). A fit to the beam current normalized asymmetry yields a linear drift of $\sim 5 \times 10^{-3}$ over a sixteen run sequence. This implies a linear contribution in the time reversal data of at most $\lesssim 3 \times 10^{-6}$ when both the temperature of the gas cell is controlled and the data is normalized to the counts in the monitor detector array. The linear term is further removed by the rotation sequence of the target (Appendix E), leaving the lowest order contribution to the asymmetry arising from the quadratic time dependence. The quadratic term in the above fit is $\sim 5 \times 10^{-4}$, implying the lowest order contribution to the the time reversal asymmetry from beam heating effects is $\lesssim 3 \times 10^{-7}$, well below the limits set by the present measurement.

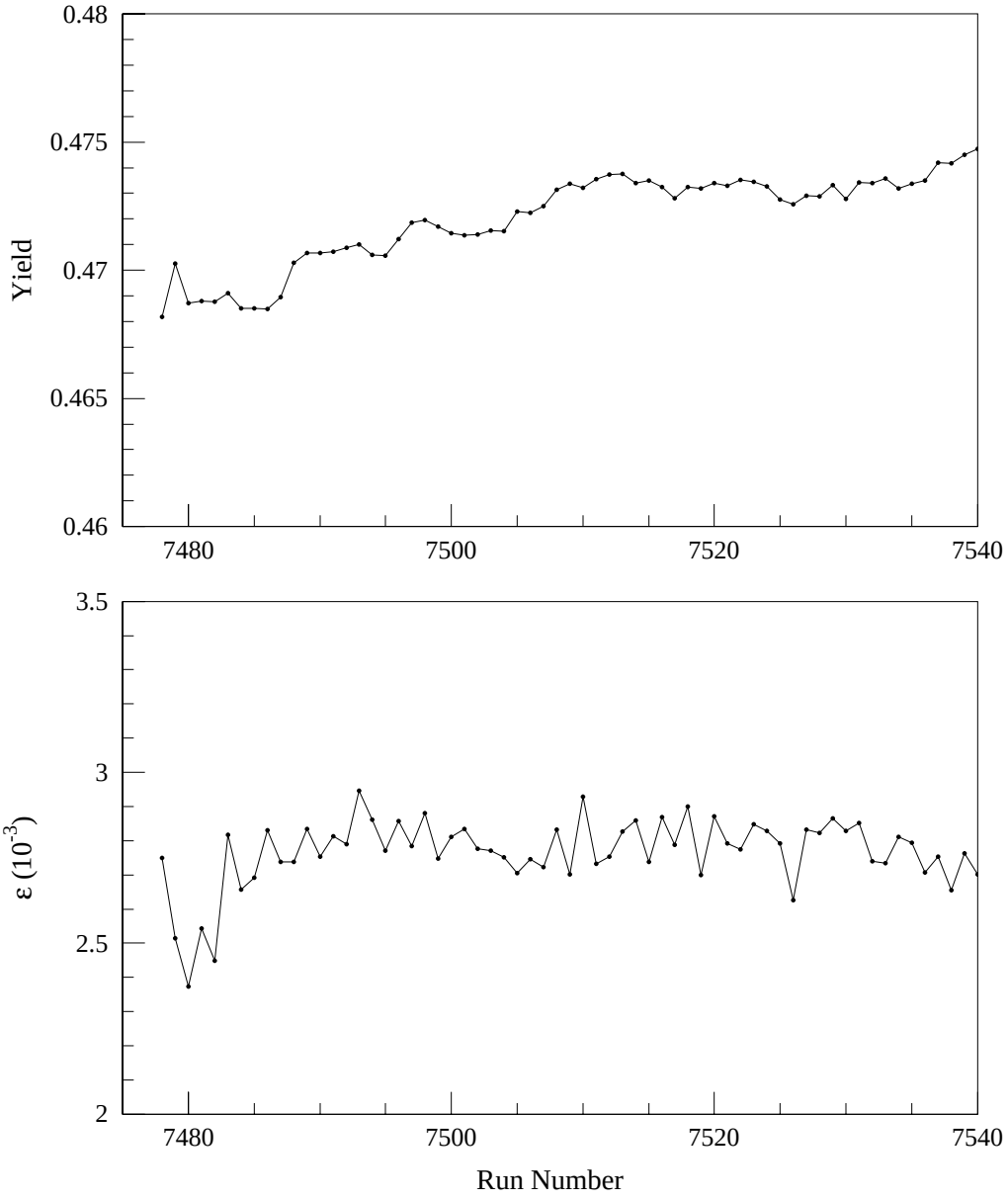

Figure D.3: Effects of beam heating in the monitor normalized yield and asymmetry. The upper graph corresponds to the transmission yield for one of the two spin-states. The lower graph corresponds to the asymmetry formed between the yields for the two neutron spin-states.

Appendix E

Spin Sequence and Target Rotation

The eight-step neutron spin-state sequence $+--+-+++-$ is utilized to remove both linear and quadratic drifts in the detector asymmetry. The rotation sequence of the target further removes linear drifts arising in the normalized asymmetry. This appendix serves to formalize the eight-step sequence and set limits on contributions from polarization dependent and polarization independent non-statistical fluctuations. The mathematical formalism for the target rotation sequence and the removal of particular components in the asymmetry are also discussed.

E.1 Eight-Step Neutron Spin Sequence

The eight-step neutron spin sequence $+--+-+++-$ has been used for a number of years to minimize both linear and quadratic drifts in an asymmetry formed between the two spin-states [Kos90, Rob93]. In past discussions, the transmission for the two spin-states was assumed to be independent of the two polarization states. This however, is not true for the present experiment and thus requires a formal treatment that includes polarization dependent effects.

The previous derivations assumed that the normalized yields for the two polarization states are equal. Following the notation of Koster [Kos90], the normalized detector

asymmetry is formed by taking the difference in transmission yields between neutrons with spin-up (+) and spin-down (−). Denoting the normalized yield as a function of time as $\tilde{N}^{\pm}(t)$, the time spent in each spin-state as Δ, and assuming $\tilde{N}^{+}(t) = \tilde{N}^{-}(t) = \tilde{N}(t)$, the detector asymmetry, $\mathcal{E}_i$, for a single eight-step sequence is given by

$$\mathcal{E}_i = \frac{F_{0,1} - F_{1,2} - F_{2,3} + F_{3,4} - F_{4,5} + F_{5,6} + F_{6,7} - F_{7,8}}{F_{0,8}}, \tag{E.1}$$

where

$$F_{a,b} = \int_{t_i+a\Delta}^{t_i+b\Delta} \tilde{N}(t)\, dt. \tag{E.2}$$

The yield $\tilde{N}(t)$ is slowly varying over the 800 ms interval of the spin-flip sequence ($t_i \rightarrow t_i + 8\Delta$) and can be expressed in a power series expansion in time:

$$\tilde{N}(t) = \sum_{m=0}^{\infty} a_m\, t^m. \tag{E.3}$$

Inserting this expansion into the integral expression above gives,

$$F_{a,b} = \int_{t_i+a\Delta}^{t_i+b\Delta} \tilde{N}(t)\, dt = \sum_{m=0}^{\infty} \frac{a_m}{m+1} \left[(t_i + b\Delta)^{m+1} - (t_i + a\Delta)^{m+1} \right]. \tag{E.4}$$

The Taylor Series expansion

$$f(t_i + a\Delta) = \sum_{n=0}^{\infty} \frac{(a\Delta)^n}{n!} \frac{\mathrm{d}^n}{\mathrm{d}{t_i}^n} f(t_i) \tag{E.5}$$

can be used with

$$f(t_i) = \sum_{m=0}^{\infty} \frac{a_m}{m+1}\, t_i^{m+1} \tag{E.6}$$

to rewrite the integral expression as

$$\begin{aligned} \int_{t_i+a\Delta}^{t_i+b\Delta} \tilde{N}(t)\, dt &= f(t_i + b\Delta) - f(t_i + a\Delta) \\ &= \sum_{n=0}^{\infty} (b^n - a^n) \frac{\Delta^n}{n!} \frac{\mathrm{d}^n}{\mathrm{d}{t_i}^n} f(t_i). \end{aligned} \tag{E.7}$$

After inserting this expression into the detector asymmetry (Equation E.1), the asymmetry for an individual eight-step sequence is given by

$$\mathcal{E}_i = \frac{\sum_{n=0}^{\infty} \phi_n \frac{\Delta^n}{n!} \frac{\mathrm{d}^n}{\mathrm{d}{t_i}^n} f(t_i)}{\sum_{n=0}^{\infty} (8^n - 0^n) \frac{\Delta^n}{n!} \frac{\mathrm{d}^n}{\mathrm{d}{t_i}^n} f(t_i)}, \tag{E.8}$$

where

$$\begin{aligned}\phi_n &= [(1^n - 0^n) - (2^n - 1^n) - (3^n - 2^n) + (4^n - 3^n) \\ &\quad - (5^n - 4^n) + (6^n - 5^n) + (7^n - 6^n) - (8^n - 7^n)]\,. \end{aligned} \tag{E.9}$$

The lowest order non-zero term in this expansion is $n = 4$. Noting that $\tilde{N}(t_i) \equiv \frac{\mathrm{d}}{\mathrm{d}t_i} f(t_i)$, the detector asymmetry $\mathcal{E}_i$ to lowest order in delta is

$$\mathcal{E}_i = \frac{-\Delta^3 \frac{\mathrm{d}^3}{\mathrm{d}{t_i}^3}\tilde{N}(t_i)}{\tilde{N}(t_i) + 4\Delta\frac{\mathrm{d}}{\mathrm{d}t_i}\tilde{N}(t_i) + \frac{32}{3}\Delta^2\frac{\mathrm{d}^2}{\mathrm{d}{t_i}^2}\tilde{N}(t_i) + \frac{64}{3}\Delta^3\frac{\mathrm{d}^3}{\mathrm{d}{t_i}^3}\tilde{N}(t_i)} \tag{E.10}$$

or

$$\mathcal{E}_i \approx -\frac{\Delta^3}{\tilde{N}(t_i)}\frac{\mathrm{d}^3}{\mathrm{d}{t_i}^3}\tilde{N}(t_i). \tag{E.11}$$

This expression has previously been derived by both Koster [Kos90] and Roberson *et al.* [Rob93].

Contributions from this term to the measured asymmetry can be estimated using $\Delta = 100$ ms, $\tilde{N}(t_i) \sim 10^6$, and $\frac{\mathrm{d}^3}{\mathrm{d}{t_i}^3}\tilde{N}(t_i) \sim 1$. Terms appearing in the asymmetry from the third order time derivative of the yield are thus less than $\sim 10^{-9}$, well below the limits of the present measurement. In practice, the normalized yield can be fit using a least squares polynomial fitting routine supplied by the statistical package JMP [JMP94]. A fit to the normalized yield gives a value of $\frac{1}{\tilde{N}(t_i)}\frac{\mathrm{d}^3}{\mathrm{d}{t_i}^3}\tilde{N}(t_i) \sim 10^{-12}$. Thus contributions to the measured asymmetry from spin independent parameters are negligible.

The above derivation is based on the assumption that $\tilde{N}^+(t) = \tilde{N}^-(t)$, which holds true for spin independent parameters such as phototube bias changes and beam current fluctuations. Spin dependent terms, however, bring about new complications and ultimately lead to components in the asymmetry larger than third order in time as discussed above.

The deuteron beam intensity is polarization dependent because the two polarization states are created using independent RF cavities within the polarized ion source (Section 3.2.1). The beam has both vector and tensor polarizations, and the magnitude of these polarizations differ for each state. Since the 0° neutron flux is proportional to both the

incident deuteron flux and its tensor polarization, the effects of independent neutron fluxes on the normalized asymmetry for the two polarization states must be considered.

The detector asymmetry for two independent neutron fluxes is modeled using a similar notation as above, except the neutron flux now contains a polarization dependent term:

$$\tilde{N}^{\pm}(t) = \tilde{N}(t)(1 + \delta^{\pm}(t)). \tag{E.12}$$

A similar expression for the asymmetry $\mathcal{E}_i$ is given by

$$\mathcal{E}_i = \mathcal{E}_i^1 + \mathcal{E}_i^2, \tag{E.13}$$

where

$$\mathcal{E}_i^1 = \frac{F_{0,1} - F_{1,3} + F_{3,4} - F_{4,5} + F_{5,7} - F_{7,8}}{F_{0,8} + G_{0,1}^{+} + G_{1,3}^{-} + G_{3,4}^{+} + G_{4,5}^{-} + G_{5,7}^{+} + G_{7,8}^{-}} \tag{E.14}$$

and

$$\mathcal{E}_i^2 = \frac{G_{0,1}^{+} - G_{1,3}^{-} + G_{3,4}^{+} - G_{4,5}^{-} + G_{5,7}^{+} - G_{7,8}^{-}}{F_{0,8} + G_{0,1}^{+} + G_{1,3}^{-} + G_{3,4}^{+} + G_{4,5}^{-} + G_{5,7}^{+} + G_{7,8}^{-}}, \tag{E.15}$$

with

$$F_{a,b} = \int_{t_i + a\Delta}^{t_i + b\Delta} \tilde{N}(t)\, dt \quad \text{and} \quad G_{a,b}^{\pm} = \int_{t_i + a\Delta}^{t_i + b\Delta} \delta^{\pm}(t)\tilde{N}(t)\, dt. \tag{E.16}$$

Performing a similar derivation as in the spin independent case above, power series expansions given by Equation E.3 and

$$\delta^{\pm}(t)\tilde{N}(t) = \sum_{m=0}^{\infty} a_m^{\pm} t^m \tag{E.17}$$

are used to express the detector asymmetry for an individual eight-step spin sequence:

$$\mathcal{E}_i = \frac{\displaystyle\sum_{n=0}^{\infty} \frac{\Delta^n}{n!} \frac{\mathrm{d}^{n-1}}{\mathrm{d}{t_i}^{n-1}} \left(\phi_n + \beta_n(t_i)\right) \tilde{N}(t_i)}{\displaystyle\sum_{n=0}^{\infty} \frac{\Delta^n}{n!} \frac{\mathrm{d}^{n-1}}{\mathrm{d}{t_i}^{n-1}} \left[(8^n - 0^n) + \alpha_n(t_i)\right] \tilde{N}(t_i)} \tag{E.18}$$

where ϕ_n is given by Equation E.9,

$$\begin{aligned} \alpha_n(t_i) \;\; = \;\; & \left[(7^n - 5^n + 4^n - 3^n + 1^n - 0^n)\, \delta^{+}(t_i)\right. \\ & \left. + (8^n - 7^n + 5^n - 4^n + 3^n - 1^n)\, \delta^{-}(t_i)\right], \end{aligned} \tag{E.19}$$

and

$$\begin{aligned}\beta_n(t_i) &= \left[\left(7^n - 5^n + 4^n - 3^n + 1^n - 0^n\right)\delta^+(t_i)\right. \\ &\quad \left. - \left(8^n - 7^n + 5^n - 4^n + 3^n - 1^n\right)\delta^-(t_i)\right]. \end{aligned} \tag{E.20}$$

The asymmetry to second order in time ($\mathcal{O}(\Delta^2)$) for an individual eight-step sequence is

$$\mathcal{E}_i = \frac{\epsilon^- \tilde{N}(t_i) + 4\Delta\frac{\mathrm{d}}{\mathrm{d}t_i}\epsilon^- \tilde{N}(t_i) + \frac{32}{3}\Delta^2\frac{\mathrm{d}^2}{\mathrm{d}{t_i}^2}\epsilon^- \tilde{N}(t_i)}{(2+\epsilon^+)\tilde{N}(t_i) + 4\Delta\frac{\mathrm{d}}{\mathrm{d}t_i}(2+\epsilon^+)\tilde{N}(t_i) + \frac{32}{3}\Delta^2\frac{\mathrm{d}^2}{\mathrm{d}{t_i}^2}(2+\epsilon^+)\tilde{N}(t_i)} \tag{E.21}$$

or

$$\mathcal{E}_i \approx \frac{1}{2}\epsilon^- + 2\frac{\Delta}{\tilde{N}(t_i)}\frac{\mathrm{d}}{\mathrm{d}t_i}\epsilon^- \tilde{N}(t_i) + \frac{16}{3}\frac{\Delta^2}{\tilde{N}(t_i)}\frac{\mathrm{d}^2}{\mathrm{d}{t_i}^2}\epsilon^- \tilde{N}(t_i), \tag{E.22}$$

where

$$\epsilon^{\pm} = \delta^+(t_i) \pm \delta^-(t_i). \tag{E.23}$$

Note the difference between this expression and the one given in Equation E.11. This expression contains a constant, linear, and quadratic term in time. The linear and quadratic terms can contribute to a $\sin 2\theta$ component in the asymmetry since the angular rotation sequence is correlated with time.

Ideally, the flux normalization using the monitor detector array will remove these spin dependent terms, leaving the lowest order contribution arising from the third order time dependence given by Equation E.11. In practice however, these terms are suppressed but not eliminated, resulting in both a non-zero constant offset and time dependent terms in the asymmetry. The constant term does not present a problem, since it is orthogonal to the $\sin 2\theta$ term of interest, but the time dependent terms can present a problem and must be investigated further.

The constant term in Equation E.22 arises from the unequal tensor polarizations of the incident deuteron beam, causing a difference in the neutron flux for the two polarization states. The monitor normalization should remove these effects, but because it subtends a different solid angle than the 0° detectors, it measures a different tensor analyzing power for the reaction and thus fails to completely remove the constant offset. As discussed in

Appendix D, the monitor normalization does however reduce the asymmetry by more than an order of magnitude and thus similarly reduces the time dependent effects. The large constant offset does not directly present a problem, but linear and quadratic time drifts in this offset can. Contributions from these drifts in time are considered below.

The term linear in time in Equation E.22 consists of two contributing parts:

$$\mathcal{E}_i \sim 2\Delta\frac{\mathrm{d}}{\mathrm{d}t_i}\epsilon^- + 2\Delta\frac{\epsilon^-}{\tilde{N}(t_i)}\frac{\mathrm{d}}{\mathrm{d}t_i}\tilde{N}(t_i). \tag{E.24}$$

The first term involves the linear time dependence of ϵ^-. We estimate an upper limit on this term using the time-dependent asymmetries shown in Figure D.3. The time rate of change of ϵ^- is estimated to be $\epsilon^- \sim 10^{-7}$. The factor of Δ suppresses this further by another order of magnitude, lowering it $\sim 10^{-8}$. The second term involves the time rate of change of the flux and can be measured independently using the normalized neutron yields. A fit to these yields gives a value of $\frac{1}{\tilde{N}(t_i)}\frac{\mathrm{d}}{\mathrm{d}t_i}\tilde{N}(t_i) \sim 10^{-6}$, which combined with the order of magnitude suppression from the Δ is well below the limits of the present measurement. A linear fit to the normalized asymmetry $\mathcal{E}_i$ in principle measures the sum of these two terms, but can not be used in the data analysis because the linear term is not orthogonal to the trigonometric functions. For estimation purposes alone however, a linear least squares fit was performed on the asymmetry, yielding a value of $\frac{\mathrm{d}}{\mathrm{d}t_i}\mathcal{E}_i \sim 10^{-7}$. This linear term is actually removed by the rotation sequence of the target which will be discussed further in the next section. The second order term in Δ will thus be the lowest order term to enter directly into the asymmetry.

The quadratic term in Equation E.22 contains three contributing parts:

$$\mathcal{E}_i \sim \frac{16}{3}\Delta^2\frac{\mathrm{d}^2}{\mathrm{d}{t_i}^2}\epsilon^- + \frac{8}{3}\frac{\Delta^2}{\tilde{N}(t_i)}\frac{\mathrm{d}}{\mathrm{d}t_i}\epsilon^-\frac{\mathrm{d}}{\mathrm{d}t_i}\tilde{N}(t_i) + \frac{16}{3}\frac{\Delta^2}{\tilde{N}(t_i)}\frac{\mathrm{d}^2}{\mathrm{d}{t_i}^2}\tilde{N}(t_i). \tag{E.25}$$

The first part contains the quadratic time dependence of the constant offset of the asymmetry. This term is estimated to be at least comparable to the linear term ($\sim 10^{-7}$) and further suppressed by two orders of magnitude by the Δ^2 dependence, setting an upper bound of $\lesssim 10^{-9}$. The second part contains the product of the linear rate of change of both the flux and spin dependent terms. Using the estimates above, this term is $\lesssim 10^{-13}$ and

well below the limits of the present measurement. The third part contains the quadratic dependence of the yield and can be measured using a least squares polynomial fit to the monitor normalized yield. A fit to this yield gives $\frac{1}{\tilde{N}(t_i)}\frac{\mathrm{d}^2}{\mathrm{d}{t_i}^2}\tilde{N}(t_i) \sim 10^{-9}$. A polynomial fit to the asymmetry $\mathcal{E}_i$ (like the linear fit discussed above) is used to estimate this term, yielding a value of $\frac{\mathrm{d}^2}{\mathrm{d}{t_i}^2}\mathcal{E}_i \sim 10^{-11}$. The contributions from the quadratic time dependence of the asymmetry are well below the limits set by the present measurement.

E.2 Target Rotation Sequence

Based on the discussion in the previous section, only the linear time dependent terms in the normalized asymmetry $\mathcal{E}_i$ are large enough to introduce significant components into the trigonometric functions in the fitting procedure discussed in Chapter 5. The target rotation sequence was thus chosen to remove the effect of linear drifts in the sine components of the fit. This procedure is discussed below.

The target is rotated in the angular sequence $-180^\circ \rightarrow +180^\circ \rightarrow -180^\circ$ in 22.5° steps. This pattern of rotation alternates clockwise and counterclockwise rotational directions, and thereby removes the linear terms in time that can contribute to the sine components of the normalized asymmetry. The rotation sequence of the target can be thought of as a four-step sequence analogous to the eight-step sequence discussed above. For an odd trigonometric function about 0° (such as the sines), a rotation from $-180^\circ \rightarrow 0^\circ$ is identical in form to a rotation from $0^\circ \rightarrow -180^\circ$ and similarly a rotation from $0^\circ \rightarrow +180^\circ$ is identical in form to a rotation from $+180^\circ \rightarrow 0^\circ$. Denoting $+$ as a rotation from $-180^\circ \rightarrow 0^\circ$ and $-$ as a rotation from $0^\circ \rightarrow +180^\circ$, the rotation pattern has the form $+\ -\ -\ +$. For an even function such as the cosines, the rotation pattern is $+\ +\ -\ -$. In the sine pattern, the sequence reverses under a change of rotation direction, whereas the cosine pattern does not. This reversal has the effect of removing any linear drifts from the sine components and leaving the cosine components unchanged.

The elimination of the linear components in the sines can expressed mathematically

by investigating the angular fit to the asymmetry using the function

$$y(x) = a_0 + \sum_{k=1}^{7} a_k \sin(k\theta(x)) + \sum_{k=1}^{8} b_k \cos(k\theta(x)). \tag{E.26}$$

For simplicity, the fitting parameters a_k and b_k are calculated using a single value of the asymmetry at each angle for a rotation in one direction ($-180^\circ \rightarrow +157.5^\circ$). The function is fit to the sixteen angular positions using the standard least squares technique [Tho84]. The parameter x represents an integer between 0 and 15 corresponding to the angular position θ in radians and is given by

$$\theta(x) = \pi\left(\frac{x}{8} - 1\right) \qquad x = 0, 1, \ldots, 15. \tag{E.27}$$

Coefficients of

$$\begin{aligned} a_0 &= \frac{1}{16}\sum_{x=0}^{15} y(x) \\ a_k &= \frac{1}{8}\sum_{x=0}^{15} y(x)(-1)^k \sin\left(\frac{k\pi x}{8}\right) \quad k > 0 \\ b_k &= \frac{1}{8}\sum_{x=0}^{15} y(x)(-1)^k \cos\left(\frac{k\pi x}{8}\right) \quad k < 8 \\ b_8 &= \frac{1}{16}\sum_{x=0}^{15} y(x)(-1)^x \end{aligned} \tag{E.28}$$

were determined for the fit. The coefficient a_0 represents the constant offset in the asymmetry discussed in the previous section. The remaining a_k coefficients denote the magnitude of the sine components in the asymmetry and the b_k coefficients denote the magnitude of the cosine components.

A similar fit can be performed using the opposite rotational direction for the angle θ. Provided that $y(x)$ is an odd function of θ (ie. $y(x) \propto x$), the reversal of the angular sequence ($\theta \rightarrow -\theta$) reverses the sign of the a_k ($k > 0$) coefficients while leaving the b_k coefficients and a_0 unchanged:

$$a_0 \rightarrow a_0, \quad a_k \rightarrow -a_k, \quad \text{and} \quad b_k \rightarrow b_k. \tag{E.29}$$

When the two sequences are added together, the a_0 and b_k coefficients add coherently and the a_k coefficients cancel. Terms linear in time are thus removed from the sine coefficients, but remain in the cosines.

In the time reversal measurement, 256 asymmetry measurements were performed at each angle. The fit uses a χ^2 minimization technique to obtain optimum values for the fitting coefficients. This technique is a generalization of the least squares technique used above with the identical cancellation of linear drifts occurring. To verify this generalization, random sets of gaussian distributed data were generated and fit using the same techniques discussed in Chapter 5.

The random sets of data are generated in the same manner as the time reversal data were taken. Each "run" contains 256 randomly generated asymmetries with a constant offset of -5×10^{-4}, comparable to the measured offset in the FC experiment. The same number of runs are generated as in the time-reversal measurement and then fit to Equation E.26 above.

Three random sets of data are generated. The first set consists of gaussian distributed random noise. The remaining two sets consist of random noise combined with a linear time drift. The first of these contains a 0.1% linear drift in which the asymmetry changed linearly from -5×10^{-4} at the start of the rotation sequence to -5.005×10^{-4} at the end of the sixteen run sequence. The second set contains a 1% drift starting at -5×10^{-4} and ending at -5.05×10^{-4}.

The three sets of data were fit to the function given by Equation E.26 and these fits are summarized in Table E.1. The random noise fit shows no non-statistical effects. No effects show up in the sine components. The fit to the 0.1% linear drift data set shows evidence of non-statistical effects in the cosine components of the fit and the 1.0% data set shows definite evidence of this effect. Linear drifts in time must therefore be $\lesssim 10^{-6}$ to keep from appearing in the cosine components of the fit.

The rotation sequence of the target therefore removes any linear time correlated drifts in the sine components of the asymmetry.

Random Noise					
Fitting Coefficient		T-ratio	Fitting Coefficient		T-ratio
Constant	$-498.94 \pm .11 \times 10^{-5}$	474.3	$\cos\theta$	$-.05 \pm .15 \times 10^{-5}$	.3
$\sin\theta$	$.00 \pm .15 \times 10^{-5}$	.0	$\cos 2\theta$	$.07 \pm .15 \times 10^{-5}$	.4
$\sin 2\theta$	$.07 \pm .15 \times 10^{-5}$	.5	$\cos 3\theta$	$.20 \pm .15 \times 10^{-5}$	1.4
$\sin 3\theta$	$-.08 \pm .15 \times 10^{-5}$	.5	$\cos 4\theta$	$.07 \pm .15 \times 10^{-5}$	.5
$\sin 4\theta$	$.12 \pm .15 \times 10^{-5}$	.8	$\cos 5\theta$	$-.19 \pm .15 \times 10^{-5}$	1.3
$\sin 5\theta$	$.14 \pm .15 \times 10^{-5}$	1.0	$\cos 6\theta$	$.07 \pm .15 \times 10^{-5}$	.4
$\sin 6\theta$	$.34 \pm .15 \times 10^{-5}$	2.3	$\cos 7\theta$	$.35 \pm .15 \times 10^{-5}$	2.3
$\sin 7\theta$	$.12 \pm .15 \times 10^{-5}$	.8	$\cos 8\theta$	$.10 \pm .15 \times 10^{-5}$	1.0
Random Noise + 0.1% Linear Drift					
Constant	$-473.68 \pm .11 \times 10^{-5}$	450.3	$\cos\theta$	$.32 \pm .15 \times 10^{-5}$	2.2
$\sin\theta$	$.10 \pm .15 \times 10^{-5}$	.6	$\cos 2\theta$	$-.23 \pm .15 \times 10^{-5}$	1.5
$\sin 2\theta$	$-.24 \pm .15 \times 10^{-5}$	1.6	$\cos 3\theta$	$.01 \pm .15 \times 10^{-5}$	.1
$\sin 3\theta$	$.23 \pm .15 \times 10^{-5}$	1.6	$\cos 4\theta$	$-.48 \pm .15 \times 10^{-5}$	3.3
$\sin 4\theta$	$-.14 \pm .15 \times 10^{-5}$	1.0	$\cos 5\theta$	$.45 \pm .15 \times 10^{-5}$	3.1
$\sin 5\theta$	$-.09 \pm .15 \times 10^{-5}$	.6	$\cos 6\theta$	$-.31 \pm .15 \times 10^{-5}$	2.1
$\sin 6\theta$	$-.19 \pm .15 \times 10^{-5}$	1.3	$\cos 7\theta$	$.18 \pm .15 \times 10^{-5}$	1.2
$\sin 7\theta$	$.03 \pm .15 \times 10^{-5}$	.2	$\cos 8\theta$	$-.22 \pm .11 \times 10^{-5}$	2.1
Random Noise + 1.0% Linear Drift					
Constant	$-251.04 \pm .11 \times 10^{-5}$	238.6	$\cos\theta$	$3.15 \pm .15 \times 10^{-5}$	21.1
$\sin\theta$	$-.02 \pm .15 \times 10^{-5}$	.1	$\cos 2\theta$	$-3.17 \pm .15 \times 10^{-5}$	21.3
$\sin 2\theta$	$.04 \pm .15 \times 10^{-5}$	.3	$\cos 3\theta$	$3.21 \pm .15 \times 10^{-5}$	21.6
$\sin 3\theta$	$-.19 \pm .15 \times 10^{-5}$	1.3	$\cos 4\theta$	$-3.02 \pm .15 \times 10^{-5}$	20.3
$\sin 4\theta$	$.19 \pm .15 \times 10^{-5}$	1.3	$\cos 5\theta$	$2.99 \pm .15 \times 10^{-5}$	20.1
$\sin 5\theta$	$.03 \pm .15 \times 10^{-5}$	.2	$\cos 6\theta$	$-3.30 \pm .15 \times 10^{-5}$	22.2
$\sin 6\theta$	$.28 \pm .15 \times 10^{-5}$	1.9	$\cos 7\theta$	$2.95 \pm .15 \times 10^{-5}$	19.9
$\sin 7\theta$	$.32 \pm .15 \times 10^{-5}$	2.2	$\cos 8\theta$	$-1.36 \pm .11 \times 10^{-5}$	13.0

Table E.1: The effects of a linear time drift in a randomly generated set of data. The T-ratio is the ratio of the extracted value to its standard deviation.

Bibliography

[Ade85] E. G. Adelberger and W. C. Haxton. *Parity Violation in the Nucleon-Nucleon Interaction.* Annual Reviews of Nuclear and Particle Sciences, **35**(1985) 501–558.

[Alf73] V. P. Alfimenkov, V. N. Efimov, Ts. Ts. Panteleev, and Yu. I. Fenin. *Interaction of Polarized Resonant Neutrons with Oriented Nuclei.* Soviet Journal of Nuclear Physics, **17**(1973) 149–152.

[Alf83] V. P. Alfimenkov, S. B. Borzakov, Vo Van Thuan, Yu. D. Mareev, L. B. Pikelner, A. S. Khrykin, and E. I. Sharapov. *Parity Nonconservation in Neutron Resonances.* Nuclear Physics, **A398**(1983) 93–106.

[Alf95] V. P. Alfimenkov, Yu. D. Mareev, V. V. Novitsky, L. B. Pikelner, V. R. Skoy, C. R. Gould, D. G. Haase, and N. R. Roberson. *Measurements of Epithermal Neutron Depolarization Using a Polarized Rare Earth Target.* Nuclear Instruments and Methods, **A352**(1995) 592–595.

[Alt92] I. S. Altarev, Yu. V. Borisov, N. V.Borovikova, S. N. Ivanov, E. A. Kolomensky, M. S. Lasakov, V. M. Lobashev, V. A. Nazarenko, A. N. Pirozhkov, A. P. Serebrov, Yu. V. Sobolev, E. V. Shulgina, and A. I. Yegorov. *New Measurement of the Electric Dipole Moment of the Neutron.* Physics Letters, **B276**(1992) 242–246.

[Ame] Materials Preparation Center at Iowa State University.

[Bar87] A. L. Barabanov. *Possibility of Experimental Study of the Correlation of Partial*

Neutron Amplitudes in Reactions with Oriented Nuclei. Soviet Journal of Nuclear Physics, **45**(1987) 597–601.

[Bea78] B. J. Beaudry and K. A. Gschneidner, Jr. *Preparation and Basic Properties of the Rare Earth Metals.* In K. A. Gschneidner, Jr. and L. Eyring, editors, *Handbook on the Physics and Chemistry of Rare Earths*, pages 173–232. North-Holland Publishing Company, 1978.

[Ber] Winfred M. Berg, Inc., 509 Ocean Ave., East Rockaway, L.I., N.Y. 11518.

[Bev69] P. R. Bevington. *Data Reduction and Error Analysis for the Physical Sciences.* McGraw-Hill Book Company, 1969.

[Bic] Bicron Corporation, 12345 Kinsman Road, Newbury, OH 44065.

[Bla79] J. M. Blatt and V. F. Weisskopf. *Theoretical Nuclear Physics.* Dover Publications, Inc., 1979.

[Bla83] E. Blanke, H. Driller, W. Glöckle, H. Genz, A. Richter, and G. Schrieder. *Improved Experimental Test of Detailed Balance and Time Reversibility in the Reactions* $^{27}Al + p \rightleftharpoons ^{24}Mg + \alpha$. Physical Review Letters, **51**(1983) 355–358.

[Boo86a] D. Boosé, H. L. Harney, and H. A. Weidenmüller. *Tests of Time-Reversal Symmetry in Compound-Nucleus Reactions.* Physical Review Letters, **56**(1986) 2012–2015.

[Boo86b] D. Boosé, H. L. Harney, and H. A. Weidenmüller. *Theory of Time-Reversal Symmetry Breaking in Compound-Nucleus Reactions.* Zeitschrift für Physik, **A325**(1986) 363–369.

[Bow82] J. E. Bowsher. BABEL. Computer code, 1982.

[Bow89] J. D. Bowman, C. D. Bowman, J. Knudson, S. Penttila, S. J. Seestrom, J. J. Symanski, V. W. Yuan, C. R. Gould, D. G. Haase, N. R. Roberson, G. E. Mitchell,

P. P. J. Delheij, H. Postma, and E. D. Davis. *Search for Parity and Time Reversal Symmetry Violation Using Polarized Neutron-Nucleus Interactions.* In H. Henrickson and P. Vogel, editors, *Fundamental Symmetries in Nuclei and Particles*, pages 1–29. World Scientific, 1989.

[Bow93] J. D. Bowman, P. P. Delheij, C. M. Frankle, C. R. Gould, D. G. Haase, J. N. Knudson, G. E. Mitchell, S. Penttilä, H. Postma, N. R. Roberson, S. J. Seestrom, J. J. Szymanski, J. J. Yeh, S. H. Yoo, V. W. Yuan, and X. Zhu. *Experimental Limit on Parity Violation in Nonresonant Neutron-Neutron Scattering.* Physical Review, **C48**(1993) 1116–1119.

[Bri71] D. M. Brink and G. R. Satchler. *Angular Momentum.* Oxford University Press, second edition, 1971.

[Bun93] V. E. Bunakov, H. L. Harney, and A. Richter. *Bayesian Statistics and Experiments on Stochastic Variables.* Nuclear Physics, **A560**(1993) 71–84.

[Cho89] D. Cho, K. Sangster, and E. A. Hinds. *Tenfold Improvement of Limits on T Violation in Thallium Floride.* Physical Review Letters, **63**(1989) 2559–2562.

[Chr64] J. H. Christenson, J. W. Cronin, V. L. Finch, and R. Turlay. *Evidence for the* 2π *Decay of the* K_2^0 *Meson.* Physical Review Letters, **13**(1964) 138–140.

[Cle95a] T. B. Clegg, W. M. Hooke, E. R. Crosson, A. W. Lovette, H. L. Middleton, H. J. Pfutzner, and K. A. Sweeton. *ECR and Cesium Ionizer Systems for the Triangle Universities Nuclear Laboratory Atomic Beam Polarized Ion Source.* Nuclear Instruments and Methods, **A357**(1995) 212–219.

[Cle95b] T. B. Clegg, H. J. Karwowski, S. K. Lemieux, R. W. Sayer, E. R. Crosson, W. M. Hooke, C. R. Howell, H. W. Lewis, A. W. Lovette, H. J. Pfutzner, K. A. Sweeton, and W. S. Wilburn. *A New Atomic Beam Polarized Ion Source for the Triangle Universities Nuclear Laboratory: Overview, Operating Experience, and Performance.* Nuclear Instruments and Methods, **A357**(1995) 200–211.

[Dav88] E. D. Davis. *Compound Nucleus Enhancements of Time-Reversal Non-Invariance.* In J. N. Ginocchoi and S. P. Rosen, editors, *Fundamental Symmetries and Nuclear Structure*, pages 52–67. World Scientific, 1988.

[Des80] B. Desplanques, J. F. Donaoghue, and B. R. Holstein. *Unified Treatment of the Parity Violating Nuclear Force.* Annals of Physics, **124**(1980) 449–495.

[Din95] D. C. Dinge, T. B. Clegg, E. R. Crosson, and H. W. Lewis. *RF Transition Systems for the Triangle Universities Nuclear Laboratory Atomic Beam Polarized Ion Source.* Nuclar Instruments and Methods, **A357**(1995) 195–199.

[Eng94] J. Engel, C. R. Gould, and V. Hnizdo. *Microscopic T-Violating Optical Potential: Implications for Neutron-Transmission Experiments.* Physical Review Letters, **73**(1994) 3508–3511.

[Eng95] J. Engel, P. H. Frampton, and R. P. Springer. *Effective Lagrangians and Parity-Conserving Time-Reversal Violation at Low Energies.* available at Los Alamos nuclear theory preprint archive, 1995.

[Fas73] U. Fasoli, G. Galeazzi, D. Toniolo, and G. Zago. *Fast-Neutron Transmission Through a Polarized Holmium Target.* Letters Nuovo Cimento, **6**(1973) 485–490.

[Fis67] T. R. Fisher, R. S. Safrata, E. G. Shelley, J. McCarthy, S. M. Austin, and R. C. Barrett. *Interaction of Fast Neutrons with Oriented* ^{165}*Ho.* Physical Review, **157**(1967) 1149–1156.

[Fre87] J. B. French, A. Pandey, and J. Smith. *Compound-Nuclear Tests of Time Reversal Invariance in the Nucleon-Nucleon Interaction.* In N. R. Roberson, C. R. Gould, and J. D. Bowman, editors, *Tests of Time Reversal Invariance in Neutron Physics*, pages 80–99, 687 Hartwell Street, Teaneck NJ 07666, USA, 1987. World Scientific Publishing Co., Inc.

[Gou90] C. R. Gould, D. G. Haase, N. R. Roberson, H. Postma, and J. D. Bowman. *Parity and Time Reversal Violation in Resonance Neutron Total Cross Sections with Polarized Targets.* International Journal of Modern Physics, **A5**(1990) 2181–2194.

[Gus83] P. P. Guss, K. Murphy, R. C. Byrd, C. E. Floyd, S. A. Wender, R. L. Walter, T. B. Clegg, and W. Wylie. *The Analyzing Power for the $^2H(d,n)^3He_{g.s.}$ Reaction from 5.5 to 11.5 MeV.* Nuclear Physics, **A395**(1983) 1–14.

[Ham94] Hamamatsu Corporation, 360 Foothill Road, P. O. Box 6910, Bridgewater, NJ 08807-0910. *Photomultiplier Tubes*, 1994.

[Har90] H. L. Harney, A. Hüpper, and A. Richter. *Ericson Fluctuations, Detailed Balance and Time-Reversal Invariance.* Nuclear Physics, **A518**(1990) 35–57.

[Hax94] W. C. Haxton, A. Höring, and M. J. Musolf. *Constraints on* T*-odd and* P*-even Hadronic Interactions from Nucleon, Nuclear, and Atomic Electric Dipole Moments.* Physical Review, **D50**(1994) 3422–3432.

[Hen89] E. M. Henley. *Status of Time Reversal Invariance.* In Pierre Depommier, editor, *Weak and Electromagnetic Interactions in Nuclei*, pages 181–192, B. P. 33, 91192 Gif-sur-Yvette Cedex-France, 1989. Editions Frontières.

[Her92] P. Herczeg. *Theoretical Aspects of Searches for New Interactions Using Oriented Nuclei.* Hyperfine Interactions, **75**(1992) 127–151.

[Hni87] V. Hnizdo and K. W. Kemper. *Spin-Spin Dependence of Total Cross Sections as an Effect of Static Nuclear Deformation.* Physical Review Letters, **59**(1987) 1892–1894.

[Hni94a] V. Hnizdo. *Observables for Polarized Neutrons Transmitted Through Polarized Targets.* Physical Review, **C50**(1994) 2639–2642.

[Hni94b] V. Hnizdo and C. R. Gould. *Optical-Model Description of Time-Reversal Violation in Neutron-Nucleus Scattering.* Physical Review, **C49**(1994) R612–R615.

[Huf95] P. R. Huffman, C. M. Frankle, C. R. Gould, D. G. Haase, J. A. Harvey, N. R. Roberson, and L. W. Weston. *Neutron Resonances in ^{165}Ho, and the Five-Fold Correlation Test of Time Reversal.* submitted to Physical Review C, 1995.

[Hus77] A. H. Hussein, J. M. Cameron, S. T. Lam, G. C. Nelson, and J. Soukup. *Scattering of 10.4 MeV Polarized Neutrons from Bismuth and Lead Between* 2° *and* 65°. Physical Review, **C15**(1977) 233–237.

[Jac93] J. P. Jacobs, W. M. Klipstein, S. K. Lamoreaux, B. R. Heckel, and E. N. Fortson. *Testing Time-Reversal Symmetry Using ^{199}Hg.* Physical Review Letters, **71**(1993) 3782–3785.

[JFB93] Editor J. F. Briesmeister. *MCNP-A General Monte Carlo N-Particle Transport Code.* Radiation Shielding Information Center Computer Code Collection: Oak Ridge National Laboratory, ccc-200/mcnp 4a edition, 1993.

[JMP94] SAS Institute Inc., SAS Campus Drive, Cary, NC 27513. JMP*: Statistical Software for the Macintosh*, 3.1 edition, 1994.

[Kab88] P. K. Kabir. *Transformation of Neutron Polarization in Polarized Media and Tests of T Invariance.* Physical Review, **D37**(1988) 1856–1859.

[Kei94] C. D. Keith. *Total Cross Section Measurements for the Scattering of Polarized Neutrons from Polarized ^{3}He.* Ph.D. thesis, North Carolina State University, 1994.

[Kel69] M. A. Kelley, B. L. Berman, R. L. Bramblett, and S. C. Fultz. *Effect of Nuclear Polarization on the Giant Dipole Resonance in ^{165}Ho.* Physical Review, **179**(1969) 1194–1211.

[Koe66] W. C. Koehler, J. W. Cable, M. K. Wilkinson, and E. O. Wollan. *Magnetic*

Structures of Holmium. I. The Virgin State. Physical Review, **151**(1966) 414–424.

[Kos90] J. E. Koster. *A Test of Time Reversal Invariance with Polarized Neutrons and an Aligned ^{165}Holmium Target.* Ph.D. thesis, North Carolina State University, 1990.

[Kos91] J. E. Koster, E. D. Davis, C. R. Gould, D. G. Haase, N. R. Roberson, L. W. Seagondollar, W. S. Wilburn, and X. Zhu. *Direct Reaction Test of T Violation in 2 MeV Neutron Scattering from Aligned ^{165}Ho.* Physics Letters, **B267**(1991) 23–26.

[Kos92a] J. E. Koster, E. D. Davis, C. R. Gould, D. G. Haase, N. R. Roberson, and L. W. Seagondollar. *Test of Time Reversal Invariance in 2-MeV Neutron Scattering from Aligned ^{165}Ho.* Hyperfine Interactions, **75**(1992) 165–172.

[Kos92b] J. E. Koster, C. R. Gould, D. G. Haase, and N. R. Roberson. *A Rotating Aligned Holmium Target for Neutron Transmission Measurements.* Nuclear Instruments and Methods, **A313**(1992) 464–470.

[Kos94] J. E. Koster, C. R. Gould, D. G. Haase, and N. R. Roberson. *Spatial Orientation of Nuclei: Mass Deformation in 165-Holmium.* Physical Review, **C49**(1994) 710–717.

[Kra86] K. S. Krane. *Nuclear Orientation Formalism.* In N. J. Stone and H. Postma, editors, *Low-Temperature Orientation*, chapter 2, pages 31–112. North Holland Physics Publishing, 1000 AC Amsterdam, The Netherlands, 1986.

[Kra88] K. S. Krane. *Introductory Nuclear Physics.* John Wiley & Sons, Inc., 1988.

[Kru69] M. Krusius, A. C. Anderson, and B. Holmström. *Calorimetric Investigation of Hyperfine Interactions in Metallic Ho and Tb.* Physical Review, **177**(1969) 910–916.

[Kun80] P. D. Kunz. CHUCK. University of Coloraro report, 1980.

[Lau79] K. M. Lau and W. Zimmermann, Jr. *Screw-Fastened Joints for Thermal Contact at Low Temperatures.* Review of Scientific Instrumemts, **50**(1979) 254–255.

[Lis75] P. W. Lisowski, R. L. Walter, C. E. Busch, and T. B. Clegg. *Polarization Transfer in the* $^2H(\vec{d},\vec{n})^3He$ *Reaction at* $\theta = 0°$. Nuclear Physics, **A242**(1975) 298–308.

[Lüd57] G. Lüders. *Proof of the TCP Theorem.* Annals of Physics, **2**(1957) 1–15.

[Mar66] H. Marshak, A. C. B. Richardson, and T. Tamura. *Effect of Nuclear Alignment on the 14-MeV Total Neutron Cross Section of* ^{165}Ho. Physical Review, **150**(1966) 996–1010.

[Mar70] H. Marshak, A. Langsford, T. Tamura, and C. Y. Young. *Total Neutron Cross Section of Oriented* ^{165}Ho *from 2 to 135 MeV.* Physical Review, **C2**(1970) 1862–1881.

[Mas93] Y. Masuda. T-*violating Neutron Spin Rotation Asymmetry.* In C. R. Gould, J. D. Bowman, and Yu. P. Popov, editors, *Time Reversal Invariance and Parity Violation in Neutron Physics*, pages 126–134, Singapore, 1993. World Scientific.

[McC68] J. S. McCarthy, T. R. Fisher, E. G. Shelley, R. S. Safrata, and D. Healey. *Inversion in the Deformation Effect for Neutron Transmission Through Oriented* ^{165}Ho. Physical Review Letters, **20**(1968) 502–504.

[McL88] V. McLane, C. L. Dunford, and P. F. Rose. *Neutron Cross Section Curves*, volume 2. Academic Press, Boston, MA, 1988.

[NET] NE-Technology, Inc. 1 Deerpark Drive, Monmouth Junction, NJ 08852.

[Ohl72] G. G. Ohlsen. *Polarization Transfer and Spin Correlation Experiments in Nuclear Physics.* Reports on the Progress in Physics, **35**(1972) 717–801.

[Phi63] R. J. N. Phillips. *Spin-Dependent Analogues of the Optical Theorem.* Nuclear Physics, **43**(1963) 413–416.

[Pre92] W. H. Press, S. A. Teukolsky, W. T. Vetterling, and B. P. Flannery. *Numerical Recipes in* FORTRAN*: The Art of Scientific Computing.* Cambridge University Press, second edition, 1992.

[Rob81] N. R. Roberson and S. E. Edwards. *Interface for the TUNL VAX Data Acquisiton Facility.* IEEE Transactions on Nuclear Science, **NS-28**(1981) 3834–3837.

[Rob93] N. R. Roberson, C. D. Bowman, J. D. Bowman, P. P. J. Delheij, C. M. Frankle, C. R. Gould, D. G. Haase, J. N. Knudson, G. E. Mitchell, R. N. Mortensen, S. J. Penttilä, H. Postma, S. J. Seestrom, J. J. Szymanski, S. A. Wender, S. H. Yoo, V. W. Yuan, and X. Zhu. *An Apparatus and Techniques of Tests for Fundamental Symmetries in Compund-Nucleus Scattering with Epithermal Polarized Neutron Beams.* Nuclear Inst. and Meth., **A326**(1993) 549–565.

[Rom65] W. A. Roman. *The Metallographic Preparation of Some Rare-Earth Metals.* Journal of Less-Common Metals, **10**(1965) 150–152.

[Sac87] R. G. Sachs. *The Physics of Time Reversal.* The University of Chichago Press, 1987.

[Sat71] G. R. Satchler, J. Arvieux, S. D. Baker, T. B. Clegg, S. E. Darden, L. J. B. Goldfarb, J. A. R. Griffith, W. Grüebler, W. Haeberli, G. M. Hale, P. W. Keaton, Jr., E. J. Ludwig, J. S. C. McKee, G. G. Ohlsen, F. G. Perey, G. R Plattner, P. A. Quin, J. Raynal, N. Rohrig, S. Roman, G. Roy, P. Schwandt, F. Seiler, R. G. Seyler, P. Shanley, H. Sherif, J. E. Simmons, M. Simonius, and L. D. Tolsma. *The Madison Convention.* In H. H. Barschall and W. Haeberli, editors, *Proceedings of the 3rd International Symposium on Polarization Phenomena in Nuclear Reactions*, pages xxv–xxix, Madison, 1971. The University of Wisconsin Press.

[Sat83] G. R. Satchler. *Direct Nuclear Reactions.* Oxford University Press, 1983.

[Shi93] H. M. Shimizu, T. Maekawa, Y. Takahashi, and T. Yabuzaki. *Polarized Target for* T-*Violation Experiment.* In C. R. Gould, J. D. Bowman, and Yu. P. Popov, editors, *Time Reversal Invariance and Parity Violation in Neutron Physics*, pages 135–137, Singapore, 1993. World Scientific.

[Sim74] M. Simonius. *Theory of Polarization Measurements. Observables, Amplitudes, and Symmetries.* In D. Fick, editor, *Lecture Notes in Physics*, volume 30, pages 38–87. Springer-Verlag, Berlin, 1974.

[Sim75] M. Simonius. *On Time Reversal Violation in the Nucleon–Nucleon System.* Physics Letters, **58B**(1975) 147–151.

[Smi90] K. F. Smith, N. Crampin, J. M. Pendlebury, D. J. Richardson, D. Shiers, K. Green, A. I. Kilvington, J. Moir, H. B. Prosper, D. Thompson, N. F. Ramsey, B. R. Heckel, S. K. Lamoreaux, P. Ageron, and W. Mampe. *A Search for the Electric Dipole Moment of the Neutron.* Physics Letters, **B234**(1990) 191–196.

[Sod88] J. P. Soderstrum, C. R. Gould, D. G. Haase, L. W. Seagondollar, M. B. Schneider, and N. R. Roberson. *Limits on P- and P,T-Violating Absorption of MeV Neutrons in* ^{165}*Ho.* Physical Review, **C38**(1988) 2424–2426.

[SPE93] SPEAKEASY Computing Corporation, 224 South Michigan Avenue, Chicago, IL 60604. SPEAKEASY *IV*, 1993.

[Sto86] L. Stodolsky. *Novel Time-Reversal Tests in Low-Energy Neutron Propagation.* Physics Letters, **B172**(1986) 5–9.

[Tho84] W. J. Thompson. *Computing in Applied Science.* John Wiley and Sons, 1984.

[VdG60] R. J. Van de Graaff. *Tandem Electrostatic Accelerators.* Nuclear Instruments and Methods, **8**(1960) 195–202.

[Wag65] R. Wagner, P. D. Miller, T. Tamura, and H. Marshak. *Interaction of 350-keV*

Polarized Neutrons with Oriented ^{165}*Ho Nuclei*. Physical Review, **139**(1965) B29–B46.

[Wil93] W. S. Wilburn. *Measurements of the Transverse Spin-Dependent Total Cross Section Difference* $\Delta\sigma_T$ *for the Scattering of Polarized Neutrons from Polarized Protons*. Ph.D. thesis, Duke University, 1993.

[Wil95] W. S. Wilburn, 1995. Designed and constructed at TUNL.

[You83] P. G. Young, E. D. Arthur, C. Philis, P. Nagel, and M. Collin. *Analysis of* $n+^{165}$*Ho and* ^{169}*Tm Reactions*. In K. H. Böckhoff, editor, *Nuclear Data for Science and Technology*, page 792. D. Reidel Publishing Company, 1983. Proceedings of the International Conference, Antwerp, September 1982.

Biography

Paul Reece Huffman

Personal

- Born in Winston-Salem, North Carolina, June 6, 1968
- Married Roxanne Gurganus, August 4, 1991

Education

- B.S. Physics, North Carolina State University, Raleigh, North Carolina, 1990
- A.M. Physics, Duke University, Durham, North Carolina, 1992

Memberships

- American Physical Society
- Sigma Pi Sigma

Publications

1. W. S. Wilburn, C. R. Gould, D. G. Haase, P. R. Huffman, C. D. Keith, J. E. Koster, N. R. Roberson, and W. Tornow. *Measurements of Polarized Neutron – Polarized Proton Scattering: Implications for the Triton Binding Energy.* Physical Review Letters, **71** 1982 (1993).

2. P. R. Huffman, C. M. Frankle, C. R. Gould, D. G. Haase, and N. R. Roberson. *Deformation Effect and Five-Fold Correlation Time Reversal Test in Neutron Resonances Using Aligned ^{165}Ho.* In C. R. Gould, J. D. Bowman, and Yu. P. Popov, editors, *Time Reversal Invariance and Parity Violation in Neutron Reactions,* pages 151–159 (World Scientific Publishing Co., Inc., 1994).

3. J. E. Koster, E. D. Davis, C. R. Gould, D. G. Haase, P. R. Huffman, and N. R. Roberson. *The TUNL Five-Fold Correlation Experiment.* In C. R. Gould, J. D. Bowman, and Yu. P. Popov, editors, *Time Reversal Invariance and Parity Violation in Neutron Reactions,* pages 144–150 (World Scientific Publishing Co., Inc., 1994).

4. C. D. Keith, C. R. Gould, D. G. Haase, P. R. Huffman, N. R. Roberson, M. L. Seely, W. Tornow, and W. S. Wilburn. *Measurement of the Polarized Neutron – Polarized ^{3}He Total Cross Section. AIP Conference Proceedings 334,* pages 449–432 (American Institute of Physics Press, New York, 1995).

5. C. R. Gould, D. G. Haase, P. R. Huffman, C. D. Keith, N. R. Roberson, M. L. Seely, and W. S. Wilburn, *Testing P-even Time Reversal Invariance with MeV Neutrons.* In S. J. Seestrom, editor, *AIP Conference Proceedings 338,* pages 270–275 (American Institute of Physics Press, New York, 1995).

6. D. G. Haase, C. D. Keith, C. R. Gould, P. R. Huffman, N. R. Roberson, M. L. Seely, and W. S. Wilburn, *A Statically Polarized Solid ^{3}He Target. AIP Conference Proceedings 343,* pages 527–531 (American Institute of Physics Press, New York, 1995).

7. P. R. Huffman, C. R. Gould, D. G. Haase, C. D. Keith, N. R. Roberson, M. L. Seely, and W. S. Wilburn, *An Experimental Test of Parity-Even Time Reversal Invariance with MeV Neutrons. AIP Conference Proceedings 339,* pages 185–190 (American Institute of Physics Press, New York, 1995).

8. M. L. Seely, C. R. Gould, D. G. Haase, P. R. Huffman, C. D. Keith, N. R. Roberson, W. Tornow, and W. S. Wilburn. *Polarized Targets at Triangle Universities Nuclear*

Laboratory. Nuclear Instruments and Methods A, **356** 142 (1995).

9. C. D. Keith, C. R. Gould, D. G. Haase, P. R. Huffman, N. R. Roberson, M. L. Seely, W. Tornow, and W. S. Wilburn. *A Polarized Solid ^{3}He Target for Neutron Transmission Experiments.* Nuclear Instruments and Methods A, **357** 142 (1995).

10. W. S. Wilburn, C. R. Gould, D. G. Haase, P. R. Huffman, C. D. Keith, N. R. Roberson, and W. Tornow. *Measurements of $\Delta\sigma_T$ in Polarized-Neutron – Polarized-Proton Scattering.* To appear in Physical Review C (November 1995).

11. P. R. Huffman, C. M. Frankle, C. R. Gould, D. G. Haase, J. A. Harvey, and N. R. Roberson *Neutron Resonances in ^{165}Ho, and the Fivefold Correlation Test of Time Reversal.* Submitted to Physical Review C for publication.

12. W. S. Wilburn, C. R. Gould, D. G. Haase, P. R. Huffman, C. D. Keith, N. R. Roberson, and W. Tornow. *Measurements at Low Energies of the Polarization Transfer Coefficient $K_y^{y'}$ for the Reaction $^3H(\vec{p},\vec{n})^3He$ at 0°.* In progress.

Abstracts

1. W. S. Wilburn, P. R. Huffman, J. E. Koster, N. R. Roberson, W. Tornow, C. R. Gould, D. G. Haase, and C. D. Keith. *Measurement of $\Delta\sigma_T$ in Polarized Neutron/Polarized Proton Scattering.* Bulletin of the American Physical Society, **37** 902 (1992).

2. C. D. Keith, C. R. Gould, D. G. Haase, P. R. Huffman, N. R. Roberson, W. Tornow, and W. S. Wilburn. *Level Structure of ^{4}He and the Spin Dependence of the n-^{3}He Total Cross Section.* Bulletin of the American Physical Society, **37** 1257 (1992).

3. W. S. Wilburn, P. R. Huffman, J. E. Koster, N. R. Roberson, W. Tornow, C. R. Gould, D. G. Haase, and C. D. Keith. *The NN Tensor Force from $\vec{n}$-$\vec{p}$ Scattering.* In I. R. Afnan and R. T. Cahill, editors, *Proceedings of the XIII International Conference on Few-Body Problems in Physics,* Adelaide, 1992, page 124.

4. W. S. Wilburn, P. R. Huffman, N. R. Roberson, W. Tornow, C. R. Gould, D. G. Haase, C. D. Keith, T. P. Murphy, and B. W. Raichle. *Measurement of $\Delta\sigma_T$ in Polarized Neutron/Polarized Proton Scattering.* Bulletin of the American Physical Society, **38** 1063 (1993).

5. W. S. Wilburn, P. R. Huffman, J. E. Koster, N. R. Roberson, W. Tornow, C. R. Gould, D. G. Haase, and C. D. Keith. *Measurements of Polarized Neutron – Polarized Proton Scattering: Implications for the Triton Binding Energy.* Bulletin of the American Physical Society, **38** 1846 (1993).

6. C. D. Keith, C. R. Gould, D. G. Haase, P. R. Huffman, N. R. Roberson, W. Tornow, and W. S. Wilburn. *A Polarized Solid ^{3}He Target for Polarized Neutron Scattering.* Bulletin of the American Physical Society, **39** 1042 (1994).

7. P. R. Huffman, N. R. Roberson, C. R. Gould, D. G. Haase, C. M. Frankle, and J. A. Harvey. *Neutron Resonances in ^{165}Ho and the Five-Fold Correlation Test of Time Reversal.* Submitted to the American Physical Society Division of Nuclear Physics Meeting, October 25–28, 1995.

8. P. R. Huffman, N. R. Roberson, W. S. Wilburn, C. R. Gould, D. G. Haase, C. D. Keith, B. W. Raichle, and M. L. Seely. *Polarized Neutron Source and Detectors for the TUNL Parity-Even Test of Time Reversal Invariance.* Submitted to the American Physical Society Division of Nuclear Physics Meeting, October 25–28, 1995.

Oral Presentations

1. *A Test of Time Reversal Invariance Using Neutron Transmission.* Given at the 6^{th} Annual Summer School for Nuclear Physics Research, Raleigh, NC (July, 1993).

2. *A Test of Parity-Even Time Reversal Invariance with MeV Neutrons.* Given at the 8^{th} International Symposium on Polarization Phenomena in Nuclear Physics, Bloomington, IN (September, 1994).

3. *A Parity-Even Test of Time Reversal Invariance.* Invited talk given at the National Institute of Standards and Technology, Gaithersburg, MD (September, 1995).